ABSTRACT

FACCHINE, EMILY GRACE. Dynamic Microstructures and Interactions of Biobased Nanomaterial Suspensions. (Under the direction of Dr. Saad Khan and Dr. Orlando Rojas).

Biobased nanomaterials such as nanocellulose and nanochitin have major potential to contribute to a more sustainable society. In order to realize this potential, a fundamental understanding of these materials, their properties, and their interactions with each other and their environment is a critical step. In pursuit of this goal, we have examined several such systems in this work, in which we will present our observations and conclusions regarding various structures and interactions in these systems and their implications for improved sustainability. For context, **Chapter 1** provides a brief overview of biobased nanomaterial properties and classifications while highlighting some noteworthy previous studies that have laid the foundation for the work presented here.

In **Chapter 2** we study the rheological response of gel-like micro/nanofibrillated cellulose (MNFC) suspensions, which are characteristically heterogeneous and prone to flocculation. To understand these behaviors, we probe the response of the characteristic heterogeneous features to different shear conditions, highlighting regimes in which the features persist and others in which they are disrupted to facilitate homogeneity. These regimes are bound by apparent yield stress transitions, in which the system exhibits an uncommon two-step yield mechanism related to the sequential breakdown of first, the percolated gel network, and second, the large-scale aggregated floc features. The results observed for this system are characteristic of the hierarchical structure present in MNFC gels and provide insight to the interactions between flocs and fibrils. The details also have the potential to help guide selection of processing conditions and product applications in the commercialization of MNFC and related materials.

In **Chapter 3**, we shift our focus to cellulose nanocrystals and their propensity to form chiral nematic phases in aqueous suspension. This behavior has been extensively documented and it is generally thought that the minimum concentration at which these phases are observed (termed c^*) is dependent on both crystal characteristics and suspension conditions, and as such can be used as an aggregate indicator of surface charges, colloidal stability, and other properties. Current methods of determining this value have considerable room for improvement with respect to time requirement, sample requirement, precision and accuracy. **Chapter 3** describes a method we have developed to efficiently measure c^* by quantifying the heat of interactions in the suspension during a dilution experiment. We show how microcalorimetry can provide thermodynamic detail at a very fine level, which allows us to detect viscous heating effects associated with the transition from a suspension in the biphasic regime (above c^*) to one that is fully isotropic (below c^*). This method is tested for a variety of CNCs with different properties, and good agreement is shown with the expected values for critical concentration, indicating the universality of the approach.

Chapter 4 concerns synergistic hybrid systems accessible by combining two or more varieties of biobased nanomaterials. As an example of such a system, we examine the range of possible interactions when combining cationic nanochitin (NCh) with anionic cellulose nanofibers (CNF). The system is characterized rheologically and calorimetrically, in order to link the microstructural observations with measured particle interactions. We demonstrate the potential for synergistic ionic complex formation, along with the competing effects of ionization and deionization of the different species under various pH conditions. By manipulating these interactions and controlling the ratio of NCh to CNF, we can access a wide range of rheological profiles, allowing adjustment of elastic modulus (G’) across a full order of magnitude without changing the solids content of the system. In conjunction with this promising opportunity for tunability, we present several relevant considerations regarding the order of operations when adjusting pH of the system and complexing materials of opposite charge, which are useful in attempts to optimize the system behavior for target applications.

Dynamic Microstructures and Interactions of Biobased Nanomaterial Suspensions

by
Emily Grace Facchine

A dissertation submitted to the Graduate Faculty of
North Carolina State University
in partial fulfillment of the
requirements for the degree of
Doctor of Philosophy

Chemical Engineering

Raleigh, North Carolina

2020

APPROVED BY:

Dr. Saad Khan
Committee Co-chair

Dr. Orlando Rojas
Committee Co-chair

Dr. Richard Spontak

Dr. Lillian Hsiao

Dr. Lokendra Pal
External Member

BIOGRAPHY

Emily Grace Facchine was born in Raleigh, North Carolina in 1993 to Kevin and Lindsay Facchine. Growing up in the Raleigh area with her two sisters, Hannah and Libby, she attended Wake County public schools Oak Grove Elementary, Carnage Magnet Middle School and William G. Enloe Magnet High School. She played the violin in school orchestras throughout middle and high school and participated in competitive swimming on various local teams, which led her to sign with the University of Alabama as a student-athlete in 2011, where she studied chemical engineering in addition to competing on the swim team for four years, serving as team captain in her junior and senior years. Upon completion of her B.S. in chemical engineering (*summa cum laude*) she returned to Raleigh and entered the PhD program in Chemical and Biomolecular Engineering at NC State. Here she found an excellent fit in the research group of Dr. Saad Khan, working on a project funded by Eastman Chemical Company and co-advised (remotely) by Dr. Orlando Rojas, based at Aalto University in Espoo, Finland. This project and the goodwill of her advisors provided her the opportunity to spend 4 months doing research in the Biobased Colloids and Materials group at Aalto University (led by Dr. Rojas), during which she was fortunate to be able to experience Finnish summer and visit 9 other countries in addition to her time spent in Finland. During her graduate studies, she also served as a member of the Graduate Student Association of NC State, External Vice President for the Chemical & Biomolecular Engineering Graduate Student Association, a graduate student coordinator of Future Leaders in Chemical Engineering, and a Recruiting Captain. She considers the five years spent in the Chemical and Biomolecular Engineering Department at NC State to be some of the best of her life so far.

ACKNOWLEDGMENTS

Countless people have uplifted and supported me throughout the past five years, and I can hardly express my gratitude sufficiently on paper, but here is an abridged list of the people who have contributed to my success:

To Dr. Khan and Dr. Rojas, thank you for taking an equally sincere interest in my well-being as you have in my work. The encouragement and positivity I have received from both of you throughout this journey has been nothing short of inspirational. In addition to guiding my research, you have mentored me through the subtleties of networking and working with industry, and you have always advocated for me. I am deeply grateful for you both. Thank you also to Dr. Richard Spontak for his always valuable and interesting insight to the Eastman work, and for sharing his wisdom and expertise regarding intellectual property and his incredibly helpful feedback on my publications.

To the BiCMat group at Aalto and beyond, for creating a richly diverse and incredibly welcoming environment, which made it so easy to feel at home while travelling internationally. Especially Gabi Berto, Carlos Silveira, and Antonio María; for all our adventures.

To The Khan group at NC State, for being a positive, supportive community, especially: Ria Corder and Barbara Farias, for being fantastic role models and making me feel welcome to the group, sharing dog stories in the office and teaching me how to operate in grad school; and Soo-Ah, for being a reliable and valuable teammate in the Eastman work and helping me feel at home in Finland, where we enjoyed many legendary brunches.

To Kate Kornau in the Eastman Center of Excellence for her guidance and teamwork in the Eastman project that funded my research and for being so pleasant to work with.

To countless friends and colleagues in the Chemical and Biomolecular Engineering Department and beyond, especially: Emily Krzystowczyk (Sunshine) for being there for me all the time and for understanding and appreciating the genius of Taylor Swift; Minyung Song for agreeing to go to any concert any time and for much-needed walks and joint online shopping sprees; Amber Hubbard for being my gateway friend and thesis-writing role model; Rachel Nye, for always making me smile and inspiring me with your relentless enthusiasm and work ethic; Sahand Saberi, for being my happy hour co-captain and job interview coach; Ryan Dudek for infinite coffee breaks and movie quotes; Jason Miles for pimento cheese and being the most reliable person I know; Ryan Barton for teaching me to play volleyball and attempting some frankly dangerous swing dancing stunts; Taylor Neumann for always being game for Chick-Fil-A and karaoke in the car; Chris Estridge for being sour and sweet and always coming through with Pedialyte; Chilton Birdwhistell for your unshakable positivity and inspiring ambition, Victoria Mitchell for being my ideal workout partner and always keeping it real, Cameron Brown for being such a caring and generous friend, Seif Yusuf for all the smiles, laughs, and sarcasm; Dilara Sen, for your bright disposition and for allowing me to be a part of an unforgettable wedding celebration in a beautiful country; Jenna Meanor, for helping me survive Recruiting 2018.

To my family: my older sister, Hannah, for acting as my role model, therapist and life coach and for 4:00 PM daily phone calls (and 7:00 AM ones when I was in Finland); my younger sister, Libby, for your brutal honesty, staunch loyalty, excellent cooking, and driving me to the grocery store in my first year of graduate school; Mom, for everything. I have learned so much from you about how to treat other people and it has served me well throughout graduate school and life. Dad, for everything. Your support, advice, and example helped lead me to pursue this degree which has been one of the best decisions of my life. I am more grateful for my family than I could ever put into words.

TABLE OF CONTENTS

LIST OF TABLES

LIST OF FIGURES

CHAPTER 1

Introduction

1.1 Motivation

Single-use plastics and petroleum-derived polymeric materials are ubiquitous in our daily lives, and all of these contribute to the global problem of solid waste accumulation and overflowing landfills. It is estimated that by the year 2050 the ocean may contain more plastic than fish,[1] due to the habitual use of unsustainable materials. Biobased nanomaterials have legitimate potential as replacements in numerous applications[2] which conventionally employ petroleum-derived polymers, making them a critical step towards a more sustainable society. By virtue of their natural origin, biobased nanomaterials have a reduced impact on the environment[3] and have even been studied as remedial agents for environmental cleanup efforts.[4] In order to optimize and effectively implement these materials, a thorough understanding of their properties and behaviors is an important first step.

1.2 Background

A general overview of the key concepts including materials, methods, and some noteworthy previous works in the field is provided here; however, each chapter contains the relevant background necessary to be read on its own.

1.2.1 Biobased Nanomaterials

Biobased nanomaterials can be defined as a class of materials which are derived from biological sources (plants, animals, fungi, etc.) and have at least one dimension in the nanoscale. They can be prepared by bottom-up or, more commonly, top-down methods and possess a variety of morphologies and surface chemistries. Perhaps the most widely used are nanocellulosic materials, which can be grouped into different classes based upon their preparation method, morphology, and surface properties. Additionally, a rapidly growing topic in the study of biobased nanomaterials is nanochitin, which shares many properties and advantages of nanocellulose, but possesses several distinctions which expand the potential applications. In this work, we will discuss insights about the dynamic microstructures and particle interactions of several biobased nanomaterials as they apply in aqueous suspensions. These findings are intended to aid characterization and understanding of biobased nanomaterials and to facilitate their implementation in new and existing applications.

Nanocellulose is derived from a variety of natural sources (e.g., wood, cotton, bacterial sources) and can be divided into 3 categories with distinct properties: micro/nanofibrillated cellulose (MFNC, **Figure 1.1a**), cellulose nanofibrils (CNF, **Figure 1.1b**), and cellulose nanocrystals (CNCs, **Figure 1.1c**). Several reviews are available on specifics of production of nanocelluloses[5] and their various properties,[6–8] and an extensive review discusses standard characterization techniques thereof.[9]

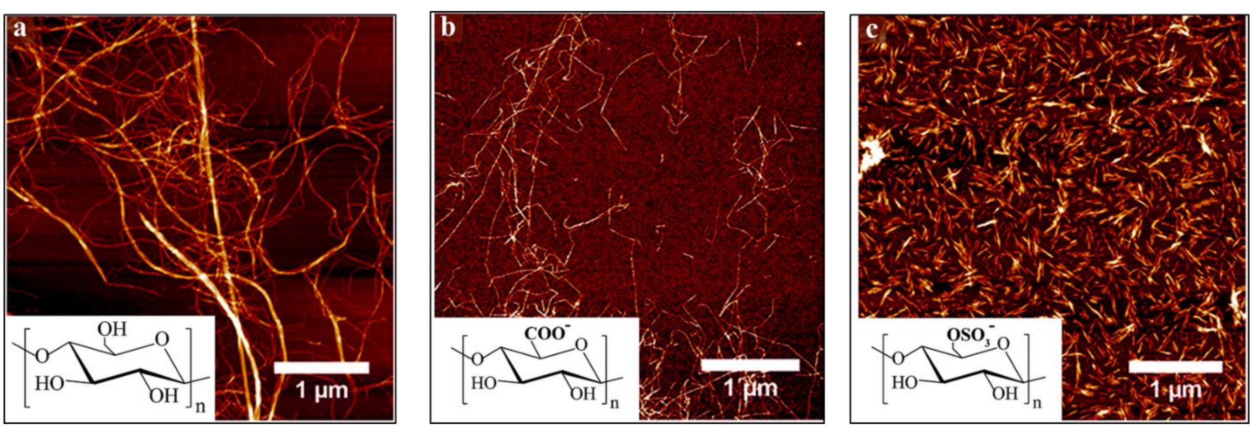

Figure 1.1. AFM images showing the different morphologies of nanocellulose. (a) MNFC, (b) CNF (c) CNC. (Adapted from Benítez and Walther, 2017)[10]

Briefly, cellulose nanocrystals (CNCs) possess characteristically shorter aspect ratios than the two fibrillar varieties of nanocellulose, in addition to higher crystallinity and stiffness. CNCs are typically produced by acid hydrolysis of the source material, which dissolves less-ordered regions in the cellulosic fiber structure, leaving intact particles of highly ordered cellulose polymer chains bound to one another by extensive hydrogen bonding. Many preparation protocols also impart charged moieties to the particle surface, such as sulfate half-esters in the case of sulfuric acid hydrolysis preparation routes. Higher aspect ratio forms of nanocellulose are designated as MNFC or CNF. MNFC particles are characteristically somewhat heterogenous and polydisperse, produced by purely mechanical means without chemical modification or enzymatic pretreatment of the cellulose source. This means that the degree of defibrillation is often highly varied, and aggregation can be a major factor since no stabilizing surface charges are deliberately applied (although in some cases there is still an appreciable charge as a result of native functional groups, such as carboxylates from hemicelluloses).[11] CNF particles are typically more uniform than MNFC and have superior colloidal stability due to the inclusion of an enzymatic or chemical modification step in their preparation, for the purpose of imparting charged groups on the surface. For example, (2,2,6,6-Tetramethylpiperidin-1-yl)oxyl or TEMPO-mediated oxidation is often used to convert CNF surface hydroxyl groups to carboxylates. While this improved colloidal stability and uniformity is preferred for certain applications, the less homogenous MNFC cellulose has its own advantages, such as reduced environmental impact due to chemical-free preparation. Additionally, the broad range of size scales at play in these systems provide some hierarchical structural features (**Figure 1.2**) that can provide value in various applications. Among these three main morphology classifications (CNC, CNF, and MNFC), surface chemistry and particle properties can be tuned in a number of ways, creating a vast library of particles and suspensions from which to choose for targeted applications.

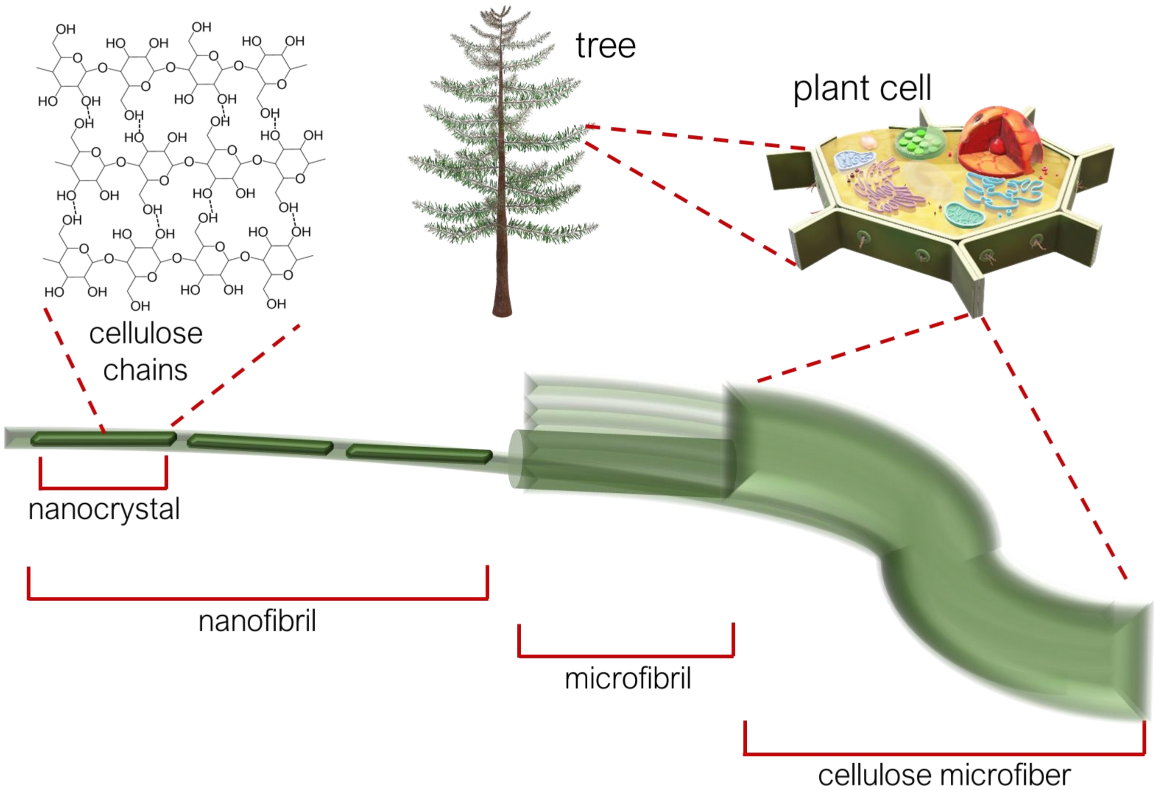

Figure 1.2. Nanocellulose hierarchy. Plant matter, such as wood, is comprised of plant cells, and the plant cell walls contain cellulose-based microfibers which themselves are bundles of the smaller fibril units that make up micro/nanofibrillated cellulose. Nanofibrils contain regions of high crystallinity, which can be isolated to obtain nanocrystals.

Nanochitin is similar to nanocellulose in many ways but is sourced from animal matter such as shrimp and crab shells rather than from plant or bacterial sources as with nanocellulose. The chitin polysaccharide structure differs from cellulose in the presence of an acetyl amine group in place of one of the hydroxyls on each glucose unit (**Figure 1.3**). This functional group imparts a higher degree of hydrophobicity than what is typical for nanocellulose. This functional group is also a target for deacetylation treatments, which are commonly used to convert the acetyl amine to an amine group, giving the nanochitin particles a positive surface charge in acidic conditions.[12] Similar to nanocellulose, nanochitin can be manipulated to take the form of a short rigid chitin nanocrystal (ChNC) by acid treatment[13] or longer, more flexible chitin nanofibril (ChNF)[14] by mechanical methods and/or partial deacetylation, but these distinctions and their characterization are less mature than in the case of nanocellulose, and at times the more general designation nanochitin (NCh) is preferred.

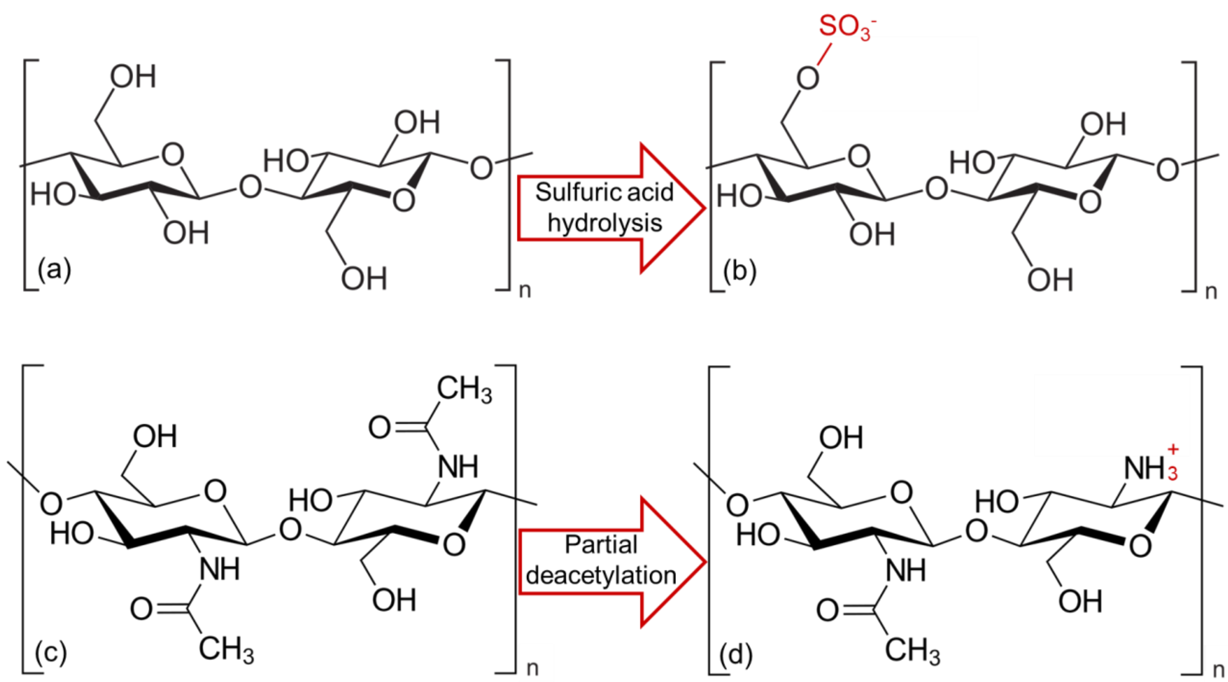

Figure 1.3. Molecular structures of cellulose and chitin polymers subjected to common modification treatments. (a) repeat unit of cellulose (b) substitution of a sulfate half-ester on cellulose surface by acid hydrolysis (c) repeat unit of chitin (b) removal of acetyl group on chitin surface by partial deacetylation

1.2.2 Methods

Two primary methods are employed in this work: rheology and calorimetry. Both are concerned with elucidating information about microstructural features and interparticle interactions of biobased nanomaterials in aqueous suspension. Chapter 2 is supported primarily by rheological measurements and Chapter 3 primarily by calorimetry. Chapter 4 is dependent on both methods and the complementary data that they provide.

1.2.2.1 Rheology

Rheology is used to directly measure the microstructure *via* material functions, *e.g.* viscosity, elasticity, and yield stress, by quantifying stress responses under the application of shear. These measurements are critical for a fundamental understanding of the suspension behavior as well as for employment of the materials in target applications (coatings, 3D printing). In addition to direct microstructural information, it is possible to indirectly characterize some particle interactions. For example, time-dependent or shear-dependent structure responses can be interpreted to gain insight about attractive forces between the particles which form the network structure.

Rheological tests can be split into two groups: steady shear experiments and dynamic oscillatory experiments. Steady shear provides details about how the material responds to different applied shear rates (**Figure 1.4**). This response can be Newtonian, as in the case of water or honey, meaning that the viscosity value is independent of the applied rate of shear. More complex fluids such as colloidal suspensions or polymer solutions are often shear-thinning, meaning that the apparent viscosity is reduced when higher shear rates are applied. This response is typically due to alignment of particles or breakage of weak attractions between them (an example of indirect particle interaction detectable by rheological measurement). Yield stress behavior can also be detected in steady shear experiments, by the absence of a Newtonian plateau and a slope of ~ -1 at low shear rates. In contrast to steady shear, which depends upon the sample being subjected to large-scale deformations, oscillatory shear experiments can elucidate the characteristics of the material "at rest" by applying small oscillatory deformations and allowing characterization of the material without destruction of the network.

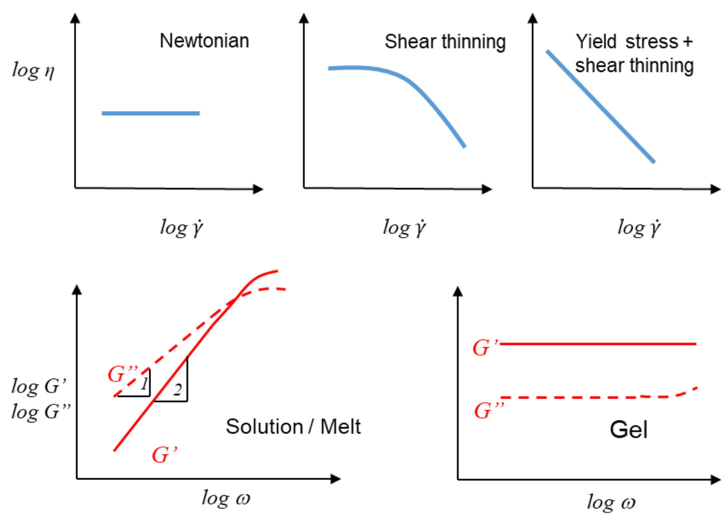

Figure 1.4 Examples of rheology plots. Top: Dependence of viscosity on shear rate can exhibit several different relationships, including Newtonian, shear-thinning, and/or yield stress. Bottom: Similarly, oscillatory frequency sweeps can take different profiles, which include frequency dependence of viscoelastic moduli in the case of liquid-like samples (left), or frequency independence for solid-like samples (right).

1.2.2.2 Calorimetry

Isothermal titration calorimetry is an analytical method by which heats of interaction between two liquids can be quantified. This technique is frequently used to measure, for example, binding constants between proteins and ligands[15] and surfactant parameters such as critical aggregation concentration.[16] The titrant is injected into a sample cell which contains the titrand while temperature is continuously monitored in the sample cell along with a reference cell (**Figure 1.5**, left). Heat evolved or absorbed by the interactions between titrant and titrand cause small changes in

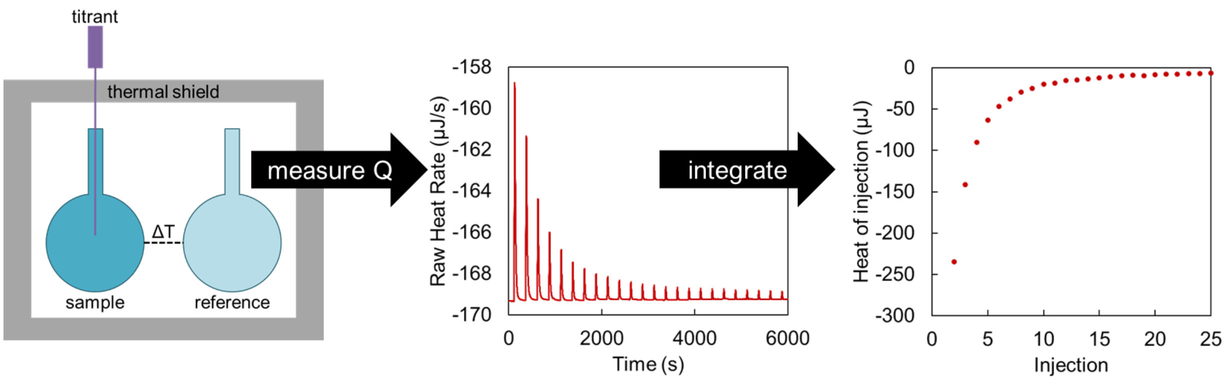

Figure 1.5. Isothermal titration calorimeter (left) continuously collects and records the heater power required to maintain isothermal conditions. This data (center) can be integrated to provide the heat value associated with interactions of each separate injection (right).

the temperature of the sample cell, which are compensated for by a feedback heater based on continuous monitoring of ΔT between the sample and reference cells. The heat rate supplied is proportionate to the heat evolved or absorbed in the cell (**Figure 1.5**, center panel) and can be integrated with respect to time, allowing assignment of a heat value to each injection or concentration ratio of titrant to titrand (**Figure 1.5**, right). Hence the thermodynamics of the interaction can be analyzed, by direct measurement of enthalpy and calculation of entropy via Gibbs free energy.

1.2.3 Previous efforts in the field

Nanoparticles of cellulose and chitin are readily dispersible in water, and the resultant hydrogels and aqueous suspensions possess properties that can be employed for rheology-modifying applications or mechanical reinforcement, but with less environmental impact than many conventional additives. The surface charges make them colloidally stable, their high aspect ratio makes them shear-thinning, and yield stress behavior is observed at relatively low concentrations (0.5 wt% in the case of MNFC)[17]. Additionally, CNCs and chitin nanocrystals (ChNCs) both exhibit chiral nematic phase formation in aqueous suspension (**Figure 1.6**), which permits their use in optical, sensing, and templating applications[18].

These and other properties have led to avid study of biobased nanomaterial suspension systems over the past decades. Here we will highlight a few select works relevant to the present studies. More specifics about relevant previous works are provided in the introduction sections for each chapter. We have already mentioned the existence of several reviews covering production,[19] properties,[20] and characterization[9] of nanocellulose. The properties of most interest to this dissertation are the rheology, chiral nematic phase formation, and ionic complexation effects of these materials. Regarding these topics, several more targeted reviews are available, which cover rheology of pulp fiber supsensions,[21] nanocellulose suspensions in general,[22] and specifically nanofibrils.[23] A number of original studies were of particular value in laying the foundation for the present works. Iotti et al.[24] and Hill[25] were among the first to conduct rheological studies of MNFC suspensions. Later work by Nechyporchuk et al.[26] and Nazari et al.[27] was instrumental in exploring wall slip and yield stress behaviors of these suspensions, and Saarikoski et al[28] were among the first to visualize and quantify flocculated structures which are so influential in the shear behavior. Much of this work was informed by previous research pertaining to pulp suspensions,[29,30] which share many characteristics with nanocellulose in general but especially with MNFC. Several more generalized studies compare the rheology of the different classifications of nanocellulose.[31] Naturally, the differing aspect ratios and morphologies between crystals and fibrils create distinct rheological behavior; hence CNC rheology has also been the specific focus of numerous investigations.[32–37] For example, there is some indication[32,33] that the formation of ordered mesophases has a marked impact on the flow behavior, as these aligned regions can flow intact at low shear rates and be broken down to individual crystals at higher shear. This is just one example of how the liquid crystalline properties of CNCs are an important topic of study, and this area has also been avidly explored, beginning with their adherence to Onsager theory[38] and following with ionic strength effects[39,40], aspect ratio effects[41,42] surface charge effects[43].

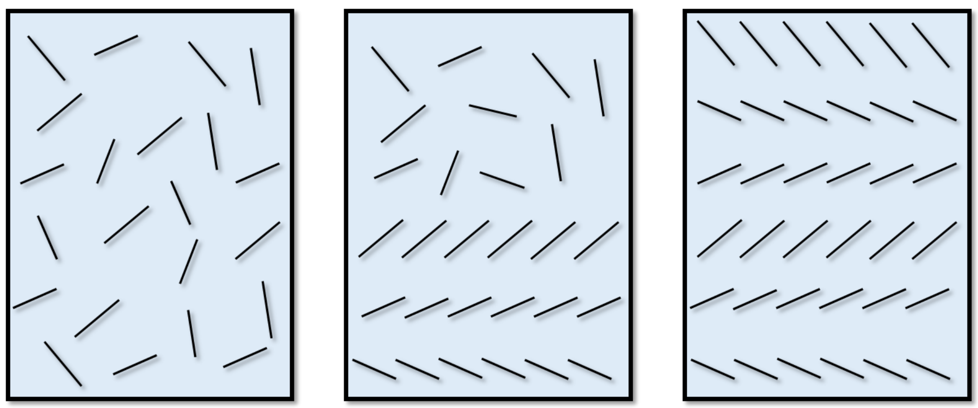

Figure 1.6. Cellulose nanocrystals are colloidally stable in aqueous suspension, and at low volume fractions these suspensions are isotropic (left). Above a critical concentration (c*), the particles will spontaneously align to form a lower chiral nematic phase and upper isotropic phase (center) which helps them maximize translational entropy, in keeping with Onsager's theory[44] for rigid rods. At high enough concentrations and provided the suspension is not kinetically arrested, full chiral nematic orientation can be attained (right).

A related set of works on nanochitin is available, beginning with the identification and characterization of its potential as a biobased nanomaterial[45] which sparked a cascade of investigations into its properties, and numerous comparisons to nanocellulose.[46] The existing body of literature on nanocellulose served as a template for the subsequent study of nanochitin, and which has come to be an important topic in the community of biobased nanomaterials research. With this development, efforts have emerged to formulate and characterize systems which make use of both materials simultaneously.[47]

1.3 Dissertation Scope

Three primary phenomena will be discussed in this work, pertaining to three different biobased nanomaterial systems. For each, we have focused on an aspect that is (*i*) specific to that material, (*ii*) of interest to the fundamental understanding thereof and (*iii*) useful in the pursuit of employing the material in real applications. In our first study (**Chapter 2**), we investigated shear behavior in micro/nanofibrillated cellulose (MNFC) suspensions. MNFC lacks the stabilizing charges found in many other biobased nanomaterial systems, which significantly influences the shear response. The lack of electrostatic repulsion creates a complex dynamic of flocculation and subsequent floc breakage under shear. We examined this behavior, its limits and tunability by quantifying the network structure using rheological tests and linking these measurements to visually observed microstructural features *in situ.* The findings of this work have implications for use of MNFC in 3D printing or coating applications, by identifying shear regimes which are likely to generate defects and inhomogeneities. The findings also highlight some underlying insights about the mechanics of the system, which imply a likeness to soft glassy materials. This relationship can be of interest in attempts to model the behavior of the system.

In the second study (**Chapter 3**), the chiral nematic ordering transition is examined for CNC suspensions. The liquid crystalline behavior is among the most avidly studied properties of CNCs, and a key parameter of this behavior is the minimum concentration required to drive phase separation (c^*). However, conventional methods to determine this value are typically slow and can be imprecise. To address this challenge, we posed the following question: do the interactions which drive phase separation exhibit an enthalpic component which can be detected calorimetrically? In this chapter, we present a new technique to characterize the concentration threshold for CNC suspensions, below which the system will remain isotropic and above which it will phase separate into anisotropic chiral nematic phase and an isotropic phase. The proposed method has the potential to expedite characterization of new samples and serve as a quality control tool, as well as opening the door to a discussion of the underlying thermodynamic mechanisms at play in the spontaneous phase separation of CNCs.

In the third study (**Chapter 4**), we branch out into the study of nanochitin. We make use of the opposite charges on nanochitin (positively charged) and CNF (negatively charged) to form ionic complexes, in which the microstructure properties are very finely tunable. The interactions between the nanoparticles are measured using isothermal titration calorimetry, which allows us to quantify the ratio at which the attractions are most relevant and decouple the complex pH effects of both systems. The microstructure of each component and various conditions for mixed systems of the two are characterized using rheology.

1.4 References

(1) De Smet, M. The New Plastics Economy: Rethinking the Future of Plastics & Catalysing Action; Ellen MacArthur Foundation, 2017.

(2) Su, Y.; Yang, B.; Liu, J.; Sun, B.; Cao, C.; Zou, X.; Lutes, R.; He, Z. Prospects for Replacement of Some Plastics in Packaging with Lignocellulose Materials: A Brief Review. *BioResources* **2018**, *13* (2), 4550–4576.

(3) Stoudmann, N.; Nowack, B.; Som, C. Prospective Environmental Risk Assessment of Nanocellulose for Europe. *Environ. Sci. Nano* **2019**, *6* (8), 2520–2531. https://doi.org/10.1039/C9EN00472F.

(4) Shak, K. P. Y.; Pang, Y. L.; Mah, S. K. Nanocellulose: Recent Advances and Its Prospects in Environmental Remediation. *Beilstein J. Nanotechnol.* **2018**, *9*, 2479–2498. https://doi.org/10.3762/bjnano.9.232.

(5) Atalla, R. H.; Atalla, R. S.; Agarwal, U. P. The Nanostructures of Native Celluloses, Their Transformations upon Isolation, and Their Implications for Production of Nanocelluloses. In *Nanocelluloses: Their Preparation, Properties, and Applications*; ACS Symposium Series; American Chemical Society, 2017; Vol. 1251, pp 1–18. https://doi.org/10.1021/bk-2017-1251.ch001.

(6) Habibi, Y. Key Advances in the Chemical Modification of Nanocelluloses. *Chem. Soc. Rev.* **2014**, *43* (5), 1519–1542. https://doi.org/10.1039/C3CS60204D.

(7) Habibi, Y.; Lucia, L. A.; Rojas, O. J. Cellulose Nanocrystals: Chemistry, Self-Assembly, and Applications. *Chem. Rev.* **2010**, *110* (6), 3479–3500. https://doi.org/10.1021/cr900339w.

(8) Moon, R. J.; Martini, A.; Nairn, J.; Simonsen, J.; Youngblood, J. Cellulose Nanomaterials Review: Structure, Properties and Nanocomposites. *Chem. Soc. Rev.* **2011**, *40* (7), 3941–3994. https://doi.org/10.1039/C0CS00108B.

(9) Johan Foster, E.; J. Moon, R.; P. Agarwal, U.; J. Bortner, M.; Bras, J.; Camarero-Espinosa, S.; J. Chan, K.; D. Clift, M. J.; D. Cranston, E.; J. Eichhorn, S.; M. Fox, D.; Y. Hamad, W.; Heux, L.; Jean, B.; Korey, M.; Nieh, W.; J. Ong, K.; S. Reid, M.; Renneckar, S.; Roberts, R.; Anne Shatkin, J.; Simonsen, J.; Stinson-Bagby, K.; Wanasekara, N.; Youngblood, J. Current Characterization Methods for Cellulose Nanomaterials. *Chem. Soc. Rev.* **2018**, *47* (8), 2609–2679. https://doi.org/10.1039/C6CS00895J.

(10) J. Benítez, A.; Walther, A. Cellulose Nanofibril Nanopapers and Bioinspired Nanocomposites: A Review to Understand the Mechanical Property Space. *J. Mater. Chem. A* **2017**. https://doi.org/10.1039/C7TA02006F.

(11) Mariano, M.; El Kissi, N.; Dufresne, A.; Mariano, M.; El Kissi, N.; Dufresne, A. Cellulose Nanomaterials: Size and Surface Influence on the Thermal and Rheological Behavior. *Polímeros* **2018**, *28* (2), 93–102. https://doi.org/10.1590/0104-1428.2413.

(12) Fan, Y.; Saito, T.; Isogai, A. Individual Chitin Nano-Whiskers Prepared from Partially Deacetylated α-Chitin by Fibril Surface Cationization. *Carbohydr. Polym.* **2010**, *79* (4), 1046–1051. https://doi.org/10.1016/j.carbpol.2009.10.044.

(13) Reza Barkhordari, M.; Fathi, M. Production and Characterization of Chitin Nanocrystals from Prawn Shell and Their Application for Stabilization of Pickering Emulsions. *Food Hydrocoll.* **2018**, *82*. https://doi.org/10.1016/j.foodhyd.2018.04.030.

(14) Ifuku, S.; Saimoto, H. Chitin Nanofibers: Preparations, Modifications, and Applications. *Nanoscale* **2012**, *4* (11), 3308–3318. https://doi.org/10.1039/C2NR30383C.

(15) Damian, L. Isothermal Titration Calorimetry for Studying Protein-Ligand Interactions. *Methods Mol. Biol. Clifton NJ* **2013**, *1008*, 103–118. https://doi.org/10.1007/978-1-62703-398-5_4.

(16) Loh, W.; Brinatti, C.; Tam, K. C. Use of Isothermal Titration Calorimetry to Study Surfactant Aggregation in Colloidal Systems. *Biochim. Biophys. Acta BBA - Gen. Subj.* **2016**, *1860* (5), 999–1016. https://doi.org/10.1016/j.bbagen.2015.10.003.

(17) Saarinen, T.; Haavisto, S.; Sorvari, A.; Salmela, J.; Seppälä, J. The Effect of Wall Depletion on the Rheology of Microfibrillated Cellulose Water Suspensions by Optical Coherence Tomography. *Cellulose* **2014**, *21* (3), 1261–1275. https://doi.org/10.1007/s10570-014-0187-5.

(18) Kontturi, E.; Laaksonen, P.; Linder, M. B.; Nonappa; Groechel, A. H.; Rojas, O. J.; Ikkala, O. Advanced Materials through Assembly of Nanocelluloses. *Adv. Mater.* **2018**, *30* (24), 1703779. https://doi.org/10.1002/adma.201703779.

(19) Belgacem, M. N.; Gandini, A. Production, Chemistry and Properties of Cellulose-Based Materials. In *Biopolymers – New Materials for Sustainable Films and Coatings*; Plackett, D., Ed.; John Wiley & Sons, Ltd, 2011; pp 151–178. https://doi.org/10.1002/9781119994312.ch8.

(20) Dufresne, A. Nanocellulose: A New Ageless Bionanomaterial. *Mater. Today* **2013**, *16* (6), 220–227. https://doi.org/10.1016/j.mattod.2013.06.004.

(21) Derakhshandeh, B.; Kerekes, R. J.; Hatzikiriakos, S. G.; Bennington, C. P. J. Rheology of Pulp Fibre Suspensions: A Critical Review. *Chem. Eng. Sci.* **2011**, *66* (15), 3460–3470. https://doi.org/10.1016/j.ces.2011.04.017.

(22) Hubbe, M. A.; Tayeb, P.; Joyce, M.; Tyagi, P.; Kehoe, M.; Dimic-Misic, K.; Pal, L. Rheology of Nanocellulose-Rich Aqueous Suspensions: A Review. *BioResources* **2017**, *12* (4), 9556–9661.

(23) Nechyporchuk, O.; Belgacem, M. N.; Pignon, F. Current Progress in Rheology of Cellulose Nanofibril Suspensions. *Biomacromolecules* **2016**, *17* (7), 2311–2320. https://doi.org/10.1021/acs.biomac.6b00668.

(24) Iotti, M.; Gregersen, Ø. W.; Moe, S.; Lenes, M. Rheological Studies of Microfibrillar Cellulose Water Dispersions. *J. Polym. Environ.* **2010**, *19* (1), 137–145. https://doi.org/10.1007/s10924-010-0248-2.

(25) Hill, R. J. Elastic Modulus of Microfibrillar Cellulose Gels. *Biomacromolecules* **2008**, *9* (10), 2963–2966. https://doi.org/10.1021/bm800490x.

(26) Nechyporchuk, O.; Belgacem, M. N.; Pignon, F. Rheological Properties of Micro-/Nanofibrillated Cellulose Suspensions: Wall-Slip and Shear Banding Phenomena. *Carbohydr. Polym.* **2014**, *112*, 432–439. https://doi.org/10.1016/j.carbpol.2014.05.092.

(27) Nazari, B.; Kumar, V.; Bousfield, D. W.; Toivakka, M. Rheology of Cellulose Nanofibers Suspensions: Boundary Driven Flow. *J. Rheol. 1978-Present* **2016**, *60* (6), 1151–1159. https://doi.org/10.1122/1.4960336.

(28) Saarikoski, E.; Saarinen, T.; Salmela, J.; Seppälä, J. Flocculated Flow of Microfibrillated Cellulose Water Suspensions: An Imaging Approach for Characterisation of Rheological Behaviour. *Cellulose* **2012**, *19* (3), 647–659. https://doi.org/10.1007/s10570-012-9661-0.

(29) Bjorkman. Floc Dynamics in Flowing Fibre Suspensions. *Nord. Pulp Pap. Res. J.* **2005**, *20* (02), 247–252. https://doi.org/10.3183/NPPRJ-2005-20-02-p247-252.

(30) Derakhshandeh, B.; Hatzikiriakos, S. G.; Bennington, C. P. J. The Apparent Yield Stress of Pulp Fiber Suspensions. *J. Rheol.* **2010**, *54* (5), 1137–1154. https://doi.org/10.1122/1.3473923.

(31) Li, M.-C.; Wu, Q.; Song, K.; Lee, S.; Qing, Y.; Wu, Y. Cellulose Nanoparticles: Structure–Morphology–Rheology Relationships. *ACS Sustain. Chem. Eng.* **2015**, *3* (5), 821–832. https://doi.org/10.1021/acssuschemeng.5b00144.

(32) Liu, D.; Chen, X.; Yue, Y.; Chen, M.; Wu, Q. Structure and Rheology of Nanocrystalline Cellulose. *Carbohydr. Polym.* **2011**, *84* (1), 316–322. https://doi.org/10.1016/j.carbpol.2010.11.039.

(33) Shafiei-Sabet, S.; Hamad, W. Y.; Hatzikiriakos, S. G. Rheology of Nanocrystalline Cellulose Aqueous Suspensions. *Langmuir* **2012**, *28* (49), 17124–17133. https://doi.org/10.1021/la303380v.

(34) Shafiei-Sabet, S.; Hamad, W. Y.; Hatzikiriakos, S. G. Influence of Degree of Sulfation on the Rheology of Cellulose Nanocrystal Suspensions. *Rheol. Acta* **2013**, *52* (8–9), 741–751. https://doi.org/10.1007/s00397-013-0722-6.

(35) Haywood, A. D.; Davis, V. A. Effects of Liquid Crystalline and Shear Alignment on the Optical Properties of Cellulose Nanocrystal Films. *Cellulose* **2017**, *24* (2), 705–716. https://doi.org/10.1007/s10570-016-1150-4.

(36) Ureña-Benavides, E. E.; Ao, G.; Davis, V. A.; Kitchens, C. L. Rheology and Phase Behavior of Lyotropic Cellulose Nanocrystal Suspensions. *Macromolecules* **2011**, *44* (22), 8990–8998. https://doi.org/10.1021/ma201649f.

(37) Haywood, A. D.; Weigandt, K. M.; Saha, P.; Noor, M.; Green, M. J.; Davis, V. A. New Insights into the Flow and Microstructural Relaxation Behavior of Biphasic Cellulose

Nanocrystal Dispersions from RheoSANS. *Soft Matter* **2017**, *13* (45), 8451–8462. https://doi.org/10.1039/C7SM00685C.

(38) Revol, J.-F.; Godbout, L.; Dong, X.-M.; Gray, D. G.; Chanzy, H.; Maret, G. Chiral Nematic Suspensions of Cellulose Crystallites; Phase Separation and Magnetic Field Orientation. *Liq. Cryst.* **1994**, *16* (1), 127–134. https://doi.org/10.1080/02678299408036525.

(39) Beck, S.; Bouchard, J. Ionic Strength Control of Sulfated Cellulose Nanocrystal Suspension Viscosity. *Tappi J.* **2016**, *15* (6), 363–372.

(40) Dong, X. M.; Kimura, T.; Revol, J.-F.; Gray, D. G. Effects of Ionic Strength on the Isotropic−Chiral Nematic Phase Transition of Suspensions of Cellulose Crystallites. *Langmuir* **1996**, *12* (8), 2076–2082. https://doi.org/10.1021/la950133b.

(41) Honorato-Rios, C.; Lehr, C.; Schütz, C.; Sanctuary, R.; Osipov, M. A.; Baller, J.; Lagerwall, J. P. F. Fractionation of Cellulose Nanocrystals: Enhancing Liquid Crystal Ordering without Promoting Gelation. *NPG Asia Mater.* **2018**, 1. https://doi.org/10.1038/s41427-018-0046-1.

(42) Klockars, K. W.; Tardy, B. L.; Borghei, M.; Tripathi, A.; Greca, L. G.; Rojas, O. J. Effect of Anisotropy of Cellulose Nanocrystal Suspensions on Stratification, Domain Structure Formation, and Structural Colors. *Biomacromolecules* **2018**, *19* (7), 2931–2943. https://doi.org/10.1021/acs.biomac.8b00497.

(43) Abitbol, T.; Kam, D.; Levi-Kalisman, Y.; Gray, D. G.; Shoseyov, O. Surface Charge Influence on the Phase Separation and Viscosity of Cellulose Nanocrystals. *Langmuir* **2018**. https://doi.org/10.1021/acs.langmuir.7b04127.

(44) Onsager, L. The Effects of Shape on the Interaction of Colloidal Particles. *Ann. N. Y. Acad. Sci.* **1949**, *51* (4), 627–659. https://doi.org/10.1111/j.1749-6632.1949.tb27296.x.

(45) Revol, J.-F.; Marchessault, R. H. In Vitro Chiral Nematic Ordering of Chitin Crystallites. *Int. J. Biol. Macromol.* **1993**, *15* (6), 329–335. https://doi.org/10.1016/0141-8130(93)90049-R.

(46) Teacă, C.-A.; Bodîrlău, R. Rheology and Processing of Nanocellulose, Nanochitin, and Nanostarch/Polymer Bionanocomposites. In *Rheology and Processing of Polymer Nanocomposites*; John Wiley & Sons, Ltd, 2016; pp 453–490. https://doi.org/10.1002/9781118969809.ch14.

(47) Gao, K.; Guo, Y.; Niu, Q.; Fang, H.; Zhang, L.; Zhang, Y.; Wang, L.; Zhou, L. Effects of Chitin Nanofibers on the Microstructure and Properties of Cellulose Nanofibers/Chitin Nanofibers Composite Aerogels. *Cellulose* **2018**, *25* (8), 4591–4602. https://doi.org/10.1007/s10570-018-1899-8.

CHAPTER 2

Shear-dependent Structures of Flocculated Micro/NanoFibrillated Cellulose (MFNC) in Aqueous Suspensions

2.1 ABSTRACT: Cellulosic nanomaterials constitute a topic of growing commercial interest for numerous applications, many of which demand a working knowledge of the rheology of the materials. We demonstrate here that aqueous suspensions of micro/nanofibrillated cellulose (MNFC) exhibit complex shear behavior governed primarily by fibrillar floc dynamics. Regimes corresponding to structure formation, persistence and breakdown are quantitatively differentiated. We assess the recovery of the network structure as a function of the applied breakdown conditions and identify critical conditions that characterize the floc dynamics as isotropic or anisotropic. A two-step yield dynamic generates persistent anisotropic flocs that effectively prohibit recovery of the initial gel structure under certain conditions. Processing within this stress window entails a risk of generating heterogenous, potentially irreproducible structures and properties. An in-depth understanding of the rheology of aqueous MNFC suspensions and their floc-dominated rather than fibril-dominated nature is critical to rationally tailoring properties through selection of judicious processing conditions.

2.2 INTRODUCTION

Nanocellulose remains an active and ubiquitous subject of research due to its many promising and diverse applications, including composite materials, food products, personal care, and medical supplies.[1,2] Of the many advantages of these cellulosic nanomaterials, some of the most important are their sustainability and biodegradability. They therefore constitute suitable candidates to replace conventional additives such as thickeners[3] and reinforcing agents[4] while reducing environmental impact.[5] These materials are generally classified according to their morphology: cellulose nanocrystal (CNC) and micro/nanofibrillated cellulose (MNFC), the latter of which is the subject of the present study. The stability of MNFC fibrils in aqueous medium is strongly dependent on both surface charge and fibrillar morphology.[6,7] Charges can result from residual functional groups present in the raw cellulose source[8,9] (*e.g.*, from hemicellulose or lignin) or from deliberate modification of the cellulose hydroxyl groups (*e.g.,* during TEMPO-mediated oxidation or carboxymethylation). **Figure 2.1** illustrates the hierarchical nature of an MNFC suspension. The elementary fibrils are held intact by hydrogen bonds between polymer chains. These fibrils form a highly entangled and flocculated network, thereby creating a heterogeneous slurry-like material that exhibits gel-like properties at concentrations as low as 0.1 wt%.[10,11]

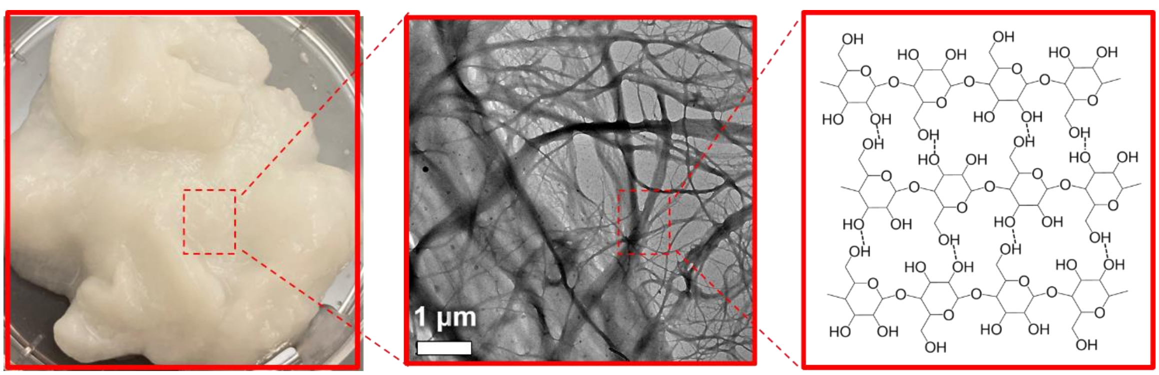

Figure 2.1. (*left*) Aqueous slurry of microfibrillated cellulose at 3.1 wt%. (*center*) Transmission electron microscopy image of a network of highly entangled fibrils exhibiting a wide diameter range. Fibrils are comprised of a highly crystalline assembly of cellulose macromolecule chains, as seen in the schematic on the right. (*right*) Chemical structure of a cellulose polymer wherein crystalline regions are held together by extensive hydrogen bonding. The multiscale dimensions typical of MNFC reflect the defibrillation process and the inherent structural hierarchy of cellulosic materials in nature.Of particular interest in this study is the relationship that exists

between microstructure and shear as both of these characteristics play pivotal roles in the practical use of these materials in various applications. Floc dynamics in heterogenous slurries create complex flow behavior in aqueous MNFC suspensions and have been the subject of limited investigation but remain inadequately understood.[11–15] Previous studies addressing this issue have focused on specific rheological phenomena such as wall slip,[16] shear banding[17] and yield stress,[18] and repeatedly point out that collecting accurate and relevant rheological measurements is nontrivial for these suspensions. We echo the sentiment that great care must be exercised to interpret results correctly.[17,18] To this point, the importance of boundary effects in MNFC suspensions has been described by Nazari *et al*.[18] in a detailed rheological study, which also served to quantify yield stresses for suspensions at concentrations above 2 wt% MNFC. They describe the formation of a dilute boundary layer during shear, especially at high concentrations. A similar assessment of wall depletion is also reported for lower concentrations by Saarinen *et al*.,[16] who emphasize the importance of boundary-dominated flow below the yield stress at 0.5 and 1 wt% MNFC. Nechyporchuk *et al*.[17] have examined the possibility of roughening plate surface topology to mitigate interfacial slip, which they suggested was of primary concern at low shear rates, in agreement with the observations by Saarinen *et al*.,[16] below the yield stress. Xu and Li[14] offer further insight into the yield stress and, in particular, its response to an added electrolyte, which can promote the formation of glassy clusters. Many of these prior findings stem from flocculation dynamics, which have been imaged by Saarikoski *et al*.[13] and Karpinnen *et al*.[12] *In-situ* descriptions of the development of flocs under increasing shear rates, along with accompanying size/shape analyses of the flocs, afford a complementary interpretation of unexpected rheological measurements, such as the "kink" or flow instability evident in the MNFC viscosity profile noted by Iotti *et al.*[19] and others.[12,17,18,20,21] The prevailing description of this unique behavior presumes anisotropic “log-roller” flocs under certain shear conditions and smaller isotropic flocs under more intense shear.[12,13] The formation and breakdown of flocs by these mechanisms have also been described for wood pulp fiber suspensions,[22,23] which possess significantly larger dimensions but similar flow properties.

Despite similar advances thus far, a comprehensive description of aqueous MNFC suspension dynamics under shear, including direct imaging of structural evolution, the correlation of structure with yield stress, and structure recovery following shear and thixotropic effects, remains missing. Of particular importance is how these related phenomena can be quantitatively correlated and controllably manipulated to optimize properties. Due to the large volume of studies performed on modified MNFC (such as TEMPO-oxidized CNF[24–29]), systems with fewer charges and more heterogeneous morphologies are less well understood by comparison. While this failing can likely be attributed to experimental challenges inherent in characterizing heterogeneous media, the industrial relevance of this type of MNFC cannot be denied in light of its lower cost and facile production. For these reasons, the present work seeks to directly relate the rheological measurements of heterogeneous MNFC to specific morphological phenomena, namely, the formation and development of flocculated structures. This course of study is necessary to establish reliable testing protocols and elucidate complex structural behavior that has proven difficult to observe or explain. We have detected a sensitive relationship between floc structures and shear responses of MNFC suspensions wherein the critical factor is shear *history*. This dependence is apparent in several instances, including, for example, floc behavior and the characteristic kink encountered during steady shear. In addition, we have investigated a complex multi-step yield behavior that appears to reflect a hierarchical fibril/floc network structure and relate directly to recovery of the broken structure. By combining such rheological measurements with direct visualization of the structure, we can draw connections between microstructure and flow behavior. A two-step yield process is indicative of hierarchical structure breakdown, which we explicitly identify and characterize with rheological measurements that confirm consistency and reproducibility. A key finding here is the dominant influence of floc morphology on structural development, which is not intuitive given the highly fibrillated nature of the system. The ability to predict the corresponding microstructure resulting from a variety of applied mechanical stimuli or vice-versa can be a valuable tool to guide selection of cellulosic nanomaterials for different applications and to expedite their processing and handling. This type of structure-property relationship has substantial implications for both process and product design with respect to nanocellulose applications.

2.3 EXPERIMENTAL

Preparation and characterization of MNFC suspensions. Sodium-form MNFC as a 3.1 wt% aqueous slurry ("cellulose nanofibrils") was purchased from the University of Maine Process Development Center. The concentration was adjusted by dilution with deionized water, followed by probe sonication (Cole-Parmer 750 W Ultrasonic Processor, 2000 J/g MNFC) to reduce fibrillar aggregation and improve sample homogeneity. Samples were stored under refrigeration prior to analysis to prevent bacterial growth. While the results provided here correspond to a 1 wt% MNFC aqueous suspension, tests were conducted on concentrations ranging from 0.5 to 3.1 wt% with similar results, as evidenced in the **Appendix B** (described in following sections). Further details regarding concentration effects can be found elsewhere.[10] To prepare the samples for transmission electron microscopy (TEM) imaging, a 10 μL drop of a 0.01 wt% MNFC suspension was placed on a carbon-coated copper TEM grid (300 mesh) and left to dry overnight at ambient temperature. Digital images were subsequently acquired on a JEOL 2000FX microscope operated at an accelerating voltage of 200 kV. Measured fibril diameters ranged from 5 to 200 nm, with a mean value of 33 nm and a mode of 5-10 nm (*cf.* **Figure A.1** in **Appendix A**). Further discussion regarding estimates of particle aspect ratios as determined by the Simha equation[30] and diffusion constants based upon a long thin rod approximation[31] can also be found in **Appendix A**. The MNFC surface charge was measured as 0.015 mmol/g with a Mutek particle charge detector by titration with poly(diallyldimethylammonium chloride).

Rheological analysis of MNFC suspensions. Steady and dynamic rheological tests were performed on either a stress-controlled rheometer or a DHR-3 Discovery Hybrid Rheometer (TA Instruments). Some experiments were repeated on both instruments to confirm reproducibility. Data were collected between concentric cylinders in which the aluminum cylindrical periphery was recessed and the gap between the inner and outer cylinders (with radii of 14 and 15 mm, respectively) was 1 mm. This setup was chosen to reduce water expulsion by mechanisms of wall depletion, inertia and compression, each of which can artificially increase the suspension concentration and influence the experimental results (as indicated[32] for parallel-plate measurements). Concentric-cylinder experiments were duplicated using serrated parallel plates to determine the influence of wall slip. Results reported here have been repeated in triplicate with a standard error of < 20% (including between rheometers). Representative viscosity profiles are provided rather than averaged data to avoid obscuring distinctive features at intermediate shear rates. An oscillatory pre-shear step of 60 s at a stress amplitude of 20 Pa and frequency of 0.5 rad/s, followed by recovery for 10 min, established a consistent starting structure after initial sample loading.[33–35] Steady-state apparent viscosities were measured by varying the shear rate from 0.01 to 1000 s^{-1} in both increasing and decreasing order to ascertain the effect of shear history. Each shear rate was applied for up to 12 min to ensure steady state was reached prior to data acquisition.

Oscillatory frequency sweeps (at a stress amplitude of 0.5 Pa) and stress amplitude sweeps (at a frequency of 0.5, 1.0 or 5.0 rad/s) were performed to obtain the dynamic storage and loss moduli (G' and G", respectively) and yield stress under different shear histories. The chosen stress amplitude of 0.5 Pa was confirmed to be within the linear viscoelastic regime by an oscillatory stress sweep.

To quantify microstructure recovery, a predetermined breakdown stress (up to 100 Pa) was applied for 5 min to rupture the microstructure, followed by a recovery time of 10 min at an oscillatory stress of 0.5 Pa (within the linear viscoelastic regime). During both breakdown and recovery, the frequency is held constant at 0.5 rad/s. Each sample was subjected to a frequency sweep (at 1 rad/s) before and after this procedure, and structure recovery was quantified here as the ratio of the final elastic modulus value to its initial value (G'/G_0').

Real-time images of structural evolution under shear were collected with a rheo-optical plate (TA Instruments) in conjunction with a digital camera and a 40-mm stainless steel, sandblasted parallel plate. In this parallel-plate arrangement, the lower plate is transparent, and the camera is placed beneath the plate to capture images of the structure in the flow and vorticity directions. A schematic diagram of this setup is depicted in **Figure A.2** in the **Appendix A**.

2.4 RESULTS & DISCUSSION

2.4.1 Structural evolution

The frequency spectra acquired from a 1 wt% MNFC suspension is displayed in **Figure 2.2a**. The entangled fibrillar network is manifested as a physical gel due to extensive aggregation and entanglement (as is visible in **Figure 2.1**), which is consistent with previous results obtained from analogous systems.[10,17] Signature features of network behavior in a 3-dimensional gel include G' exceeding G" over the entire frequency range examined and both moduli being independent of frequency.[36,37] This frequency sweep is conducted within the linear viscoelastic region as determined by oscillatory stress sweep shown in **Figure 2.2b**. The oscillatory stress sweep shows a small overshoot in the value of G'' near the end of the linear viscoelastic regime. This "weak strain overshoot" behavior is a typical feature of soft glassy materials[38,39] with attractive interactions between particles. In many systems such behavior is attributed in systems to large scale structural rearrangement.[40] In the case of MNFC, the attractions between flocs (due hydrogen bonding) could cause the viscous modulus to increase slightly as the structure transitions from an intact network to a broken system of fibrillar flocs, which have a brief opportunity to interact with each other before the increased oscillatory stress separates them entirely. However, a full understanding falls beyond the scope of this study.

The corresponding viscosity profile measured from the same sample is presented in **Figure 2.2c** as a function of shear rate. We first note the absence of a Newtonian plateau, which is consistent with gel-like properties. This shear-thinning profile is characteristic of a yield-stress material (for which the slope is approximately –1 at low shear rates) and possesses a distinctive and reproducible "kink" at intermediate shear rates. Yield stress behavior is also indicated by the plateau of shear stress observed at low shear rates in **Figure 2.2d**.

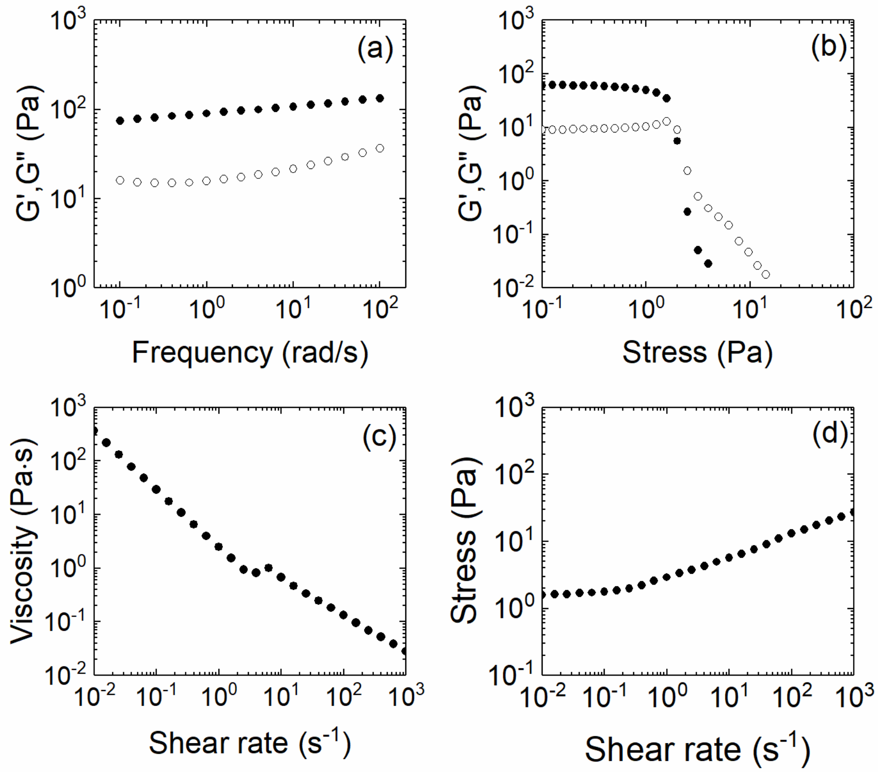

Figure 2.2. (a), G' (filled circles) and G" (open circles) measured as a function of oscillatory frequency in the linear viscoelastic regime from a 1 wt% MNFC suspension, confirming that G' > G" and both moduli are nearly independent of frequency, conditions that are indicative of a percolated gel network. (b), Oscillatory stress sweep indicates that the linear viscoelastic region extends to ~1.5 Pa. (c), Viscosity profile reveals that the suspension is shear-thinning and possesses a distinctive kink at intermediate shear rates (1-10 s^{-1}). (d) Shear stress versus shear rate profile revealing a yields stress (extrapolated to low shear rate).

The dominant influence on suspension viscosity is shear-induced rearrangement of flocs. More specifically, changes in the floc shape and size dictate the flow properties of the bulk system.[12] The kink evident in **Figure 2.2c** is a result of the floc mechanics that accompany breakdown of the structure at various shear rates, as illustrated in **Figure 2.3**. Initially, the fibrils exist as a percolated gel network at rest (**Figure 2.3a**). At low shear rates, the network flows in this state. Under intermediate shear, the continuous network is disturbed and rifts begin to develop in the vorticity direction, perpendicular to the direction of shear. As the system reaches steady state, these voids grow and eventually separate the network into a heterogeneous system of anisotropic floc structures that move with a log-rolling motion (**Figure 2.3b**). Anisotropic log-rolling flocs have been predicted[41] by simulations for some model systems under various conditions of shear and confinement. This motion persists as the shear rate increases further up to a critical range at which the shear is strong enough to disrupt the anisotropic structures. At these conditions, the flocs begin to split into smaller, isotropic, spheroidal units (**Figure 2.3c**) in a transition that is similar to behavior observed in attractive colloids.[42]

The transition from anisotropic to isotropic flocs is deemed responsible for the kink in the viscosity profile. As the shear rate increases further, the isotropic flocs continue to split and decrease in size, contributing to the shear-thinning behavior. This proposed sequence of floc evolution is confirmed in **Figure 2.4** using real-time rheo-optical imaging by observing the initial suspension structure at rest (**Figure 2.4a**), as well as structure progression at selected shear rates of 1, 10 and 100 s^{-1}. During and after application of a shear rate of 1 s^{-1} (**Figures 2.4b** and **2.4f**, respectively), the structure is indistinguishable from the initial state and appears as a homogeneous, intact network spanning the entire field of view. Application of shear at a rate of 10 s^{-1} promotes the formation of anisotropic rolling flocs that persist throughout the field of view (**Figure 2.4c**). It is important to recognize that elongated (log-shaped) flocs are oriented normal to the flow direction. Upon cessation of this intermediate shear in **Figure 2.4g**, distinct holes indicative of sample heterogeneity remain in the structure. An image of the sandblasted plate with no sample in the gap is included in **Figure 2.4e** to identify the background visible in the voids. Upon application of a high shear rate (100 s^{-1} in **Figure 2.4d**), these heterogeneities are altogether eliminated and the suspension structure once again becomes homogeneous, which is corroborated when the shear ceases (**Figure 2.4h**). Taken together, this sequence of images provides direct experimental evidence that supports the floc breakdown mechanism pictured in **Figure 2.3**.

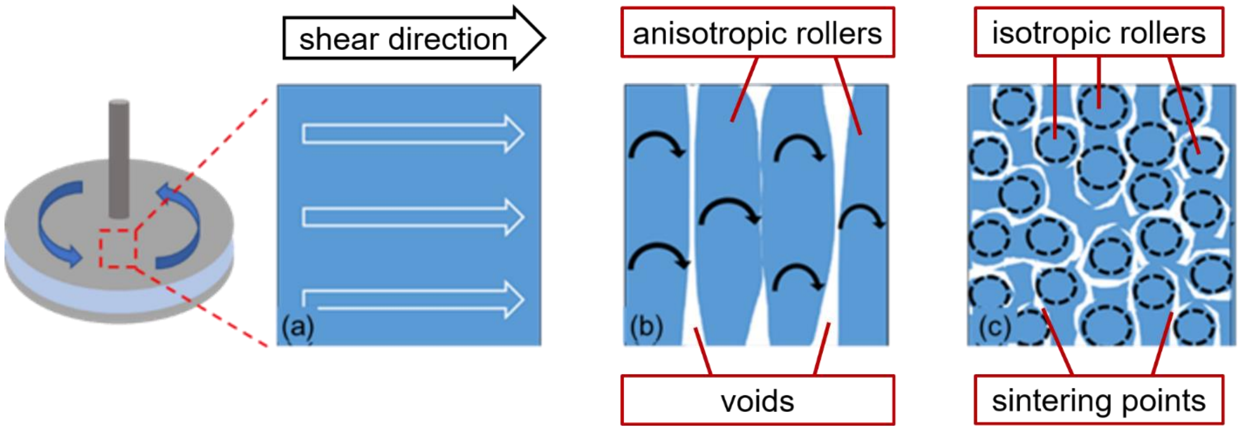

Figure 2.3. Schematic illustration of the floc breakdown sequence for fibrillar MNFC suspension under increasing shear conditions. Blue regions indicate fibril networks or flocs, while white regions indicate voids between fibril structures. Direction of shear is left to right (a) homogeneous network at rest and low shear rates, (b) anisotropic log-rolling flocs at intermediate shear rates, and (c) isotropic rolling flocs at high shear rates. Dashed lines indicate distinct flocs (approximately spherical) which move with a rolling action and sinter together upon cessation of flow to restore the homogenous network represented in (a)

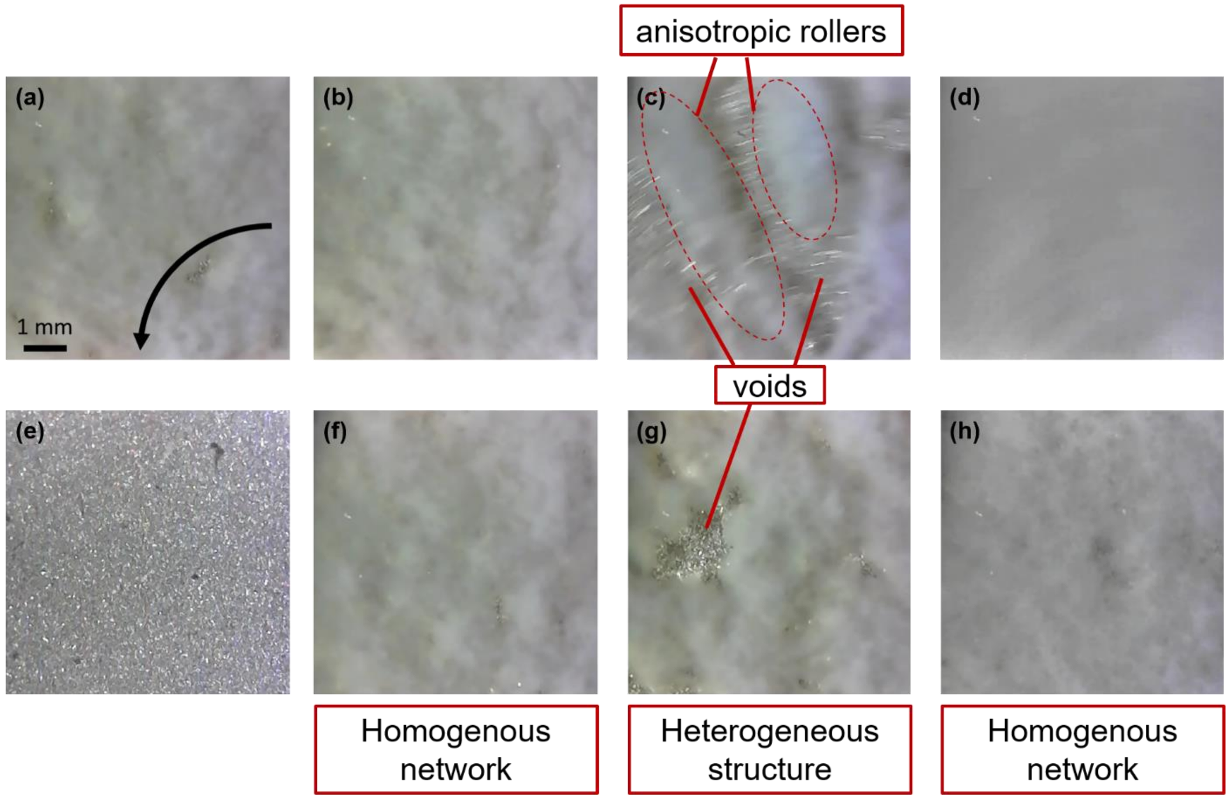

Figure 2.4. Rheo-optical images of 1 wt% MNFC suspension during and after application of steady shear at different shear rates: (a) initial sample structure at rest, (b) at 1 s^{-1}, (c) at 10 s^{-1}, (d) at 100 s^{-1}, (e) background plate for reference (no sample), (f) after 1 s^{-1}, (g) after 10 s^{-1}, and (h) after 100 s^{-1}. At applied shear rate 10 s^{-1}, voids develop between anisotropic flocs, and the textured silver surface of the upper rheometer plate can be seen between these features (c,g). An example of an anisotropic cylindrical (log-rolling) floc is visible in (c). Approximately 1 mm across, it spans from the upper left corner of the image to the center bottom edge.

2.4.2 Shear history

The implications associated with isotropic and anisotropic shear regimes of floc flow behavior prompt further investigation wherein we have examined two different steady shear sequences. In this context, the term "quench" is used to indicate cessation of shear or how we end our shearing experimental protocol; "fast quench" indicating direct cessation of experiments from (or after) a high shear rate, and "slow quench" indicating gradual cessation by reducing shear rate from high to low before coming to rest. This nomenclature is adopted from related experiments by Moghimi et al.[42] In slow quench tests, the first shear sweep is performed from low to high shear rate, followed by a second sweep from high to low shear rate, and a final low-to-high shear sweep. Conversely, fast quench experiments are conducted from an initial low-to-high shear sweep, immediately followed by an identical low-to-high sweep only. Representative data acquired from 1 wt% MNFC suspensions are presented in **Figure 2.5**, although we hasten to point out that similar results are observed for a range of concentrations up to 3 wt% (*cf.* **Figure A.3** in the **Appendix A**). These results unequivocally confirm that shear history has a pronounced effect on flow properties. Fast-quench tests (**Figure 2.5a,b** red squares) result in full recovery of the initial low-shear properties (*i.e.*, the viscosity and shear stress evaluated at low shear rates) from the initial increasing sweep (black circles) even without a rest period between the steps. On the other hand, in the case of the slow-quench conditions, values of low-shear properties from the initial increasing shear sweep (**Figure 2.5c**,**d** black circles) are not recovered in the subsequent steps (**Figure 2.5c,** blue triangles and red squares), even if the system is allowed to rest for 15 min before the final increasing shear sweep. Below, we endeavor to explain this difference in the reverse context of the structure breakdown mechanism previously described with regard to **Figure 2.3**.

Under fast-quench conditions, the gel network reforms from a state of small, isotropic flocs, which develop at high shear rates during the first shear sweep (**Figures 2.3c**) and form a quasi-homogeneous medium (**Figures 2.4d** and **2.4h**), prior to the start of the second sweep. The homogenous network depicted in **Figure 2.4h** is known to assemble from small isotropic flocs that result from the high-shear breakup of the intermediate structures depicted in **Figure 2.4g.** While these small isotropic flocs are difficult to visualize discretely at the concentration pictured here, extensive floc size analysis and imaging has been conducted by previous researchers.[15,16] During the slow-quench sequence, the small isotropic flocs are subjected to intermediate and low shear rates in the second (decreasing) shear sweep, which gives them the opportunity to reorganize into the cylindrical (log-rolling) flocs characteristic of these conditions (**Figures 2.3b** and **2.4d**)

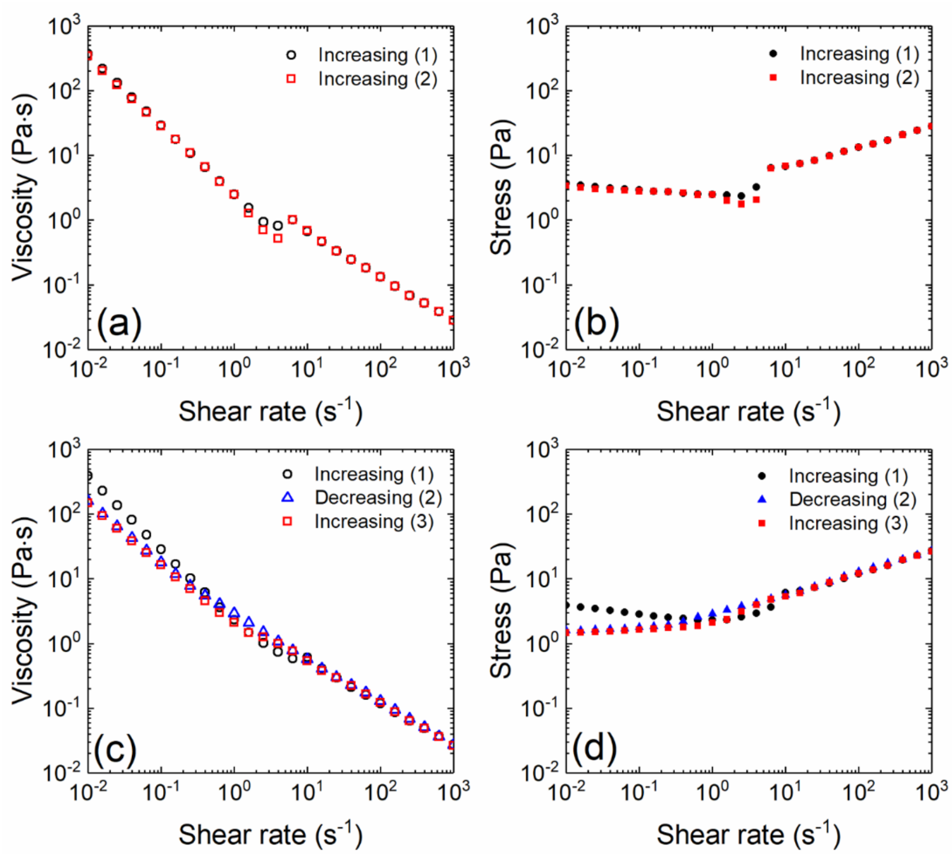

Figure 2.5. (a) Viscosity profile and (b) shear stress for fast quench test conditions; (c) viscosity profile and (d) shear stress for slow quench conditions (see the symbol legend in each case). The slow quench consists of 3 successive shear sweeps: increasing shear rate (1), then decreasing shear rate (2) and increasing shear rate (3). The fast quench subjects the specimen to two back-to-back sweeps of increasing shear rate. In (c) and (d), the low shear viscosity and shear stress do not recover their initial values due to locked-in log-rolling structures (depicted in **Figure 2.3b** and seen in **Figure 2.4c**).

The spacing between these anisotropic structures is expected to be too large for them to rejoin and subsequently form a homogeneous network when shear ceases. As a result, the measured stress and low-shear viscosity are depressed relative to the original network structure. All measurements appear to be affected up to ~10 s^{-1} of the final increasing sweep. At this shear rate, the suspension is once again exposed to the high shear rates that form small isotropic flocs. Images of the gel structure under shear in **Figure 2.4** provide convincing support for making a distinction between the two shear-history regimes of slow and fast quench, and further raise an important issue regarding the identification of the range of shear rates (or applied stresses) that fall into each category. To address this point in more quantitative fashion, we employ oscillatory shear, discussed below.

2.4.3 Microstructure recovery

As a consequence of the shear-dependent floc structures observed under steady-shear conditions, we now seek to characterize the recovery behavior of MNFC physical gels from different shear-generated floc regimes and examine how network structure is affected by specific stress conditions and, in turn, how this relationship governs the ultimate network strength. To elucidate the effect of breakdown condition on gel structure, microstructure recovery is measured here according to a protocol that is similar to one previously employed.[33,34] The microstructure recovery protocol used in this work is a four step procedure as follows:

(*i*) Initial structure characterization by frequency sweep (G'_0) (black dashed line in **Figure 2.6a**, black symbols in **Figure 2.6b**); (*ii*) Breakdown stress application (**Figure 2.6a**, time 0 to 300 s); (*iii*) Recovery interval (**Figure 2.6a**, time 300 to 900 s); (*iv*) Final structure characterization by frequency sweep of final modulus (G') (**Figure 2.6b,** for representative breakdown stresses in red, blue and green symbols) and normalized final modulus as G'/G'_0 (**Figure 2.6c**).

The results reflect the same difference observed in the fast- *vs*. slow-quench steady-shear experiments: the *most recently applied* shear level determines the recovery of the structure.

According to the results displayed in **Figure 2.6c**, application of a high stress (> 17 Pa) promotes complete recovery of the gel network ($G'/G_0' \sim 1$) after 10 min (although the actual recovery occurs much faster). A low stress (< 1.5 Pa) within the linear viscoelastic regime (**Figure 2.2b**) has relatively little impact on the ultimate network structure. In the intermediate stress region (between 1.5 and 17 Pa), however, network structure recovery is sensitively dependent on the applied breakdown conditions. Incomplete network recovery at intermediate stress levels is

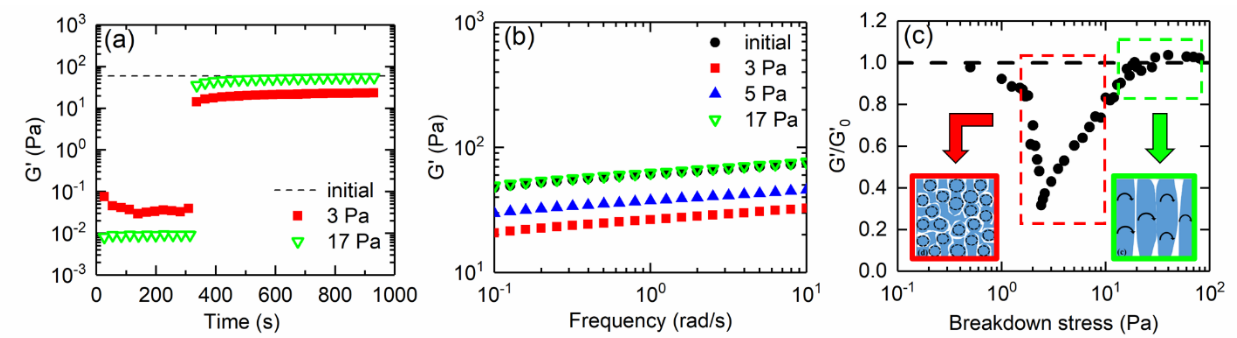

Figure 2.6. Dependence of final gel modulus (G') on breakdown stress: (a) time sweep of breakdown (3 or 17 Pa) and recovery (0.5 Pa) periods, (b) final frequency sweep after 3, 5, and 17 Pa breakdown periods, (c) relative final gel modulus with respect to applied breakdown stress. At intermediate values of applied oscillatory stress (red boxed region), the structure develops anisotropic flocs (left inset) which are unable to reform a percolated network. At high oscillatory stresses (green boxed region), the structure is split into uniform isotropic flocs (right inset) which pack more efficiently and thus recover the full initial gel modulus.

attributed to the same structure breakdown depicted in **Figure 2.3** and reproduced for convenience as insets in **Figure 2.6c**. Although this breakdown sequence is initially observed under steady shear, the structure is anticipated to respond in similar fashion to increasing stress amplitude during oscillatory shear. This expectation is supported by heterogeneous structures detected in the *in-situ* rheometer images during oscillatory tests (**Figure A.4**), which are indistinguishable from those of the steady shear tests. If this equivalence is valid, we expect that a range of intermediate stress conditions exists in which the resulting structure resembles **Figure 2.3b**, namely, anisotropic log-rolling flocs separated by large voids. The mechanism of microstructure recovery depends on fibrillar contact points and floc sintering, in which case it follows that the presence of voids will hinder recovery of the initial network. This explains the stress regime resulting in incomplete recovery from 1.5 to 17 Pa. The decreasing recovery from *ca*. 1-2 Pa in **Figure 2.6c** suggests that anisotropic flocs are developing and separating farther apart as the stress is increased. Similarly, we infer that beyond this range the log-rolling flocs have begun to transition to isotropic flocs, possibly decreasing in size at escalating stress levels, as described by Saarikoski *et al.*[13] Since isotropic flocs pack more efficiently and possess more contact points, the network structure is increasingly able to recover its initial elasticity. This echoes the behavior observed in the fast-quench steady-shear tests described in the previous section. The quantitative relationship between extent of recovery and applied stress amplitude is a topic that certainly merits additional study.

Related shear-dependent recovery behavior has been observed by Moghimi *et al.*[42] for colloidal gels and by Burns *et al.*[33] for nanodiamond suspensions. In both systems, intermediate breakdown conditions result in weaker network structures than those subjected to more severe breakdown conditions. In the case of colloidal gels, the dynamic mechanism of breakdown/recovery is comparable to the behavior described herein and relies on the formation of anisotropic log-rolling flocs, as confirmed by Brownian Dynamics simulations. Such similarity sheds light on the structural interpretation of MNFC suspensions subjected to shear. These similarities indicate that it may be more accurate to envisage the suspension as a system of flocs, rather than as a system of fibrils. While systems composed of TEMPO-oxidized or otherwise modified CNF might follow models of repulsive colloidal fibrils,[43] the rheological behavior of low-charge, aggregated MNFC suspensions appears to be better described in terms of attractive flocs rather than by the dynamics of individual fibrils. A critical distinction in the present system is most likely the low surface charge of the MNFC (0.015 meq/g), which might be unable to overcome the attraction of van der Waals interactions and extensive interfibrillar hydrogen bonding. The nanodiamond system examined by Burns *et al.*[33] also consists of attractive flocs. In that instance, however, the system behaves as a hierarchy of tightly bound aggregates which could flocculate together to form more loosely arranged structural elements. The reported minimum recovery at intermediate stress levels is attributed to the breakdown of loosely bound flocs, whereas smaller, tightly associated aggregates remain intact. In both these systems and in the MNFC suspensions investigated here, weak attraction of flocs results in intermediate shear-dependent structures, creating distinct regimes of flow-induced morphological development.

2.4.4 Two-step yield

On the basis of the complexity accompanying structure buildup and breakdown, apparent yield stress constitutes a relevant property by which to characterize and predict the behavior of MNFC suspensions. Keeping in mind that measurements of yield stress are most certainly impacted by shear history, we have considered two experimental strategies in this study. From steady-shear experiments, we can extract the dynamic yield stress from the stress plateau at low shear rates.[15,44–46] As pointed out by Fall *et al.*,[47] however, this method can be misleading for complex systems with time-dependent or shear-history effects. For this reason, we also discern the static yield point from plots of elastic stress as a function of oscillatory strain, where the elastic stress is calculated from the product of strain and the elastic (storage) modulus. Prior studies have established that the maximum elastic stress provides a systematic and reliable measure of the yield stress.[18,33,34,44] **Figure 2.2d** displays the dynamic yield stress obtained from steady shear measurements of a 1 wt% MNFC suspension. This is typically obtained by extrapolation of the data to zero shear rate. In our figure we see that this stress (shown only up to low shear rates as the value seems flat) reveals the yield stress is ~1.5 Pa, which is in favorable agreement with significant experimental phenomena already mentioned. First, from the microstructure recovery trials, the onset of incomplete recovery occurs at an applied breakdown stress of ~1.5 Pa (**Figure 2.6c**). Taken together, these results indicate that ~1.5 Pa is the stress required to sustain anisotropic flocs. Moreover, the viscosity kink apparent in steady-shear sweeps (**Figure 2.2c**) corresponds to a stress of 1.5 Pa, followed by a sharp increase to a higher stress (~10 Pa) with increasing shear rate (**Figure 2.2d**). This sudden increase is attributed here to the transition from anisotropic to isotropic flocs as the higher shear rate overcomes the stress required to break apart the anisotropic flocs.

Alternatively, the yield stress deduced from the elastic stress approach is provided in **Figure 2.7** In this case, the maximum in the elastic stress corresponding to the yield point provides further confirmation of a structural transition at the same critical value of 1.5 Pa. These data also reveal additional insight into the structural rearrangement of MNFC. While a plot of elastic stress as a function of strain typically exhibits a single maximum at the yield point,[35,44] this MNFC suspension possesses two local maxima at different strain levels. The existence of dual peaks could arise from wall slip or some other measurement artifact, but repeated tests conducted with

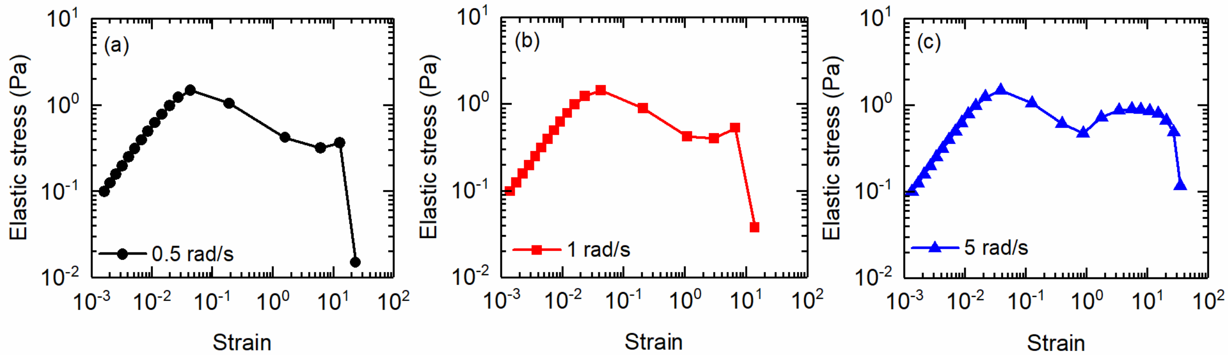

Figure 2.7. Oscillatory stress sweeps demonstrate two step yield by the elastic stress method, shown for different frequencies: (a) 0.5 rad/s, (b) 1 rad/s, (c) 5 rad/s. Primary yield stress is observed at 1.5 Pa regardless of frequency and is associated with the transition from a continuous network to anisotropic log-rolling flocs. Secondary yield stress shows some frequency dependence and marks the transition from anisotropic to isotropic flocs. Two step yield behavior is most pronounced at high frequencies (c), indicating the anisotropic flocs possess a shorter characteristic time scale than the original network structure

serrated plates at different frequencies have come to reveal that this feature is inherently related to structure breakdown. On the basis of this finding, we therefore propose the incidence of a two-step yield mechanism, which is consistent with the progression of structure breakdown previously suggested for the suspension in **Figure 2.3**. Recalling the different aspects of structure breakdown for this system, we assign a yield stress to each of the two transitions to explain this two-peak behavior. In this case, the first (or primary) yield stress represents the transition from a percolated network structure (**Figure 2.3a**) to one of log-rolling, anisotropic flocs (**Figure 2.3b**). Likewise, the secondary yield stress indicates a transition from anisotropic to isotropic flocs (**Figure 2.3c**). Furthermore, considering the microstructure recovery from the perspective of a two-step yield, we suggest that the structure overcomes the first yield stress but not the second in the regime of poor recovery (at intermediate stress values). The regime of inferior recovery begins at a stress of ~1.5

Pa (**Figure 2.6c**), and elastic stress measurements identify an initial or "primary" yield stress (τ_{y1}) of 1.5, which is independent of frequency.

Although the primary yield stress is frequency independent, an increase in oscillatory frequency promotes a systematic increase in the stress associated with the second maximum (τ_{y2}), from 0.36 Pa at 0.5 rad/s (**Figure 2.7a**) to 0.53 Pa at 1 rad/s (**Figure 2.7b**) and 0.90 Pa at 5 rad/s (**Figure 2.7c**). This relationship implies a time dependence of the isotropic floc behavior. At higher frequencies (shorter time scales) the measured response is more elastic. Frequency-dependent yield behavior has also been recorded for cellulose nanocrystals, where higher frequency resulted in a higher measured yield strain. Derakshandeh *et al.*[48] credit their observation to the increasing effect of Brownian motion at low frequencies. They contend that facilitated local particle rearrangement promotes suspension flow. This agrees favorably with what is observed for colloidal glasses of spherical particles,[49] which we have already pointed out exhibit several parallels with MNFC suspensions. However, if the micron to millimeter size scales of interest in the present system are considered, it is highly unlikely that Brownian forces are responsible for frequency dependence here. Hill[36] also predicts that Brownian forces are negligibly weak in this system. A more likely reason for such frequency dependence remains unclear at the present time, but warrants future study. The hypothesis of a two-step yield mechanism is predicated on reports that other systems display hierarchical structure and similar rheological behavior.[50,51] One of these, a model colloidal gel composed of spherical poly(methyl methacrylate) particles stabilized by chemically grafted poly(hydrostearic acid), exhibits[42,50] both the two-step yield behavior and microstructure recovery sequence encountered in this work. This further corroborates that treating MNFC suspensions as flocs, rather than fibrillar systems, can be more descriptive of their physical behavior.

This fundamental distinction between flocs and fibrils is of paramount importance to any effort that endeavors to model and/or predict material behavior. Moreover, since MNFC is becoming increasingly essential as a rheological modifier in coatings and 3D printing inks, a thorough understanding of its structural features and their response to shear is crucial to designing devices that rely on flow. Operating in the intermediate shear regime will lead to the development of persistent log-rolling flocs, which are likely to manifest as defects in a 3D-printed structure or a coating applied, for example, by doctor-blade or draw-rod methods. Of neglected significance is the *cessation* of shear. If a suspension is purposefully subjected to high stresses during processing with the intention of generating a homogeneous microstructure, that benefit could be completely lost if the shear rate is reduced gradually (as in the slow quench) rather than abruptly (as in the fast quench). While this study has successfully identified several rheo-optical features of MNFC suspensions that (*i*) help to explain the origin of experimental observations and (*ii*) establish the dominant role of flocs in hierarchical structure breakdown/recovery, interesting scientific questions remain to be answered regarding this complex system. One of these issues is the range over which the mechanisms described here apply. While these are believed to be specific to the gel regime, they could depend sensitively on dispersion quality and suspension concentration. The nature of the recovered structure as a function of breakdown condition is another topic that deserves further study, as is the behavior of the secondary yield stress under different shear conditions, especially with regard to changing oscillatory frequency. Our results provide insight into the flow behavior and accompanying structure of MNFC suspensions and, by doing so, confirm the complexity of these systems.

2.5 CONCLUSIONS

Distinct structural regimes of MNFC suspensions under shear flow have been observed and explained based on floc mechanics. Differences in low-shear viscosity following fast and slow quench conditions, the window of minimum structure recovery following oscillatory shear, and the existence of a two-step yield mechanism can all be related to a systematic progression of floc structures from a homogeneously percolated network through an anisotropic log-rolling regime at intermediate shear to a system of uniform, isotropic flocs at high shear. Favorable quantitative agreement is achieved between all the rheological measurements performed here, with a critical stress of 1.5 Pa corresponding to the primary yield stress from elastic stress measurements, as well as the onset of incomplete structure recovery, the viscosity kink and the dynamic yield stress from slow-quench flow curves. In summary, all of the results reported here and their similarities with previously documented systems make a strong case for interpreting MNFC morphologies on the basis of flocs rather than fibrils, even though the system is fundamentally an aqueous suspension of fibrils. The hierarchical approach proposed here to elucidate flow-induced structure in MNFC suspensions explains a number of interesting experimental observations and provides a largely unexplored means by which to understand and control flow-related properties.

2.6 ACKNOWLEDGMENTS

The authors acknowledge the Eastman Center of Excellence at North Carolina State University for supporting this work. This work was performed in part at the Analytical Instrumentation Facility (AIF) at North Carolina State University, which is supported by the State of North Carolina and the National Science Foundation (award number ECCS-1542015). The AIF is a member of the North Carolina Research Triangle Nanotechnology Network (RTNN), a site in the National Nanotechnology Coordinated Infrastructure (NNCI).

2.7 REFERENCES

(1) Klemm, D.; Cranston, E. D.; Fischer, D.; Gama, M.; Kedzior, S. A.; Kralisch, D.; Kramer, F.; Kondo, T.; Lindström, T.; Nietzsche, S.; Petzold-Welcke, K.; Rauchfuß, F. Nanocellulose as a Natural Source for Groundbreaking Applications in Materials Science: Today's State. *Mater. Today* **2018**, *21* (7), 720–748. https://doi.org/10.1016/j.mattod.2018.02.001.

(2) Moon, R. J.; Martini, A.; Nairn, J.; Simonsen, J.; Youngblood, J. Cellulose Nanomaterials Review: Structure, Properties and Nanocomposites. *Chem. Soc. Rev.* **2011**, *40* (7), 3941–3994. https://doi.org/10.1039/C0CS00108B.

(3) Dimic-Misic, K.; Gane, P. A. C.; Paltakari, J. Micro- and Nanofibrillated Cellulose as a Rheology Modifier Additive in CMC-Containing Pigment-Coating Formulations. *Ind. Eng. Chem. Res.* **2013**, *52* (45), 16066–16083. https://doi.org/10.1021/ie4028878.

(4) Abd El-Fattah, M.; Hasan, A. M. A.; Keshawy, M.; El Saeed, A. M.; Aboelenien, O. M. Nanocrystalline Cellulose as an Eco-Friendly Reinforcing Additive to Polyurethane Coating for Augmented Anticorrosive Behavior. *Carbohydr. Polym.* **2018**, *183*, 311–318. https://doi.org/10.1016/j.carbpol.2017.12.084.

(5) Wei, H.; Rodriguez, K.; Renneckar, S.; Vikesland, P. J. Environmental Science and Engineering Applications of Nanocellulose-Based Nanocomposites. *Env. Sci Nano* **2014**, *1* (4), 302–316. https://doi.org/10.1039/C4EN00059E.

(6) Isogai, A.; Saito, T.; Fukuzumi, H. TEMPO-Oxidized Cellulose Nanofibers. *Nanoscale* **2011**, *3* (1), 71–85. https://doi.org/10.1039/C0NR00583E.

(7) Chinga-Carrasco, G. Cellulose Fibres, Nanofibrils and Microfibrils: The Morphological Sequence of MFC Components from a Plant Physiology and Fibre Technology Point of View. *Nanoscale Res. Lett.* **2011**, *6* (1), 417. https://doi.org/10.1186/1556-276X-6-417.

(8) Xiang, W.; Preisig, N.; Ketola, A.; Tardy, B. L.; Bai, L.; Ketoja, J. A.; Stubenrauch, C.; Rojas, O. J. How Cellulose Nanofibrils Affect Bulk, Surface, and Foam Properties of Anionic Surfactant Solutions. *Biomacromolecules* **2019**, *20* (12), 4361–4369. https://doi.org/10.1021/acs.biomac.9b01037.

(9) Xiang, W.; Preisig, N.; Laine, C.; Hjelt, T.; Tardy, B. L.; Stubenrauch, C.; Rojas, O. J. Surface Activity and Foaming Capacity of Aggregates Formed between an Anionic Surfactant and Non-Cellulosics Leached from Wood Fibers. *Biomacromolecules* **2019**, *20* (6), 2286–2294. https://doi.org/10.1021/acs.biomac.9b00243.

(10) Pääkkö, M.; Ankerfors, M.; Kosonen, H.; Nykänen, A.; Ahola, S.; Österberg, M.; Ruokolainen, J.; Laine, J.; Larsson, P. T.; Ikkala, O.; Lindström, T. Enzymatic Hydrolysis Combined with Mechanical Shearing and High-Pressure Homogenization for Nanoscale Cellulose Fibrils and Strong Gels. *Biomacromolecules* **2007**, *8* (6), 1934–1941. https://doi.org/10.1021/bm061215p.

(11) Frisoni, G.; Baiardo, M.; Scandola, M.; Lednická, D.; Cnockaert, M. C.; Mergaert, J.; Swings, J. Natural Cellulose Fibers: Heterogeneous Acetylation Kinetics and Biodegradation Behavior. *Biomacromolecules* **2001**, *2* (2), 476–482. https://doi.org/10.1021/bm0056409.

(12) Karppinen, A.; Saarinen, T.; Salmela, J.; Laukkanen, A.; Nuopponen, M.; Seppälä, J. Flocculation of Microfibrillated Cellulose in Shear Flow. *Cellulose* **2012**, *19* (6), 1807–1819. https://doi.org/10.1007/s10570-012-9766-5.

(13) Saarikoski, E.; Saarinen, T.; Salmela, J.; Seppälä, J. Flocculated Flow of Microfibrillated Cellulose Water Suspensions: An Imaging Approach for Characterisation of Rheological Behaviour. *Cellulose* **2012**, *19* (3), 647–659. https://doi.org/10.1007/s10570-012-9661-0.

(14) Xu, H.-N.; Li, Y.-H. Decoupling Arrest Origins in Hydrogels of Cellulose Nanofibrils. *ACS Omega* **2018**, *3* (2), 1564–1571. https://doi.org/10.1021/acsomega.7b01905.

(15) Lê, H. Q.; Dimic-Misic, K.; Johansson, L.-S.; Maloney, T.; Sixta, H. Effect of Lignin on the Morphology and Rheological Properties of Nanofibrillated Cellulose Produced from γ-Valerolactone/Water Fractionation Process. *Cellulose* **2018**, *25* (1), 179–194. https://doi.org/10.1007/s10570-017-1602-5.

(16) Saarinen, T.; Haavisto, S.; Sorvari, A.; Salmela, J.; Seppälä, J. The Effect of Wall Depletion on the Rheology of Microfibrillated Cellulose Water Suspensions by Optical Coherence Tomography. *Cellulose* **2014**, *21* (3), 1261–1275. https://doi.org/10.1007/s10570-014-0187-5.

(17) Nechyporchuk, O.; Belgacem, M. N.; Pignon, F. Rheological Properties of Micro-/Nanofibrillated Cellulose Suspensions: Wall-Slip and Shear Banding Phenomena. *Carbohydr. Polym.* **2014**, *112*, 432–439. https://doi.org/10.1016/j.carbpol.2014.05.092.

(18) Nazari, B.; Kumar, V.; Bousfield, D. W.; Toivakka, M. Rheology of Cellulose Nanofibers Suspensions: Boundary Driven Flow. *J. Rheol. 1978-Present* **2016**, *60* (6), 1151–1159. https://doi.org/10.1122/1.4960336.

(19) Iotti, M.; Gregersen, Ø. W.; Moe, S.; Lenes, M. Rheological Studies of Microfibrillar Cellulose Water Dispersions. *J. Polym. Environ.* **2010**, *19* (1), 137–145. https://doi.org/10.1007/s10924-010-0248-2.

(20) Martoïa, F.; Dumont, P. J. J.; Orgéas, L.; Belgacem, M. N.; Putaux, J.-L. On the Origins of the Elasticity of Cellulose Nanofiber Nanocomposites and Nanopapers: A Micromechanical Approach. *RSC Adv.* **2016**, *6* (53), 47258–47271. https://doi.org/10.1039/C6RA07176G.

(21) Agoda-Tandjawa, G.; Durand, S.; Berot, S.; Blassel, C.; Gaillard, C.; Garnier, C.; Doublier, J.-L. Rheological Characterization of Microfibrillated Cellulose Suspensions after Freezing. *Carbohydr. Polym.* **2010**, *3* (80), 677–686. https://doi.org/10.1016/j.carbpol.2009.11.045.

(22) Bjorkman. Floc Dynamics in Flowing Fibre Suspensions. *Nord. Pulp Pap. Res. J.* **2005**, *20* (02), 247–252. https://doi.org/10.3183/NPPRJ-2005-20-02-p247-252.

(23) Derakhshandeh, B.; Kerekes, R. J.; Hatzikiriakos, S. G.; Bennington, C. P. J. Rheology of Pulp Fibre Suspensions: A Critical Review. *Chem. Eng. Sci.* **2011**, *66* (15), 3460–3470. https://doi.org/10.1016/j.ces.2011.04.017.

(24) Lasseuguette, E.; Roux, D.; Nishiyama, Y. Rheological Properties of Microfibrillar Suspension of TEMPO-Oxidized Pulp. *Cellulose* **2008**, *15* (3), 425–433. https://doi.org/10.1007/s10570-007-9184-2.

(25) Reiner, R. S.; Rudie, A. W. Experiences with Scaling-Up Production of TEMPO-Grade Cellulose Nanofibrils. In *Nanocelluloses: Their Preparation, Properties, and Applications*; ACS Symposium Series; American Chemical Society, 2017; Vol. 1251, pp 227–245. https://doi.org/10.1021/bk-2017-1251.ch012.

(26) Geng, L.; Naderi, A.; Mao, Y.; Zhan, C.; Sharma, P.; Peng, X.; Hsiao, B. S. Rheological Properties of Jute-Based Cellulose Nanofibers under Different Ionic Conditions. In *Nanocelluloses: Their Preparation, Properties, and Applications*; ACS Symposium Series; American Chemical Society, 2017; Vol. 1251, pp 113–132. https://doi.org/10.1021/bk-2017-1251.ch006.

(27) Saito, T.; Kimura, S.; Nishiyama, Y.; Isogai, A. Cellulose Nanofibers Prepared by TEMPO-Mediated Oxidation of Native Cellulose. *Biomacromolecules* **2007**, *8* (8), 2485–2491. https://doi.org/10.1021/bm0703970.

(28) Okita, Y.; Fujisawa, S.; Saito, T.; Isogai, A. TEMPO-Oxidized Cellulose Nanofibrils Dispersed in Organic Solvents. *Biomacromolecules* **2011**, *12* (2), 518–522. https://doi.org/10.1021/bm101255x.

(29) Fukuzumi, H.; Saito, T.; Iwata, T.; Kumamoto, Y.; Isogai, A. Transparent and High Gas Barrier Films of Cellulose Nanofibers Prepared by TEMPO-Mediated Oxidation. *Biomacromolecules* **2009**, *10* (1), 162–165. https://doi.org/10.1021/bm801065u.

(30) Iwamoto, S.; Lee, S.-H.; Endo, T. Relationship between Aspect Ratio and Suspension Viscosity of Wood Cellulose Nanofibers. *Polym. J.* **2014**, *46* (1), 73–76. https://doi.org/10.1038/pj.2013.64.

(31) Tao, Y.-G.; den Otter, W. K.; Padding, J. T.; Dhont, J. K. G.; Briels, W. J. Brownian Dynamics Simulations of the Self- and Collective Rotational Diffusion Coefficients of Rigid Long Thin Rods. *J. Chem. Phys.* **2005**, *122* (24), 244903. https://doi.org/10.1063/1.1940031.

(32) Nechyporchuk, O.; Belgacem, M. N.; Pignon, F. Current Progress in Rheology of Cellulose Nanofibril Suspensions. *Biomacromolecules* **2016**, *17* (7), 2311–2320. https://doi.org/10.1021/acs.biomac.6b00668.

(33) Burns, N. A.; Naclerio, M. A.; Khan, S. A.; Shojaei, A.; Raghavan, S. R. Nanodiamond Gels in Nonpolar Media: Colloidal and Rheological Properties. *J. Rheol.* **2014**, *58* (5), 1599–1614.

(34) Raghavan, S. R.; Khan, S. A. Shear-induced Microstructural Changes in Flocculated Suspensions of Fumed Silica. *J. Rheol.* **1995**, *39* (6), 1311–1325. https://doi.org/10.1122/1.550638.

(35) Walls, H. J.; Caines, S. B.; Sanchez, A. M.; Khan, S. A. Yield Stress and Wall Slip Phenomena in Colloidal Silica Gels. *J. Rheol.* **2003**, *47* (4), 847–868. https://doi.org/10.1122/1.1574023.

(36) Hill, R. J. Elastic Modulus of Microfibrillar Cellulose Gels. *Biomacromolecules* **2008**, *9* (10), 2963–2966. https://doi.org/10.1021/bm800490x.

(37) Azzam, F.; Siqueira, E.; Fort, S.; Hassaini, R.; Pignon, F.; Travelet, C.; Putaux, J.-L.; Jean, B. Tunable Aggregation and Gelation of Thermoresponsive Suspensions of Polymer-Grafted Cellulose Nanocrystals. *Biomacromolecules* **2016**, *17* (6), 2112–2119. https://doi.org/10.1021/acs.biomac.6b00344.

(38) Hyun, K.; Wilhelm, M.; Klein, C. O.; Cho, K. S.; Nam, J. G.; Ahn, K. H.; Lee, S. J.; Ewoldt, R. H.; McKinley, G. H. A Review of Nonlinear Oscillatory Shear Tests: Analysis and Application of Large Amplitude Oscillatory Shear (LAOS). *Prog. Polym. Sci.* **2011**, *36* (12), 1697–1753. https://doi.org/10.1016/j.progpolymsci.2011.02.002.

(39) Hyun, K.; Kim, S. H.; Ahn, K. H.; Lee, S. J. Large Amplitude Oscillatory Shear as a Way to Classify the Complex Fluids. *J. Non-Newton. Fluid Mech.* **2002**, *107* (1), 51–65. https://doi.org/10.1016/S0377-0257(02)00141-6.

(40) Mason, T. G.; Bibette, J.; Weitz, D. A. Elasticity of Compressed Emulsions. *Phys. Rev. Lett.* **1995**, *75* (10), 2051–2054. https://doi.org/10.1103/PhysRevLett.75.2051.

(41) Arya, G.; Panagiotopoulos, A. Z. Log-Rolling Micelles in Sheared Amphiphilic Thin Films. *Phys. Rev. Lett.* **2005**, *95* (18). https://doi.org/10.1103/PhysRevLett.95.188301.

(42) Moghimi, E.; Jacob, A. R.; Koumakis, N.; Petekidis, G. Colloidal Gels Tuned by Oscillatory Shear. *Soft Matter* **2017**, *13* (12), 2371–2383. https://doi.org/10.1039/C6SM02508K.

(43) Martoïa, F.; Dumont, P. J. J.; Orgéas, L.; Belgacem, M. N.; Putaux, J.-L. Micro-Mechanics of Electrostatically Stabilized Suspensions of Cellulose Nanofibrils under Steady State Shear Flow. *Soft Matter* **2016**, *12* (6), 1721–1735. https://doi.org/10.1039/C5SM02310F.

(44) Yang, M. C.; Scriven, L. E.; Macosko, C. W. W. *J. Rheol.* **1986**, *30* (5), 1015–1029. https://doi.org/10.1122/1.549892.

(45) Puisto, A.; Illa, X.; Mohtaschemi, M.; Alava, M. Modeling the Rheology of Nanocellulose Suspensions. *Nord. Pulp Pap. Res. J.* **2012**, *27* (2), 277–281. https://doi.org/10.3183/NPPRJ-2012-27-02-p277-281.

(46) Cheng, D. C.-H. Yield Stress: A Time-Dependent Property and How to Measure It. *Rheol. Acta* **1986**, *25* (5), 542–554. https://doi.org/10.1007/BF01774406.

(47) Fall, A.; Bertrand, F.; Ovarlez, G.; Bonn, D. Yield Stress and Shear Banding in Granular Suspensions. *Phys. Rev. Lett.* **2009**, *103* (17), 178301. https://doi.org/10.1103/PhysRevLett.103.178301.

(48) Derakhshandeh, B.; Petekidis, G.; Shafiei Sabet, S.; Hamad, W. Y.; Hatzikiriakos, S. G. Ageing, Yielding, and Rheology of Nanocrystalline Cellulose Suspensions. *J. Rheol.* **2012**, *57* (1), 131–148. https://doi.org/10.1122/1.4764080.

(49) Petekidis, G.; Moussaïd, A.; Pusey, P. N. Rearrangements in Hard-Sphere Glasses under Oscillatory Shear Strain. *Phys. Rev. E* **2002**, *66* (5), 051402. https://doi.org/10.1103/PhysRevE.66.051402.

(50) Koumakis, N.; Petekidis, G. Two Step Yielding in Attractive Colloids: Transition from Gels to Attractive Glasses. *Soft Matter* **2011**, *7* (6), 2456. https://doi.org/10.1039/c0sm00957a.

(51) Ilzhoefer, J. R.; Broom, B. C.; Nepa, S. M.; Vogler, E. A.; Khan, S. A.; Spontak, R. J. Evidence of Hierarchical Order in an Amphiphilic Graft Terpolymer Gel. *J. Phys. Chem.* **1995**, *99* (32), 12069–12071. https://doi.org/10.1021/j100032a002.

CHAPTER 3

Quantitative Calorimetric Studies of the Chiral Nematic Mesophase in Aqueous Cellulose Nanocrystal Suspensions

3.1 ABSTRACT. Aqueous suspensions of cellulose nanocrystals (CNC) can spontaneously form a chiral nematic mesophase at a critical concentration (c^*). Unfortunately, no current analytical technique permits rapid detection of c^*. Herein, we introduce a facile and accurate approach to assess c^* rapidly (< 2 h) from a small sample volume and compare our results to those obtained by conventional methods. Our strategy employs isothermal titration calorimetry (ITC) to measure the heat of interaction, which can identify the onset of mesophase formation since it is sensitive to suspension viscosity and thus capable of detecting small changes in the suspension environment. We measure c^* for CNC samples differing in surface charge and aspect ratio and find that lower aspect ratios and higher surface charges both increase c^*. Our ITC results reveal the role of CNC interactions prior to visual observation of mesophase formation and elucidate effects related to nanocrystals and their suspensions.

3.2 INTRODUCTION

Cellulose nanocrystals (CNCs) have become a popular research topic as a broadly promising biomaterial. They continue to attract increasing attention due largely to their interesting aqueous suspension behavior, as well as their renewability, biodegradability and promising properties.[1] Their potential uses span a wide and diverse range of applications, including reinforcement media for polymer nanocomposites,[2] biomimetic materials and optically-active coatings.[3] One common method of preparing CNCs involves the hydrolysis of cellulose sources in sulfuric acid.[4,5] This treatment dissolves the less ordered regions of native cellulose fiber, leaving behind rigid, crystalline nanoparticles with a high aspect ratio. It simultaneously converts a fraction of the hydroxyl moieties on the surface of the nanocrystals to negatively charged sulfate half-ester groups, resulting in improved colloidal stability in aqueous suspensions due to electrostatic repulsion by the sulfate groups. In many cases, acidic ester are ion exchanged with sodium to facilitate redispersion after drying the nanocrystals.[6] Of the many interesting properties of CNC aqueous suspensions, their propensity to form a chiral nematic mesophase is among the most avidly studied.[7–13] Previous investigations of this mesomorphic behavior have been illuminating, and it is generally accepted that formation of a chiral nematic mesophase is driven by the rod-like shape and inherent chirality of CNC.[1] A critical concentration (c^*) can be defined, above which the CNCs phase-separate into anisotropic (bottom) and isotropic (upper) fractions. The value of c^* depends primarily on the aspect ratio[8,14] and surface charge of the CNCs.[15,16] Higher aspect ratios favor ordering and shift c^* to lower concentrations, in agreement with the theory of Onsager.[17] Conversely, increasing surface charge shifts c^* to higher concentrations in suspensions of protonated CNCs. In this case, the increased total ionic strength of the suspension screens repulsive charges, resulting in a reduction in the effective volume fraction, so that a higher crystal concentration is required for the suppressed electrostatic double layers (EDLs) to overlap.[15] High CNC volume fractions can alternatively induce volume-arrested states, *i.e.*, gelation or colloidal glass formation,[18] which can disrupt or compete with cholesteric mesophase formation.[19]

The complexity between rheological and mesomorphic behavior has naturally motivated numerous studies that provide a strong foundation for further investigation into the liquid crystalline ordering of CNCs. A seminal study has been conducted by Reid *et al.*,[20] who systematically compared the properties of different commercially available and lab-produced CNCs. Detailed studies have elucidated the roles of ionic strength,[10,21–23] aspect ratio[24] and surface charge[13,15,25,26] on mesophase formation, and phase diagrams describing CNC ordering and kinetic arrest at varied ionic strength conditions have been reported by Honorato-Rios *et al.*[27] The rheological behavior of aqueous CNC suspensions has been the subject of numerous related investigations,[23,28–37] and viscosity has frequently been used as an indicator of CNC ordering on the presumption that pre-aligned chiral nematic domains exhibit more pronounced shear-thinning behavior than a fully isotropic suspension of rods.[38] This can, however, be an exquisitely delicate measurement because of the interrelationship between shear and alignment. While shear can detect ordering, it can also either induce or disrupt ordering depending on how it is applied. In addition, measuring the viscosity of very dilute suspensions at low shear rates can be experimentally challenging.[38] Hence, using viscosity as a means to identify CNC ordering has limitations.

Conventionally, c^* is routinely determined by polarized optical microscopy[32,39] by checking for the presence of birefringent domains in suspensions between crossed polarizers. Another, somewhat imprecise method that is perhaps the most commonly used in practice is direct visualization of phase separation. For example, an aqueous CNC suspension left to stand for an extended time under quiescent conditions will phase-separate if the concentration is above c^*, and the presence of anisotropic domains can be observed visually once they exceed the wavelength of visible light, which may take days to weeks.[14] These protocols are valuable to check whether a given suspension is above or below c^*, but they are impractical to determine the value of c^* with precision. In addition to being laborious, they can also be inconvenient if sample quantity is limited. To the best of our knowledge, no method is currently available to test a single suspension and determine c^* directly. In the present work, we propose a calorimetric method to discern c^* of suspensions differing in CNC aspect ratios and surface charges. By automatically and continuously diluting an initially concentrated suspension (above c^*), we can quickly and accurately determine the value of c^* by measuring the heat flux of the sample by isothermal titration calorimetry (ITC). We demonstrate here that, by injecting a concentrated suspension with small volumes of water at short time intervals, the response can be measured over a wide range of concentrations at high resolution. Changes in viscosity (which are previously shown to relate to liquid crystalline behavior)[33,38,40] throughout the experiment can be interpreted to provide an accurate estimation of c^* for various samples with different properties that impact their liquid crystalline behavior. Since c^* constitutes such an important fundamental property of CNC suspensions, an expedient method by which to ascertain it can afford a highly beneficial advantage.

3.3 EXPERIMENTAL

3.3.1 Materials

Cellulose nanocrystals were purchased from Forest Products Laboratories, FPL (Madison, WI), where they were prepared by sulfuric acid hydrolysis and distributed in sodium form as a 12 wt% aqueous suspension. Samples were tested as-received and after being subjected to several different treatments, including (*i*) size fractionation as described elsewhere[14] to separate higher (anisotropic fraction) and lower (isotropic fraction) aspect ratios and (*ii*) acid-catalyzed desulfation as proposed by Jiang *et al*.[26] to reduce surface charge by removing some of the sulfate groups. Additional CNC grades provided by collaborators from University of British Columbia (UBC) and Hebrew University of Jerusalem (HUJI) were used as-received, and a summary of the materials examined in this study is provided in **Table 3.1**.

Table 3.1. Summary of CNCs used in this study and their key properties.

CNC designation	Source	Expected c^* (wt%)	Surface charge (μmol OSO_3/g CNC)	Zeta potential (mV)	Length (nm)	Width (nm)	Aspect ratio
FPL-CNC	FPL	4	330	-46	120 ± 38	5.6 ± 0.5	21
D-CNC	FPL (modified)	3	-	-37	148 ± 41	5.3 ± 0.6	28
S-CNC	FPL (modified)	6	-	-40	108 ± 32	6.3 ± 0.4	17
LD-CNC	FPL (modified)	3	-	-44	150 ± 42	5.5 ± 0.4	27
175-CNC	HUJI	0.7	157	-38	94 ± 7	4.5 ± 0.2	21
875-CNC	HUJI	0.5	87	-36	101 ± 6	5.7 ± 0.2	18
UBC-CNC	UBC	7	235	-33	127 ± 49	7.0 ± 2	18

3.3.2 Methods

Acid-catalyzed desulfation was conducted according to the procedure described elsewhere.[26] Here, 500 mL of suspension containing 1 wt% CNC was heated to 80 °C, at which point HCl was added to achieve a final acid concentration of 12.5 mM and the suspension subsequently stirred for 2 h. The reaction was then quenched in an ice bath, followed by dialysis against DI water (until a stable pH was achieved) to remove free sulfate groups and ultrafiltration in a stirred cell to increase the suspension concentration to ~6 wt% (as previously recommended[39]). Aspect-ratio fractionation was performed using a previously established method.[14] A 7 wt% aqueous CNC suspension was allowed to equilibrate for 1 week, resulting in nearly even separation into isotropic and anisotropic phases. The top fraction (isotropic) was removed by pipetting, and each of the separated phases was then fractionated two additional times, for a total of 3 iterations. The thrice-anisotropic fraction has a statistically higher aspect ratio, and the thrice-isotropic has a reduced aspect ratio. Dilution (by addition of DI water) of anisotropic fractions and concentration (by ambient evaporation) of isotropic fractions between iterations was necessary to achieve an approximately even split, since the anisotropic fraction was inherently more concentrated. Atomic force microscopy (AFM) images of the resultant suspensions were acquired on an Asylum MFP-

3D instrument. In the case of each sample, a 0.01 wt% CNC suspension was dropped onto freshly cleaved mica that had been treated for 30 min with a 0.01 wt% poly-L-lysine solution. This was allowed to sit for 1 min, rinsed with DI water and blown dry with nitrogen gas. Particle dimensions were then determined by ImageJ,[41] with 140-300 individual particles measured from 4-7 images per sample. Zeta potentials were measured from a 0.01 wt% CNC suspension with 10 mM NaCl by a Malvern ZetaSizer (NanoZSP). Surface charges were discerned by conductometric titration.[39] A low-volume TA Instruments NanoITC was used for the ITC experiments. In this procedure, the sample cell was filled with concentrated aqueous CNC suspension (initially above c^*), whereas the reference cell contained deionized (DI) water. The titration syringe was also loaded with DI water and injections were performed in 1.0-2.5 μL increments, with 250-600 s between each dilution. Changing injection volume or equilibration time did not noticeably influence the results, since the relationship between viscosity and concentration is not impacted by either factor (as demonstrated for the case of variable injection concentrations in **Figure B.1**). Stirring was maintained at 350 rpm throughout each test run by the rotating titration syringe. The heating power required to maintain isothermal conditions was monitored continuously and integrated over the time interval of the injections to yield the change in enthalpy associated with each injection.

3.4.1 Heat rate considerations

To validate the calorimetry method introduced here, we first evaluate the result for a sample with a known c^* value. Commercially available CNCs from Forest Products Laboratories (FPL) have been previously reported[14,42,43] to exhibit phase separation at 4-5 wt% with some degree of batch-to-batch variability. The sample employed in this study forms a cholesteric mesophase at 4 wt% when left standing quiescently in a vial (**Figure B.2**). Since no evidence of birefringence is observed at 3 wt% CNC, we infer that the value of c^* lies between 3 and 4 wt%. The time required for this suspension to exhibit visible phase separation is more than two weeks, which is substantially longer than the time needed to induce phase separation in suspensions with higher concentrations of 5 or 6 wt% (~ 3 days). The longer equilibration time, coupled with the observation that the volume fraction of the anisotropic phase (φ) is relatively small at 4 wt% (φ ≈ 0.06), suggests that c^* is likely only slightly below that suspension concentration. In **Figure 3.1a**, φ is presented as a function of suspension concentration and confirms that φ is strongly dependent on CNC content, as expected, and that a suspension with 8 wt% CNC is well above c^*. Starting with this concentration, we have performed an incremental suspension dilution while monitoring the heat flow required to maintain isothermal conditions. To simplify data presentation, we have removed the injection peaks (which were uniform throughout the experiment and representative of the heat of dilution) and plotted only the equilibrium baseline values associated with the end of each injection in **Figure 3.1b.** A representative excerpt of the full raw data is included in **Figure B.3**. The baseline heat rate of an ITC experiment provides a measure of the viscosity of the sample,[44,45] since the stirring action of the syringe produces more pronounced viscous heating effects for a higher viscosity sample.[46,47] As a consequence, less power is required from the heater to maintain the target temperature, as depicted in **Figure 3.2a**.

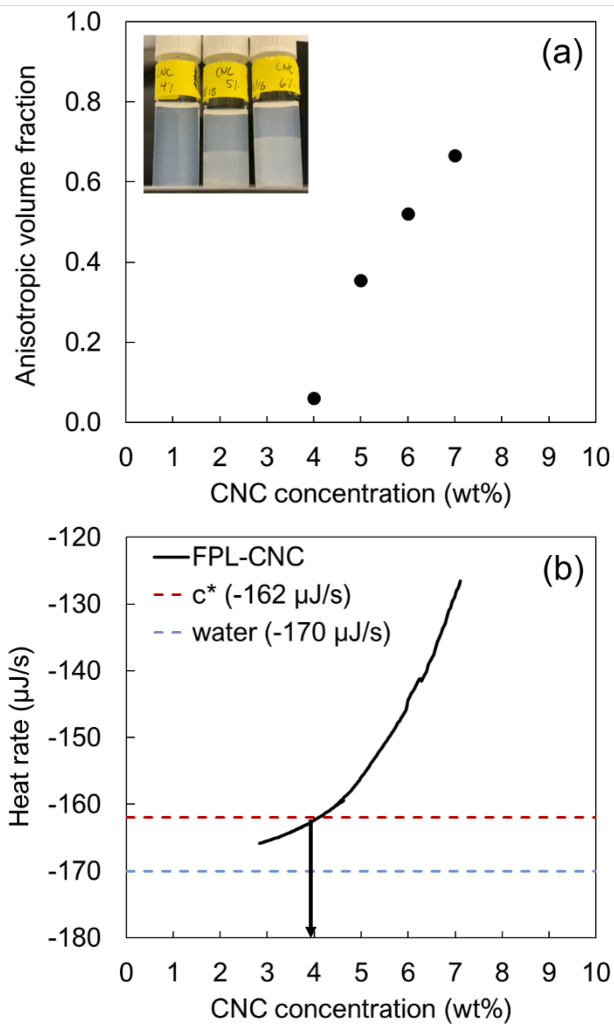

Figure 3.1. (a) Measured volume fraction of the anisotropic phase (φ) as discerned from phase-separated FPL-CNC suspensions in vials (inset showing representative CNC concentrations of 4, 5 and 6 wt.%) as a function of CNC concentration. (b) Dependence of heat rate on CNC concentration during dilution for as-received FPL-CNCs. Indicated here is the baseline for a stirring cell containing only water (blue dashed line) and the baseline at which c^* of FPL-CNC suspensions is crossed at ~4 wt% (red dashed line and arrow).

As the dilution proceeds to lower concentrations and therefore lower viscosities, the heat rate decreases accordingly. Furthermore, the baseline appears to level off at low CNC concentrations, approaching a horizontal asymptote at about -168 μJ/s, which is the baseline heat rate of a cell containing only water for the relevant experimental parameters (25°C and 350 rpm). The results evident in **Figure 3.1b** illustrate a key concept: *the difference in baseline heat rates is associated with viscous heating and, hence, the suspension viscosity.* In other words, decreasing the CNC concentration promotes a reduction in viscosity, which is reflected in the ITC signal due to the reduced viscous heating effects, as diagrammed in **Figure 3.2a**. This concept is further verified by measuring the baseline heat rate for the sample cell across a range of stir rates. As expected, increasing the stir rate from 150 to 450 rpm elevates viscous heat and lowers (less exothermic) power output from the heater to maintain isothermal conditions (**Figure 3.2b**).

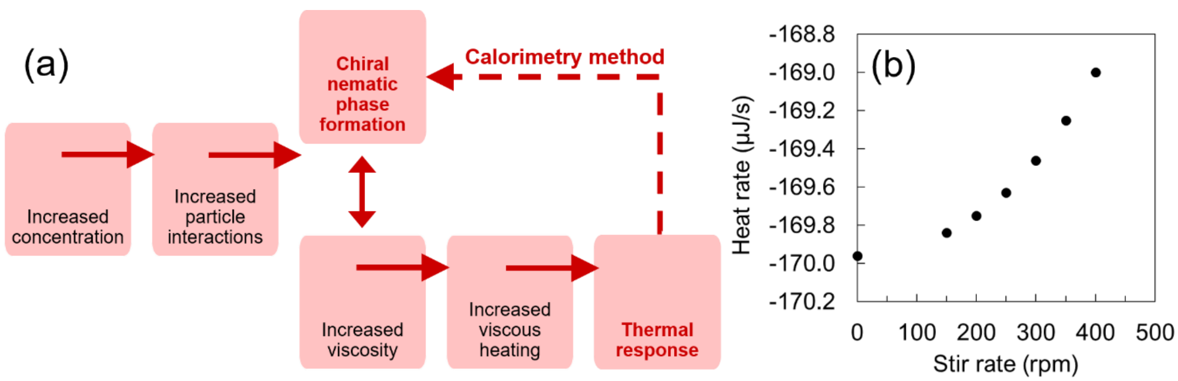

Figure 3.2. (a) Schematic diagram describing the underlying principle behind the use of ITC to determine c^*. Viscosity links liquid crystalline ordering and the thermal response detected by ITC. Increasing the CNC concentration provokes a response in both mesomorphic behavior and rheology, the latter of which can be detected by ITC due to viscous heating (i.e., stirring a more viscous material generates more friction and consequently more heat than the same stir rate applied to a less viscous material). (b) Baseline heat rate measured by ITC for water only at different stir rates. The measured heat rate indicates the power supplied by the heater to maintain isothermal conditions (25°C), which decreases (becomes less exothermic) as the stir rate is increased. An increase in viscous heating lowers the demand on the heater.

Previous work has established that the viscosity of a CNC suspension is related to its liquid crystallinity.[27,31,33,40,43] Xu *et al.*[43] have observed that isotropic CNC suspensions (< 3 wt%) exhibit Newtonian behavior, while suspensions that are initially biphasic or liquid crystalline are shear-thinning. Haywood *et al.*[40] point out that biphasic suspensions often display a characteristic 3-region viscosity profile, and Van Rie *et al*.[38] have found that samples at CNC concentrations above c^* exhibit an apparent viscosity that has a more negative slope with respect to shear rate compared to samples to isotropic suspensions. This leads us to a second key concept: *the onset of liquid crystallinity can be detected by ITC due to the flow behavior of CNC suspensions.* We will make use of this relationship to determine c^* precisely and expediently. Taken together, these two key concepts indicate that the ITC heat signal can be used to determine the concentration corresponding to the onset of mesophase formation by straightforward dilution. Starting with our benchmark sample of FPL CNC, we use this result from ITC to calibrate our further measurements, in which case the heat rate of -162 μJ/s in **Figure 3.1b** is selected as the critical value identifying the transition from isotropic to biphasic suspension. We hypothesize that CNCs with different properties cross through this critical heat rate at their respective c^* thresholds on the premise that c^* is associated with a "critical viscosity" that can be identified via viscous heating effects detected by ITC.

3.4.2 Aspect ratio effect

According to the theory proposed by Onsager[17] for rigid rods in suspension, rods possessing a shorter aspect ratio will exhibit a higher value of c^*, which has been verified[14] for size-fractionated CNCs intended to separate the nanocrystals on the basis of their length. Using the same protocol, we compare as-received CNCs with a suspension containing CNCs with a lower aspect ratio (S-CNC) to ascertain whether ITC correctly tracks the change in c^*. After fractionation, the average length of the crystals determined by AFM is reduced from 120 ± 38 nm to 108 ± 32 nm (*cf.* **Figure B.4**). Measured values of φ from visual observation (**Figure B.5**) are provided as a function of CNC concentration in **Figure 3.3a** and confirm that c^* is higher (between 5 and 6 wt% S-CNC) than for the unfractionated parent FPL-CNCs. The corresponding ITC results for S-CNC suspensions are included in **Figure 3.3b** and reveal that the concentration evaluated at -162 μJ/s (for c^* of FPL-CNC in **Figure 3.1b**) is ~ 5.6 wt% for the shorter CNCs, in favorable agreement with both the amorphous fraction data in **Figure 3.3a** and theoretical expectations.

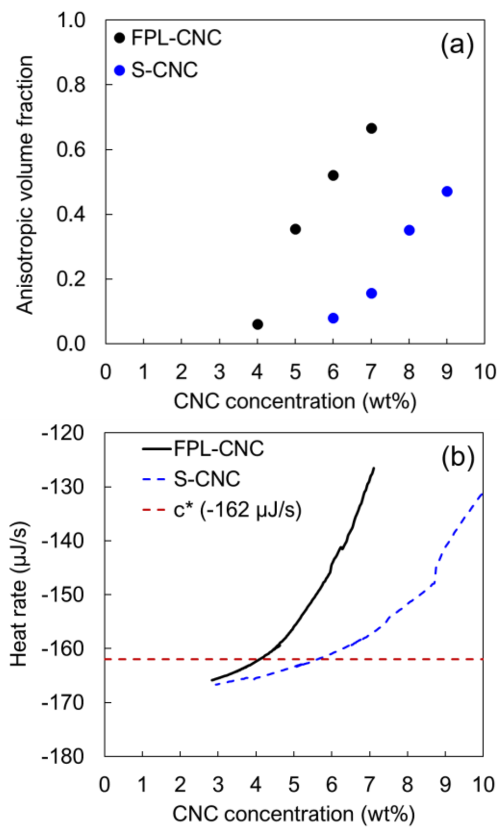

Figure 3.3. (a) Measured values of φ as discerned from phase-separated FPL-CNC and S-CNC suspensions (see legend) as a function of CNC concentration, indicating that c^* for S-CNC suspensions lies between 5 and 6 wt%. (b) Dependence of heat rate on CNC concentration during ITC for FPL-CNC and S-CNC suspensions (see legend). The heat rate corresponding to -162 μJ/s (red dashed line) is used to identify c^* (≈ 5.6 wt%) for the S-CNC suspension.

3.4.3 Surface charge effect

Abitbol *et al.*,[15] as well as others, have demonstrated that a reduction in surface charge lowers c^*. To discern whether ITC can predict this behavior, we have chemically modified the as-received FPL-CNCs by using a well-established desulfation protocol to partially remove surface charges. Based on visual observation of phase separation (**Figure B.6**) and the corresponding anisotropic volume fraction measurements for the desulfated CNC (D-CNC) presented in **Figure 3.4a**, we expect c^* to fall between 2 and 3 wt%, especially since $\varphi = 0.12$ at 3 wt% D-CNC. This result confirms that a reduction in surface charge lowers c^*. In **Figure 3.4b**, the heat rate for the desulfated CNCs (D-CNC) crosses the selected c^* threshold (at -162 μJ/s) at a concentration of ~ 2.7 wt%, which favorably agrees with visual observations. Also included in **Figure 3.4** for additional comparison are corresponding findings from aqueous suspensions composed of a fractionated and desulfated CNC (LD-CNC) with longer nanocrystals and a larger aspect ratio (see **Table 3.1**). The value of c^* in this system is estimated as < 3 wt% from phase-separation observations (**Figure B.7**) in **Figure 3.4a** and measured as ~ 2.1 wt% from ITC results in **Figure 3.4b**. The observation that c^* in this case is lower than that of the D-CNC suspensions further corroborates the expected relationship between aspect ratio and c^*. At 3 wt% nanocrystal concentration, for instance, $\varphi = 0.12$ for the D-CNC suspensions, whereas $\varphi = 0.58$ for the LD-

CNC suspensions (**Figure 3.4a**), clearly indicating that the latter possesses a lower critical concentration.

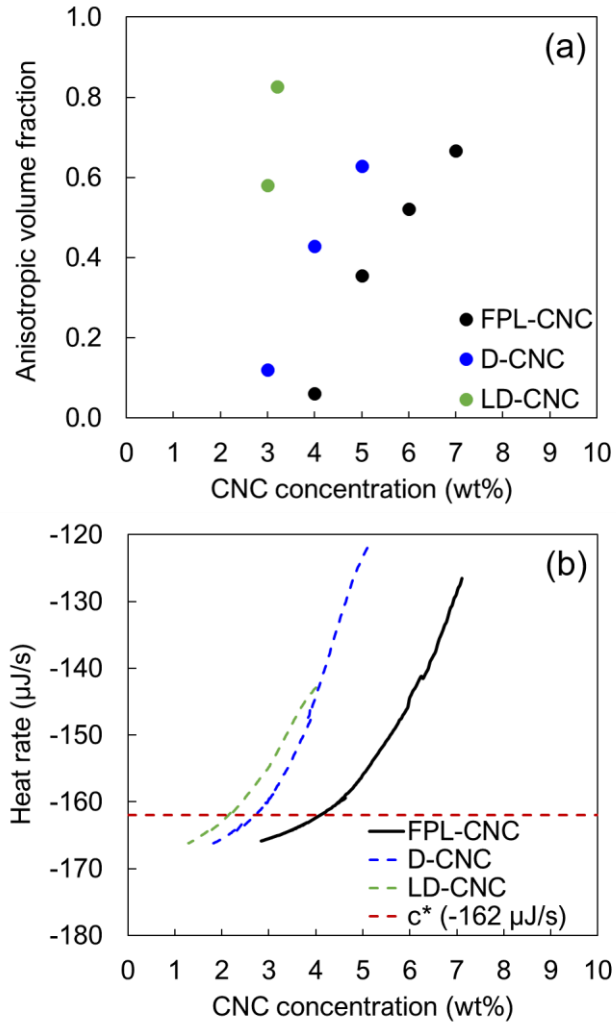

Figure 3.4. (a) Measured values of φ as discerned from phase-separated FPL-CNC, D-CNC and LD-CNC suspensions (see legend) as a function of CNC concentration, indicating that c^* for both D-CNC and LD-CNC suspensions lies between 2 and 3 wt%. (b) Dependence of heat rate on CNC concentration during ITC for FPL-CNC, D-CNC and LD-CNC suspensions (see legend). The heat rate corresponding to -162 μJ/s (red dashed line) is used to identify c^* for each suspension (see the text for values).

3.4.4 Generalized analysis validity

To establish the general validity of the ITC method as a precise analytical technique, we have obtained CNC samples with different properties from other sources. Two that were characterized in an earlier study[15] (designated here as 175-CNC and 875-CNC) have been kindly provided by the authors of that work. Their respective c^* values are 0.50 and 0.65 wt%, as determined in that study by visual observation of phase separation. Measurement of these suspensions by ITC in **Figure 3.5** indicate c^* transitions at 0.87 and 0.84 wt%, respectively. Although these values of c^* are qualitatively comparable to those acquired previously visual observation of phase separation, the discrepancy between previous and present values of c^* might indicate some unidentified error in the measurement protocol. It is also possible, however, that the condition of the as-received samples altered their mesomorphic behavior. More precisely, the samples have been stored for 2 years, in which case they might have aggregated or denatured (in terms of surface charge). Factors such as these would not be unexpected and could strongly influence the onset of mesophase formation. While the sample quantity was insufficient to assess c^* by complementary methods, duplicate ITC trials ensure good reproducibility of the results reported here. A third sample, prepared at the University of British Columbia (UBC-CNC), possesses a c^* value of ~ 7 wt% from visual observation of phase separation in the presence of 1 mM NaCl (**Figure B.8**). Since ionic strength strongly affects the viscosity of colloidal suspensions, we have performed ITC with and without added electrolyte. At 1 mM NaCl, the viscosity of the suspension is suppressed, along with the baseline heat rate, resulting in an overestimation of c^* (~ 9 wt%). This observation emphasizes the importance of viscosity as a factor in the baseline heat rate for ITC experiments, and illustrates that the empirical threshold identified in this work is not universal. Without the addition of electrolyte, however, c^* is measured to be ~ 5.3 wt%. Although this value is lower than the anticipated value of 7 wt%, it is reasonable based on previous efforts that indicate the addition of 1 mM NaCl should increase c^* by ≈ 1 wt% due to a reduction in effective volume fraction as an increase in ionic strength suppresses the electrostatic double layer of the nanocrystals. For example, Honorato-Rios *et al.*[27] have recorded c^* between 3 and 4 wt% for an electrolyte-free CNC suspension. Incorporation of 1 mM NaCl raises c^* to between 4 and 5 wt%. Similarly, Dong *et al.*[10] have found that c^* shifts from 5.7 to 7.4 wt% upon increasing the ionic strength of a CNC suspension from 0.1 to 1 mM. Considering this precedent, we believe that the value of c^* measured here from the electrolyte-free suspension is acceptable given the higher c^* at 1 mM NaCl.

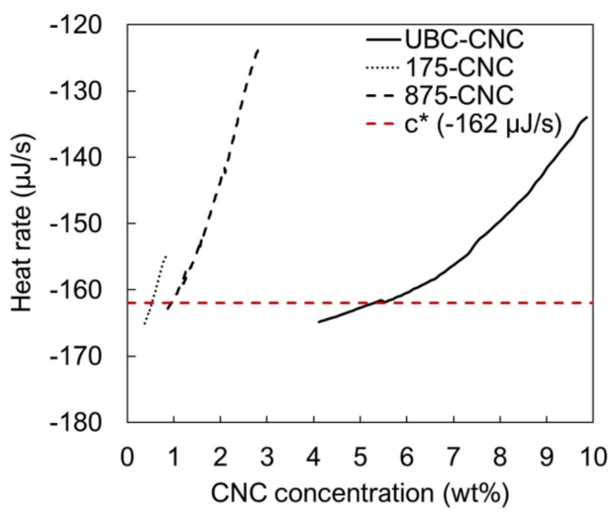

Figure 3.5. Dependence of heat rate on CNC concentration during ITC for three additional CNC suspensions (see legend). The heat rate corresponding to -162 μJ/s (red dashed line) is used to identify c^* for each suspension (see the text for values).

3.5 DISCUSSION

To help assess the merit of ITC as a quantitative analytical method to determine c^* expediently, **Figure 3.6** displays values of c^* measured by this technique against values visually observed by phase separation or provided by the sample source. Because phase-separation observations are only assessed in intervals of ~ 1 wt%, a slight underestimation in c^* is expected by ITC since the resolution is higher (~ 0.1 wt%). For example, in the case of FPL-CNC suspensions, phase separation is visually detected at 4 wt%, which indicates that c^* must be *less than* 4 wt%. Indeed, the precision of ITC is one of its great advantages, but this aspect is difficult to evaluate at present given the lack of comparable detail afforded by other experimental methods. For other strategies developed to assess c^*, the precision of the measurement is frequently limited by the concentration interval selected. Furthermore, the accurate preparation of suspensions of known concentration can be challenging due to the discrepancies in composition between the isotropic and anisotropic phases. Utilization of ITC effectively eliminates the need for painstaking preparation of a series of suspensions precisely differing in CNC concentration. Data reproducibility in ITC has also proven to be very consistent; for instance, a series of 4 repeated measurements starting with the same suspension concentration of as-received FPL-CNC yields a standard deviation of less than 0.1 wt%. In addition to excellent experimental reproducibility, ITC offers several other practical advantages. First, it requires relatively small sample volumes (as little as 300 μL for a single trial) if the sample concentration is above c^*. This can easily be achieved by water evaporation or by stirred-cell ultrafiltration[14] if the initial sample does not meet this requirement. Moreover, equilibration is not required as it is in the case of phase-separation observations. Use of phase separation to identify mesomorphic behavior necessitates quiescent equilibration for long times ranging from *ca*. 24 h up to 4 months.[14] In marked contrast, an entire ITC experiment lasts only a few hours. A quantitative comparison of the improved efficiency of ITC relative to conventional approaches is included in the **Appendix B**, in which we estimate that sample quantity can be reduced by a factor of ~40x and time by a factor ~60x of by the use of this method.

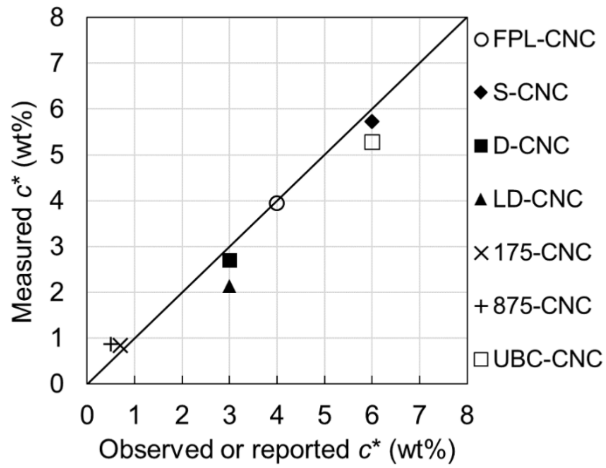

Figure 3.6. Values of c^* measured here by ITC (ordinate) with respect to corresponding c^* values observed by phase separation or provided by the source (abscissa). The solid line represents where they are equal for reference. The symbols are identified (see legend) and represent various CNC samples described in the text.

3.6 CONCLUSIONS

In this study, we have presented a method by which the critical concentration corresponding to the onset of CNC mesomorphic behavior can be rapidly and efficiently measured by ITC. The method is based on two key underlying principles: (*i*) the viscosity of a suspension influences the heat generated by stirring, and (*ii*) liquid crystallinity in a CNC suspension can be detected from changes in viscosity. This technique is successful at accurately estimating c^* for 7 CNC grades from different sources and possessing different properties. The relationship between liquid crystalline ordering, suspension viscosity and viscous heating is complex, since nanocrystal considerations (*e.g.*, surface charge, aspect ratio, polydispersity, and surface chemistry) and the suspension environment (*e.g.*, ionic strength, temperature, pH, and dispersability[20]) all influence both viscosity and mesomorphic behavior, but not necessarily to the same degree. Despite the analytical challenges this relationship presents, it also means that both properties constitute sensitive indicators of relevant experimental parameters, making them powerful tools for characterization and quality control. This technique has the potential to elucidate fundamental structure/property relationships for CNC, as well as for other liquid crystalline systems. The advantages of the method include short measurement time, small sample volume and improved experimental resolution, but additional study of the nuanced relationship between viscosity and c^* would augment its general applicability. A more rigorous and detailed exploration of the sensitive interplay between nanocrystal characteristics, suspension properties, viscosity, and liquid crystalline behavior is clearly warranted. Such analysis has the potential to extend the application of this method to a plethora of other phase-separating systems and facilitate detailed characterization even in the absence of previously established standards.

3.7 ACKNOWLEDGMENTS

The authors would like to acknowledge Tiffany Abitbol, Emily Cranston, and Gwendoline Delepierre for sharing their samples and for discussions regarding the experimental work. This work was performed in part at the Analytical Instrumentation Facility (AIF) at North Carolina State University, which is supported by the State of North Carolina and the National Science Foundation (award number ECCS-1542015). The AIF is a member of the North Carolina Research Triangle Nanotechnology Network (RTNN), a site in the National Nanotechnology Coordinated Infrastructure (NNCI). O.J.R. acknowledges funding from the European Research Council (ERC) under the European Union’s Horizon 2020 research and innovation program (ERC Advanced Grant Agreement No. 788489, “BioElCell”) and the Canada Excellence Research Chair initiative and the Canada Foundation for Innovation (CFI).

3.8 REFERENCES

(1) Habibi, Y.; Lucia, L. A.; Rojas, O. J. Cellulose Nanocrystals: Chemistry, Self-Assembly, and Applications. *Chemical Reviews* **2010**, *110* (6), 3479–3500. https://doi.org/10.1021/cr900339w.

(2) Zhou, C.; Wu, Q. Recent Development in Applications of Cellulose Nanocrystals for Advanced Polymer-Based Nanocomposites by Novel Fabrication Strategies. **2012**. https://doi.org/10.5772/48727.

(3) Kontturi, E.; Laaksonen, P.; Linder, M. B.; Nonappa; Groechel, A. H.; Rojas, O. J.; Ikkala, O. Advanced Materials through Assembly of Nanocelluloses. *Adv. Mater.* **2018**, *30* (24), 1703779. https://doi.org/10.1002/adma.201703779.

(4) Mao, J.; Abushammala, H.; Brown, N.; Laborie, M.-P. Comparative Assessment of Methods for Producing Cellulose I Nanocrystals from Cellulosic Sources. In *Nanocelluloses: Their Preparation, Properties, and Applications*; ACS Symposium Series; American Chemical Society, 2017; Vol. 1251, pp 19–53. https://doi.org/10.1021/bk-2017-1251.ch002.

(5) Korolovych, V. F.; Cherpak, V.; Nepal, D.; Ng, A.; Shaikh, N. R.; Grant, A.; Xiong, R.; Bunning, T. J.; Tsukruk, V. V. Cellulose Nanocrystals with Different Morphologies and Chiral Properties. *Polymer* **2018**, *145*, 334–347. https://doi.org/10.1016/j.polymer.2018.04.064.

(6) Beck, S.; Bouchard, J.; Berry, R. Dispersibility in Water of Dried Nanocrystalline Cellulose. *Biomacromolecules* **2012**, *13* (5), 1486–1494. https://doi.org/10.1021/bm300191k.

(7) Tran, A.; Hamad, W. Y.; MacLachlan, M. J. Tactoid Annealing Improves Order in Self-Assembled Cellulose Nanocrystal Films with Chiral Nematic Structures. *Langmuir* **2018**, *34* (2), 646–652. https://doi.org/10.1021/acs.langmuir.7b03920.

(8) Hu, Y.; Abidi, N. Distinct Chiral Nematic Self-Assembling Behavior Caused by Different Size-Unified Cellulose Nanocrystals via a Multistage Separation. *Langmuir* **2016**, *32* (38), 9863–9872. https://doi.org/10.1021/acs.langmuir.6b02861.

(9) Schütz, C.; Agthe, M.; Fall, A. B.; Gordeyeva, K.; Guccini, V.; Salajková, M.; Plivelic, T. S.; Lagerwall, J. P. F.; Salazar-Alvarez, G.; Bergström, L. Rod Packing in Chiral Nematic Cellulose Nanocrystal Dispersions Studied by Small-Angle X-Ray Scattering and Laser Diffraction. *Langmuir* **2015**, *31* (23), 6507–6513. https://doi.org/10.1021/acs.langmuir.5b00924.

(10) Dong, X. M.; Kimura, T.; Revol, J.-F.; Gray, D. G. Effects of Ionic Strength on the Isotropic−Chiral Nematic Phase Transition of Suspensions of Cellulose Crystallites. *Langmuir* **1996**, *12* (8), 2076–2082. https://doi.org/10.1021/la950133b.

(11) Hirai, A.; Inui, O.; Horii, F.; Tsuji, M. Phase Separation Behavior in Aqueous Suspensions of Bacterial Cellulose Nanocrystals Prepared by Sulfuric Acid Treatment. *Langmuir* **2009**, *25* (1), 497–502. https://doi.org/10.1021/la802947m.

(12) Araki, J.; Kuga, S. Effect of Trace Electrolyte on Liquid Crystal Type of Cellulose Microcrystals. *Langmuir* **2001**, *17* (15), 4493–4496. https://doi.org/10.1021/la0102455.

(13) Dong, X. M.; Gray, D. G. Effect of Counterions on Ordered Phase Formation in Suspensions of Charged Rodlike Cellulose Crystallites. *Langmuir* **1997**, *13* (8), 2404–2409. https://doi.org/10.1021/la960724h.

(14) Honorato-Rios, C.; Lehr, C.; Schütz, C.; Sanctuary, R.; Osipov, M. A.; Baller, J.; Lagerwall, J. P. F. Fractionation of Cellulose Nanocrystals: Enhancing Liquid Crystal Ordering without Promoting Gelation. *NPG Asia Materials* **2018**, 1. https://doi.org/10.1038/s41427-018-0046-1.

(15) Abitbol, T.; Kam, D.; Levi-Kalisman, Y.; Gray, D. G.; Shoseyov, O. Surface Charge Influence on the Phase Separation and Viscosity of Cellulose Nanocrystals. *Langmuir* **2018**. https://doi.org/10.1021/acs.langmuir.7b04127.

(16) Beck-Candanedo, S.; Roman, M.; Gray, D. G. Effect of Reaction Conditions on the Properties and Behavior of Wood Cellulose Nanocrystal Suspensions. *Biomacromolecules* **2005**, *6* (2), 1048–1054. https://doi.org/10.1021/bm049300p.

(17) Onsager, L. The Effects of Shape on the Interaction of Colloidal Particles. *Annals of the New York Academy of Sciences* **1949**, *51* (4), 627–659. https://doi.org/10.1111/j.1749-6632.1949.tb27296.x.

(18) Nordenström, M.; Fall, A.; Nyström, G.; Wågberg, L. Formation of Colloidal Nanocellulose Glasses and Gels. *Langmuir* **2017**, *33* (38), 9772–9780. https://doi.org/10.1021/acs.langmuir.7b01832.

(19) Chu, G.; Vasilyev, G.; Qu, D.; Deng, S.; Bai, L.; Rojas, O. J.; Zussman, E. Structural Arrest and Phase Transition in Glassy Nanocellulose Colloids. *Langmuir* **2020**, *36* (4), 979–985. https://doi.org/10.1021/acs.langmuir.9b03570.

(20) Reid, M. S.; Villalobos, M.; Cranston, E. D. Benchmarking Cellulose Nanocrystals: From the Laboratory to Industrial Production. *Langmuir* **2016**. https://doi.org/10.1021/acs.langmuir.6b03765.

(21) Beck, S.; Bouchard, J. Ionic Strength Control of Sulfated Cellulose Nanocrystal Suspension Viscosity. *Tappi Journal* **2016**, *15* (6), 363–372.

(22) Dammak, A.; Moreau, C.; Azzam, F.; Jean, B.; Cousin, F.; Cathala, B. Influence of Cellulose Nanocrystals Concentration and Ionic Strength on the Elaboration of Cellulose

Nanocrystals-Xyloglucan Multilayered Thin Films. *J Colloid Interface Sci* **2015**, *460*, 214–220. https://doi.org/10.1016/j.jcis.2015.08.048.

(23) Shafiei-Sabet, S.; Hamad, W. Y.; Hatzikiriakos, S. G. Ionic Strength Effects on the Microstructure and Shear Rheology of Cellulose Nanocrystal Suspensions. *Cellulose* **2014**, *21* (5), 3347–3359. https://doi.org/10.1007/s10570-014-0407-z.

(24) Boluk, Y.; Danumah, C. Analysis of Cellulose Nanocrystal Rod Lengths by Dynamic Light Scattering and Electron Microscopy. *J Nanopart Res* **2013**, *16* (1), 2174. https://doi.org/10.1007/s11051-013-2174-4.

(25) Vanderfleet, O. M.; Osorio, D. A.; Cranston, E. D. Optimization of Cellulose Nanocrystal Length and Surface Charge Density through Phosphoric Acid Hydrolysis. *Phil. Trans. R. Soc. A* **2018**, *376* (2112), 20170041. https://doi.org/10.1098/rsta.2017.0041.

(26) Jiang, F.; Esker, A. R.; Roman, M. Acid-Catalyzed and Solvolytic Desulfation of H2SO4-Hydrolyzed Cellulose Nanocrystals. *Langmuir* **2010**, *26* (23), 17919–17925. https://doi.org/10.1021/la1028405.

(27) Honorato Rios, C.; Kuhnhold, A.; Bruckner, J.; Dannert, R.; Schilling, T.; Lagerwall, J. Equilibrium Liquid Crystal Phase Diagrams and Detection of Kinetic Arrest in Cellulose Nanocrystal Suspensions. *Frontiers in Materials* **2016**, *3*. https://doi.org/10.3389/fmats.2016.00021.

(28) Derakhshandeh, B.; Petekidis, G.; Shafiei Sabet, S.; Hamad, W. Y.; Hatzikiriakos, S. G. Ageing, Yielding, and Rheology of Nanocrystalline Cellulose Suspensions. *Journal of Rheology* **2012**, *57* (1), 131–148. https://doi.org/10.1122/1.4764080.

(29) Shafiei-Sabet, S.; Hamad, W. Y.; Hatzikiriakos, S. G. Rheology of Nanocrystalline Cellulose Aqueous Suspensions. *Langmuir* **2012**, *28* (49), 17124–17133. https://doi.org/10.1021/la303380v.

(30) Xu, Y.; Atrens, A. D.; Stokes, J. R. “Liquid, Gel and Soft Glass” Phase Transitions and Rheology of Nanocrystalline Cellulose Suspensions as a Function of Concentration and Salinity. *Soft Matter* **2018**, *14* (10), 1953–1963. https://doi.org/10.1039/C7SM02470C.

(31) Shafiei-Sabet, S.; Hamad, W. Y.; Hatzikiriakos, S. G. Influence of Degree of Sulfation on the Rheology of Cellulose Nanocrystal Suspensions. *Rheol Acta* **2013**, *52* (8–9), 741–751. https://doi.org/10.1007/s00397-013-0722-6.

(32) Liu, D.; Chen, X.; Yue, Y.; Chen, M.; Wu, Q. Structure and Rheology of Nanocrystalline Cellulose. *Carbohydrate Polymers* **2011**, *84* (1), 316–322. https://doi.org/10.1016/j.carbpol.2010.11.039.

(33) Ureña-Benavides, E. E.; Ao, G.; Davis, V. A.; Kitchens, C. L. Rheology and Phase Behavior of Lyotropic Cellulose Nanocrystal Suspensions. *Macromolecules* **2011**, *44* (22), 8990–8998. https://doi.org/10.1021/ma201649f.

(34) Wu, Q.; Li, X.; Fu, S.; Li, Q.; Wang, S. Estimation of Aspect Ratio of Cellulose Nanocrystals by Viscosity Measurement: Influence of Surface Charge Density and NaCl Concentration. *Cellulose* **2017**, *24* (8), 3255–3264. https://doi.org/10.1007/s10570-017-1341-7.

(35) Haywood, A. D.; Davis, V. A. Effects of Liquid Crystalline and Shear Alignment on the Optical Properties of Cellulose Nanocrystal Films. *Cellulose* **2017**, *24* (2), 705–716. https://doi.org/10.1007/s10570-016-1150-4.

(36) Boluk, Y.; Lahiji, R.; Zhao, L.; McDermott, M. T. Suspension Viscosities and Shape Parameter of Cellulose Nanocrystals (CNC). *Colloids and Surfaces A: Physicochemical and Engineering Aspects* **2011**, *377* (1), 297–303. https://doi.org/10.1016/j.colsurfa.2011.01.003.

(37) Lu, A.; Hemraz, U.; Khalili, Z.; Boluk, Y. Unique Viscoelastic Behaviors of Colloidal Nanocrystalline Cellulose Aqueous Suspensions. *Cellulose* **2014**, *21* (3), 1239–1250. https://doi.org/10.1007/s10570-014-0173-y.

(38) Van Rie, J.; Schütz, C.; Gençer, A.; Lombardo, S.; Gasser, U.; Kumar, S.; Salazar-Alvarez, G.; Kang, K.; Thielemans, W. Anisotropic Diffusion and Phase Behavior of Cellulose Nanocrystal Suspensions. *Langmuir* **2019**, *35* (6), 2289–2302. https://doi.org/10.1021/acs.langmuir.8b03792.

(39) Johan Foster, E.; J. Moon, R.; P. Agarwal, U.; J. Bortner, M.; Bras, J.; Camarero-Espinosa, S.; J. Chan, K.; D. Clift, M. J.; D. Cranston, E.; J. Eichhorn, S.; M. Fox, D.; Y. Hamad, W.; Heux, L.; Jean, B.; Korey, M.; Nieh, W.; J. Ong, K.; S. Reid, M.; Renneckar, S.; Roberts, R.; Anne Shatkin, J.; Simonsen, J.; Stinson-Bagby, K.; Wanasekara, N.; Youngblood, J. Current Characterization Methods for Cellulose Nanomaterials. *Chemical Society Reviews* **2018**, *47* (8), 2609–2679. https://doi.org/10.1039/C6CS00895J.

(40) Haywood, A. D.; Weigandt, K. M.; Saha, P.; Noor, M.; Green, M. J.; Davis, V. A. New Insights into the Flow and Microstructural Relaxation Behavior of Biphasic Cellulose Nanocrystal Dispersions from RheoSANS. *Soft Matter* **2017**, *13* (45), 8451–8462. https://doi.org/10.1039/C7SM00685C.

(41) Schneider, C. A.; Rasband, W. S.; Eliceiri, K. W. NIH Image to ImageJ: 25 Years of Image Analysis. *Nature Methods* **2012**, *9* (7), 671–675. https://doi.org/10.1038/nmeth.2089.

(42) Klockars, K. W.; Tardy, B. L.; Borghei, M.; Tripathi, A.; Greca, L. G.; Rojas, O. J. Effect of Anisotropy of Cellulose Nanocrystal Suspensions on Stratification, Domain Structure Formation, and Structural Colors. *Biomacromolecules* **2018**, *19* (7), 2931–2943. https://doi.org/10.1021/acs.biomac.8b00497.

(43) Xu, Y.; Atrens, A. D.; Stokes, J. R. Rheology and Microstructure of Aqueous Suspensions of Nanocrystalline Cellulose Rods. *Journal of Colloid and Interface Science* **2017**, *496*, 130–140. https://doi.org/10.1016/j.jcis.2017.02.020.

(44) de Rivera, M. R.; Socorro, F.; Matos, J. S. Heats of Mixing Using an Isothermal Titration Calorimeter: Associated Thermal Effects. *Int J Mol Sci* **2009**, *10* (7), 2911–2920. https://doi.org/10.3390/ijms10072911.

(45) Grolier, J.-P. E.; del Río, J. M. On the Physical Meaning of the Isothermal Titration Calorimetry Measurements in Calorimeters with Full Cells. *Int J Mol Sci* **2009**, *10* (12), 5296–5325. https://doi.org/10.3390/ijms10125296.

(46) Morini, G. L. Viscous Heating. In *Encyclopedia of Microfluidics and Nanofluidics*; Li, D., Ed.; Springer US: Boston, MA, 2013; pp 1–11. https://doi.org/10.1007/978-3-642-27758-0_1670-2.

(47) Warren, R. C. Viscous Heating. In *Rheological Measurement*; Collyer, A. A., Clegg, D. W., Eds.; Springer Netherlands: Dordrecht, 1993; pp 119–149. https://doi.org/10.1007/978-94-017-2898-0_5.

CHAPTER 4

Synergistic ionic complexes of cellulose nanofibrils and nanochitin are pH responsive with precise tunability

4.1 ABSTRACT Biobased nanomaterials, especially nanocellulose and nanochitin, are a promising resource due to their sustainability and suitability for use in a broad variety of applications. In this work we demonstrate how ionic complexes in aqueous suspension can employ the complementary properties of cationic nanochitin (NCh) and anionic cellulose nanofibrils (CNF) to develop a hybrid material with precise control over rheological properties and pH responsive behavior. Adjusting the pH environment of the suspensions can induce or prohibit complex formation by changing the protonation state of one or both constituent nanoparticles. Using this principle, we were able to finely adjust the elastic modulus (G') of the complex in aqueous suspension across a full order of magnitude (~2 Pa to ~20 Pa) while keeping the solids content of the suspension constant at 0.5 wt. %. We utilized isothermal titration calorimetry to measure and characterize the interparticle interactions, allowing us to select the NCh and CNF ratios and pH conditions to generate a particular rheological profile. The wide variety of morphologies and surface chemistries available in biobased nanomaterials present an opportunity to create a vast library of nanomaterial complexes with properties targeted for specific applications.

4.2 INTRODUCTION

Biobased nanomaterials are an active and growing topic of study, with particular focus on nanocellulose due to its abundance and, more recently, nanochitin due to its analogous and complementary properties.[1] This class of materials presents a number of advantages derived from their tunable surface chemistry and morphology, making them attractive candidates for many diverse applications. Incorporation of these materials is driven largely by a societal motivation to increase the utilization of biobased components and thereby decrease negative environmental impacts, such as reliance on single-use plastics, dependence on fossil fuels and use of harsh solvents and reagents. They have been employed in medical uses[1,2], water purification,[3] emulsion stabilization,[4,5] and many other fields with great success.

In nearly all these applications, a working understanding of the rheological behavior is imperative to optimize the system properties and processing conditions. To this end, numerous rheological studies have been conducted on nanocellulose[6–10] and (to a lesser extent) nanochitin,[11–14] but detailed studies on the rheology of systems of the two materials combined remain scarce. Such mixed systems are worthy of detailed study, since engineering materials that employ the assets of both nanoparticles can create unique advantages for different applications. For example, manipulating the behavior of oppositely charged materials is a useful tool to create physically crosslinked structures with tunable properties. This strategy has been employed in layer by layer assembly methods[15] and fabrication of self-assembled microfibers,[16] most often with oppositely charged polyelectrolytes like polydiallyldimethylammonium chloride (polyDADMAC) and polystyrene sulftonate (PSS). The opposite charges present on certain forms of nanocellulose and nanochitin make them promising candidates for this technique.[17] This strategy also aligns with the broader goal to decrease environmental impact, by mitigating or reducing the use of crosslinking agents.

The conditions and properties of ionic complex formation pertaining to polyelectrolytes have been studied in quite some detail.[18] They have well-documented use in drug delivery[19] and have noteworthy rheological properties,[20] including the propensity to form coacervates.[21] Additionally, there have been several fundamental studies which make use of isothermal titration calorimetry in the analysis of thermodynamics of polyelectrolyte complex (PEC) formation which have provided important insights.[22–26] Namely, the work by Fu and Schlenoff[23] detailing the enthalpy changes affiliated with ion exchange for a series of different counterion affinities is of great importance to any thermodynamic investigation of PEC formation. Lounis et al. provided valuable insight about the relationship between charge density and the stoichiometry of complex formation, using PDADMAC/PSS as a model system.[24] Another illuminating study, by Huang and Lapitsky,[27] conducted an investigation to formation of colloidal particles and subsequently macroscopic aggregates as counterions are added to polyelectrolytes. Work by Feng et al[22] distinguished between complex formation of strong and weak polyelectrolytes and presented several important considerations regarding ionization of species at changing pH which are expected to be applicable in the complex formation of colloidal biobased nanomaterials.

Despite the illuminating body of work regarding the characterization of model polyelectrolyte systems, fundamental understanding of the same method as it applies to biobased colloidal nanomaterials is less thorough. However, works dealing with complexes of polymeric forms cellulose, chitin or chitosan[28–30] can be a good starting point to understand and predict the interactions of the corresponding colloidal nanomaterials. Benselfelt et al. evaluated the of use anionic carboxylated cellulose as a substrate for multilayers of PDADMAC/PSS,[30] which is a well-known PEC system. Two other studies[28,29] explored composites or blends of cellulose and chitin polymers, referring to benefits derived from hydrogen bonding between the two, but neither case mentioned the potential for ionic complex formation between charged forms. Many studies that contain efforts to create composites of polymeric cellulose and/or chitin have also involved the use of ionic liquids,[31–34] which can be avoided if the colloidal nanomaterial forms are used instead.

Separate works have delved into the task of creating ionic complexes from colloidal biobased nanomaterials, but in many cases, these have been heavily focused on their respective applications, and the studied systems were often confined to aerogel or hydrogel morphologies.[11,35–38] Two additional works[16,39] developed fibril morphologies by complexing anionic CNF with cationic chitosan or PDADMAC, both with great success. A similar principle has been employed to ionically crosslink alginate using calcium in electropsun mats.[40]

Although a wide variety of hybrid biobased nanomaterial systems is emerging in the literature, much of the fundamental basis for creating, optimizing and tuning these materials remains unexplored. The objective of this study is to look closely at the interactions which drive formation of ionic complexes, in particular those that are relevant for biobased colloids such as nanocellulose and nanochitin. Some key aspects of such behavior include the charge ratio stoichiometry, ionization effects in changing pH conditions, and the manifestation of the ionic interactions in the microstructure of the materials, which can be evaluated by studying the rheological properties. Using rheology to elucidate the microstructure and calorimetry to quantify specific particle interactions, we will demonstrate the importance of pH effects that must be thoroughly understood in order to successfully take advantage of the ionic behaviors of biobased nanomaterials and explain how these can be manipulated to finely tune the rheological properties of the mixed aqueous suspension. The microstructural details of composite/complex properties determined through rheological measurements will be coordinated with the corresponding measured interactions of the starting materials, with a particular focus on semi-dilute solutions, rather than hydrogels, aerogels, or fibril morphologies. Such semi-dilute solutions are best suited for calorimetric studies and can provide a basis for understanding of interactions in other designed systems.

4.3 EXPERIMENTAL

4.3.1 Materials

CNF was prepared according to a method previously described.[4,41] Briefly, disintegrated birch fibers from a Finnish pulp mill were disintegrated via 6 passes of high-energy microfluidization (M110P, Microfluidics Int. Co., Newton MA). No enzymatic or chemical treatment was applied, so any surface charges present are the result of residual carboxylates.[41–43] The preparation of NCh was described in our previous report.[44] In brief, the sample designated as NCh-S is equivalent to the NCh used in this work. Purified α-chitin (obtained from frozen blue crabs at a Finnish seafood market) was treated with 33 wt % NaOH solution at 90 °C for 3.5 h, at a liquid-to-solid ratio of 25 mL/g[45]. The resulting partially deacetylated chitin was washed, dried, redispersed in Milli-Q water, and the pH was adjusted to 3.0 before subjecting the sample to mechanical defibrillation using a high speed blender (T-25 Ultra-Turrax Digital Homogenizer, IKA, Germany). The resultant coarse suspension was further processed to fine suspension via ultrasonication (Sonifier 450, Branson Ultrasonics Co., Danbury, CT, U.S.A.; 40 minutes at 50% strength, 5 s on-2 s off). Centrifugation (5 min 10,000 rpm) was carried out after ultrasonication to remove remaining large particles. Concentration was adjusted by addition of MilliQ water followed by vortex mixing (~10 s). Adjustment of pH conditions was done by addition of dilute sodium hydroxide or hydrochloric acid as needed.

4.3.2 Methods

Titration experiments were done using a Low Volume NanoITC isothermal titration calorimeter. In this technique, a suspension of aqueous NCh is incrementally injected to a sample cell containing aqueous CNF. The heater power required to maintain isothermal conditions is continuously monitored and is automatically reduced or increased to account for any heat absorbed or evolved by the interactions taking place in the sample cell. As such, the heat rate can be integrated to provide a quantitative indication of the heats of interaction between two materials. To measure the interactions between nanochitin and nanocellulose, a 0.01 wt% NCh aqueous suspension was titrated into 0.05 wt% CNF aqueous suspension, in a series of 25 injections of 2 μL each with an equilibration time of 400 s between injections. These initial concentrations were established after previous experiments with higher NCh ratios showed the heat signal to be saturated after a single injection. Corresponding blank experiments were also performed using the same protocol to decouple competing effects and background heats. These included NCh into water, water into CNF, acid into CNF, neutralized NCh into CNF, and NCh into acidic CNF. Relevant data sets are included in **Figure C.1**. Injection equilibration time used was 400 s, but equivalent results were obtained for injection times up to 1200 s (**Figure C.2**). The first injection is often conventionally excluded from analysis[46] due to baseline equilibration effects and diffusion out of the syringe during the equilibration period. A standard injection volume of 2.5 μL was used for all experiments. Steady and dynamic oscillatory rheological experiments were conducted on an Anton Paar MCR 300 rheometer with a 25 mm parallel plate geometry, using a 1 mm measuring gap. Steady shear viscosity measurements were done for shear rates ranging from 10^{-2} to 10^{2} s^{-1}. Frequency sweeps were performed at an oscillatory strain of 1%, determined to be within the linear viscoelastic regime according to oscillatory strain sweeps. The lower limit of frequencies for the low modulus sample(s) was often dictated by the transducer limit of the rheometer Tests were repeated in triplicate and standard errors were < 15%. Average values are reported.

4.4 RESULTS & DISCUSSION

To understand the formation of ionic complexes between CNF and NCh, comprehending ionization of the constituent nanoparticles is a critical prerequisite. In both materials, the charge group responsible for forming the complex is subject to deionization under specific pH conditions. These charges are also responsible for the colloidal stability of the materials by maintaining electrostatic repulsion in aqueous suspension. NCh is colloidally stable at pH < 6 due to the protonated amine group, which has a pKa of 6.3 according to previous studies.[12] At pH 6, ~65% of the amine groups are protonated as calculated by the Henderson Hasselbach equation[47] and there is a known decrease in colloidal stability (ζ-potential 30 mV)[48] compared to pH 5, where ~95% of the groups are protonated (ζ-potential 60 mV, **Figure C.3**). Similarly, CNF is colloidally stable for pH > 4, due to the pKa (~3.6) of the residual carboxylate groups on the fibril surfaces. Below 3.9, the COO- is protonated to COOH and in the absence of electrostatic repulsion, the particles aggregate.[49–52]

4.4.1 Microstructure comparison of NCh, CNF and mixed system

Figure 4.1 shows the dynamic and steady shear rheological properties of NCh and CNF and their combinations under different conditions. When both materials are at their native pH based on their preparation protocols (*i.e.*, ~7 for CNF and ~4 for NCh), the microstructure of each suspension is based primarily on the morphology and aspect ratio of the colloidally stable nanoparticles (represented schematically in the cartoons presented with the plots).

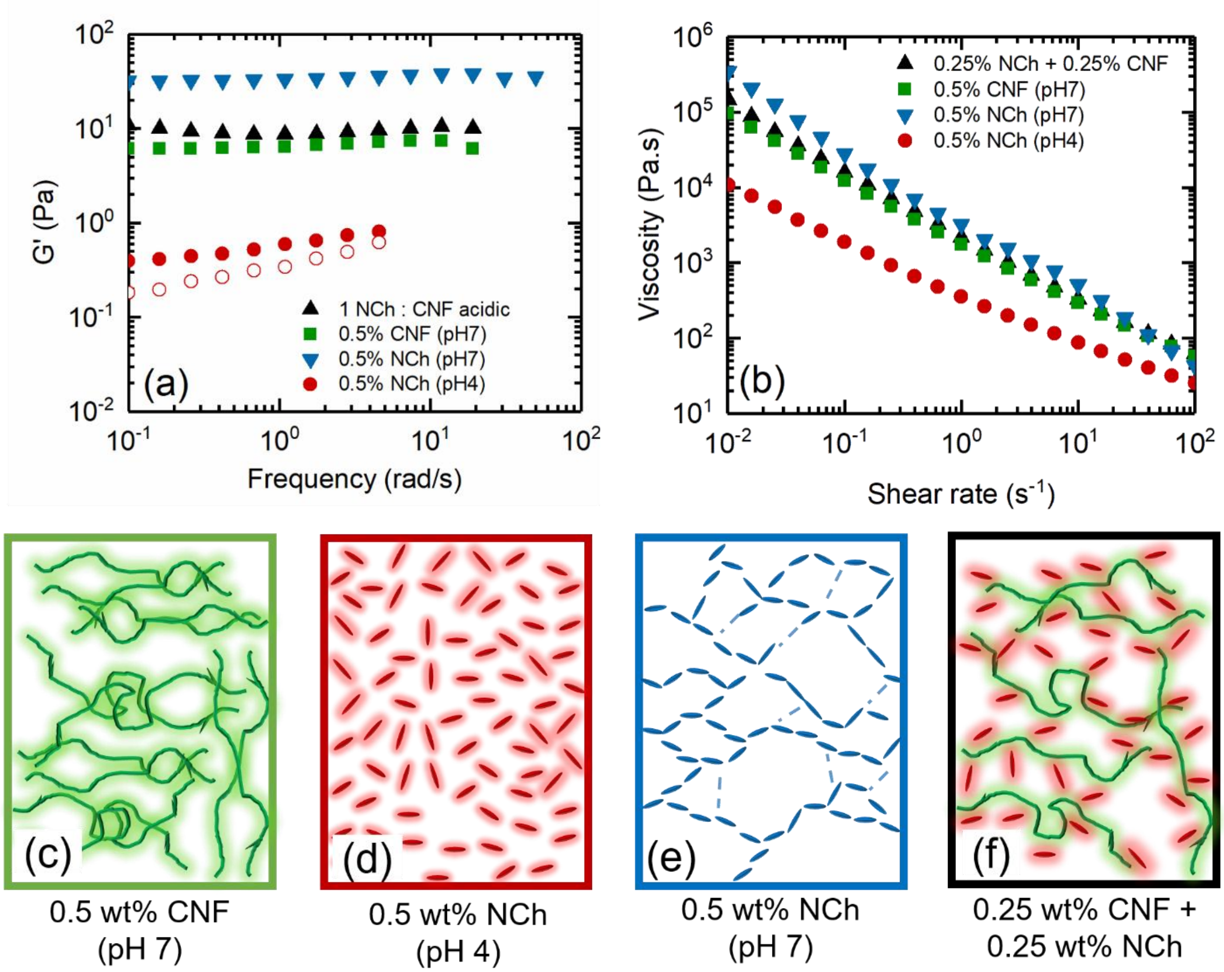

Figure 4.1. (a) Elastic modulus (G') as a function of frequency, and (b) shear-dependent viscosity of four different systems. The loss modulus (G'') of only one sample is shown for the sake of clarity. Stable CNF system (green squares) exhibits higher elasticity and viscosity compared to stable NCh system (red circles). Elastic modulus and viscosity of aggregated NCh system (blue inverted triangles) and of NCh/CNF mixtures (black triangles) are higher than the individual components, due to attractive forces inducing aggregation of NCh and complexation in the mixed system. (c-f) Schematic illustrations of each system

Under these conditions, the elastic modulus of the CNF system (~6 Pa) is approximately an order of magnitude higher than the NCh system (~0.4 Pa) (**Figure 4.1a**), at equivalent solids content

(0.5 wt. %). CNF is clearly gel-like, as we see that G' is independent of frequency and is higher than G" (complete data set shown in **Appendix C**, **Figure C.4)**. NCh shows weak-gel like features with G' becoming flat at low frequencies and larger than G'' as seen for many weak gel systems.[53] This result is consistent with the viscosity versus shear rate plot (**Figure 4.1b**) where we see the absence of a Newtonian plateau at low shear rate indicating buildup of network structure. The viscosity of CNF shows similar features except has a higher value. Possible schematic representations of the microstructure are shown in the bottom row of **Figure 4.1**. It is expected that the CNF system will have a higher elastic modulus and viscosity when both systems are colloidally stable, by virtue of its higher aspect ratio, and the length and flexibility of the fibrils which promote entanglement. The aspect ratio of CNF is estimated to be on the order of ~100 or more (**Figure C.5**), although as previously noted,[54] quantitative measurements fibril length are challenging due to entanglement and fibrils passing in and out of the field of view. NCh aspect ratio for the samples used here was previously quantified as ~15 by Bai et al.[5] and a qualitative sense of the different aspect ratios of the materials can be gleaned from microscopy images (**Figure C.5,6**). The increased entanglement and higher number of contact points in the CNF network reduce the mobility of the fibrils, resulting in higher viscosity and elasticity of the gel-like system.

When the pH of the NCh system is adjusted from 4 to 7 (above the pKa of NH_3^+), the elastic modulus increases by about two orders of magnitude, from ~0.4 to ~30 Pa (**Figure 4.1a**, red and blue symbols respectively). This can be attributed to aggregation of particles as the electrostatic repulsion is reduced or eliminated by the deprotonation of the stabilizing amine groups ($NH_3^+ \rightarrow NH_2$). Attractive van der Waals forces and hydrogen bonding can now facilitate assembly of a network structure of NCh particles. Previous cases[55] have shown that such aggregation often favors an end-to-end configuration due to the lowest density of charge groups being on the particle end, resulting in an increased effective aspect ratio. This is depicted in the cartoon (**Figure 4.1e**)

Based on this understanding of the aspect ratio effect, an equal mixture of shorter NCh and longer CNF in stable suspension would be expected to have a G' value which falls between the values measured for each individual component. However, we find instead that the mixed system (pH ~5.5) at the same total solids content has an elastic modulus and viscosity that are slightly *higher* than either individual component (**Figure 4.1**, black symbols). We can attribute this to the attractive forces between the negatively charged CNF particles and positively charged NCh particles resulting in increased effective aspect ratio, ionic crosslinking, network formation, and therefore increased viscosity and structural elasticity. We envision the extent of this synergistic effect to be a function of the ratio of the two components, a topic we explore in a subsequent section.

4.4.2 Thermal interactions between NCh and CNF

To quantify these hypothesized interactions between charged particles, we make use of ITC to calorimetrically detect the interactions when the components are mixed. The thermogram for a titration of NCh into CNF is shown in **Figure 4.2**. **Figure 4.2a** represents the continuous power supplied by the feedback heater to maintain isothermal conditions, which is a direct function of the heat evolved or generated by the interactions in the cell. **Figure 4.2b** represents that heat rate integrated with respect to time and plotted as discrete values associated with each individual injection. The secondary y-axis shows pH of the sample cell. A positive heat value indicates an exothermic event in the sample cell. Note that while the initial prepared NCh suspension at 0.5 wt. % was at pH 4, dilution with DI water to concentration 0.01 wt. % increases the pH to ~5.

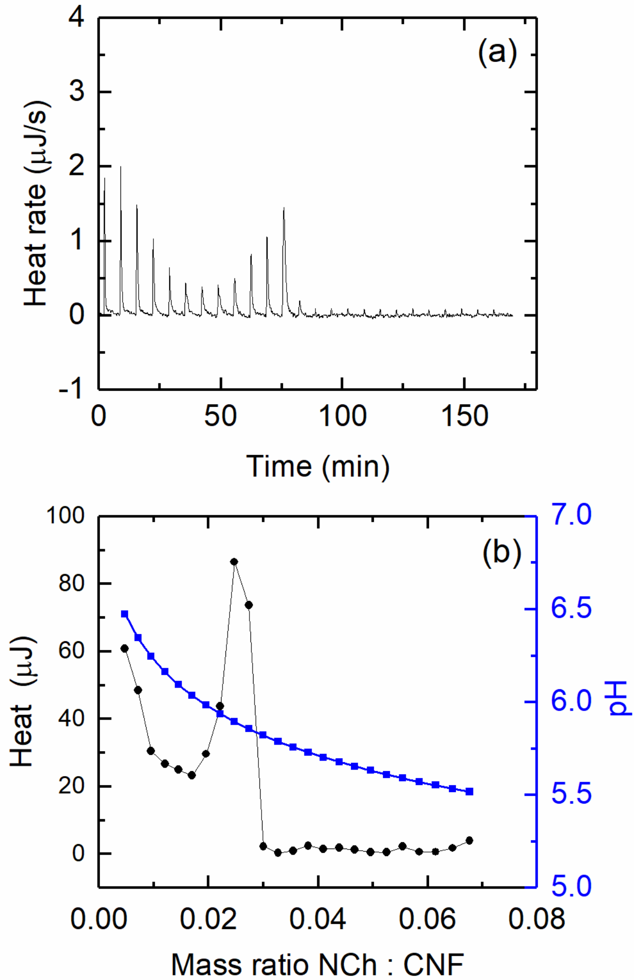

Figure 4.2. ITC thermogram of 0.01 wt. % NCh (pH 5) injected into 0.05 wt. % CNF (pH 7). (a) continuous heat rate measured in the cell (b) integrated heat values for each injection. Positive heat value indicates an exothermic event.

There are several factors that are important to recognize with respect to interpreting the thermogram. As previously noted, the charge groups on both species are sensitive to pH changes. Prior to the beginning of the ITC experiment, each component is at its native pH resulting from its preparation method. This means that with each injection of NCh suspension (pH 5) into CNF suspension (pH 7), there is a pH change to consider in addition to the potential ionic complex formation. Since the particles must be in charged form in order to form complexes, it is important to track the ionization of each species throughout the experiment, as the ionization state will directly impact the interparticle interactions. The calculated pH value for each injection is shown on the secondary y-axis for reference (**Figure 4.3a**). Calculations have been confirmed by checking the pH at the end of the experiment and for select ratios in the middle of the titration. Taken together, the charge densities and changing pH environment can account for the 3-regime shape that we see in the thermogram, which we will discuss in terms of Regime 1 (injections 1-6, up to mass ratio 0.02 g NCh to g CNF), Regime 2 (injections 7-10, ratio 0.02-0.03) and Regime 3 (injections 11-24, mass ratio ≥ 0.03).

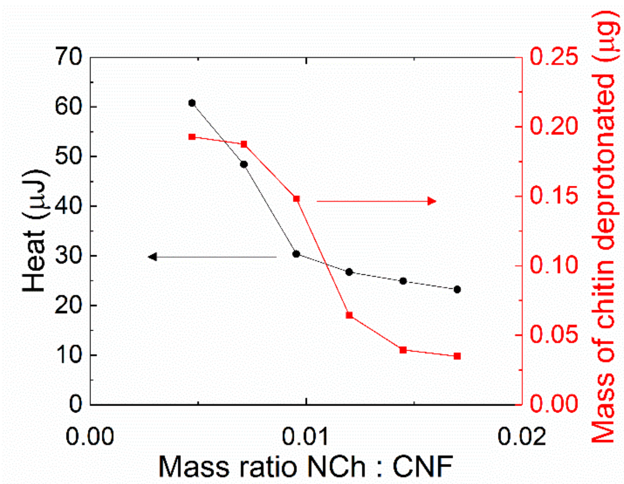

Figure 4.3. In first regime of titration the dominant interaction is deprotonation of nanochitin (pH 5) as it is injected into the sample cell (pH 7). (a) In Regime 1, the magnitude of the heat signal closely follows the mass of nanochitin deprotonated for each injection (shown on secondary axis) until the pH reaches ~6 and deprotonation is no longer favored. (b) Deprotonation and protonation of nanochitin are driven by pH changes.

Regime 1 (deprotonation): **(Figure 4.3)** Throughout the experiment, the pH is decreasing due to the addition of acidic NCh (**Figure 4.2b**), but at the start of the experiment the bulk pH in the cell is above 6.3 (pKa of NH_3^+ charge groups on NCh). This means the initial injections result in deprotonation of NH_3^+ to NH_2. Similar interactions have been shown for titration of acidic chitosan into neutral pH liposomes.[56] Since the nanochitin used here is partially deacetylated, the surface chemistry is closely related to that of chitosan. The mass of chitin deprotonated with each injection *decreases* as the pH *increases* in the cell due to NCh addition, causing a corresponding increase in the % ionization of the amine groups. This accounts for the decrease in the magnitude of the heat signal through Regime 1, which tracks closely with the calculated mass of chitin deprotonated during each injection (**Figure 4.3a**) (See **Appendix C** for details on calculation of deprotonated chitin). The earliest injections represent extensive deprotonation (**Figure 4.4**, purple highlighted region), but with continued addition of NCh, the pH decreases and the equilibrium shifts to favor protonated NCh. At the end of Regime 1, the pH in the cell has decreased to 6.0, which corresponds to 65% protonation of NH_3^+ as calculated by the Henderson-Hasselbach equation. At this point, further deprotonation of incoming NCh is no longer favored, and there is enough positively charged NCh in the cell to drive ionic complex formation with negatively charged CNF. Throughout this experiment the pH is still well above the pKa of the CNF carboxylate group (~3.6), so no protonation of that species is expected. For reference, heat of dilution of an equivalent pH change (without protonation/deprotonation) exhibits a small and constant value of ~10 μJ (**Figure C.7**).

Regime 2 (complexation): As ionic complex formation proceeds, the pH continues to decrease with continued addition of NCh, and ionic complex formation correspondingly becomes more vigorous due to the increased availability of positively charged NCh. For this reason, the magnitude of the heat signal, which had previously been decreasing due to decreasing driving force for protonation of NH_3^+, begins to increase (**Figure 4.4**, yellow highlighted region). The increase continues through Regime 2 for three injections as ionization of NH_3^+ increases (from 65% at pH

6.0, injection 6 to 75% at pH 5.8) and availability for ionic complex formation increases correspondingly. A brief decrease for 1 injection follows, this being the injection where the CNF charges are fully consumed. The last injection of Regime 2 is therefore smaller than the previously increasing ones, because although the ionization of NCh is still increasing, the NCh entering the cell during this injection does not have a full stoichiometric equivalent of CNF charge available to complex, and hence the magnitude of heat signal is decreased.

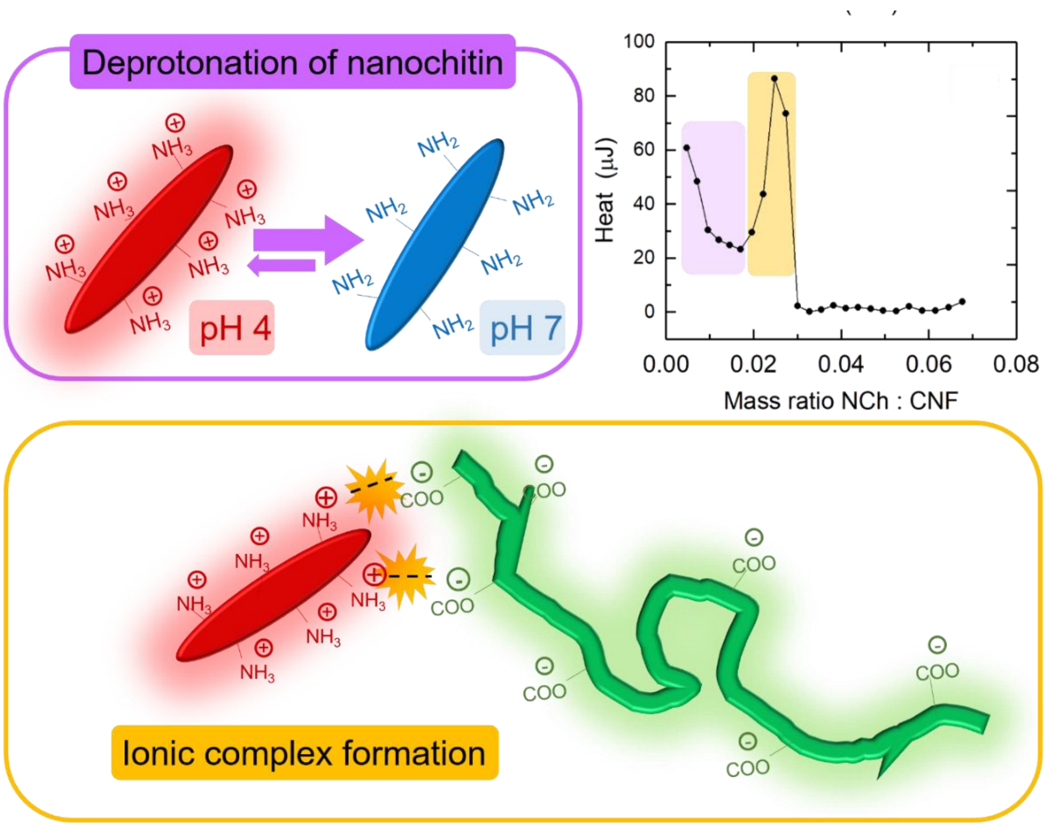

Figure 4.4. Schematics of interactions in Regime 1 (top left, purple highlighted region) and Regime 2 (bottom, yellow highlighted region). Magnitude of heat signal for deprotonation decreases throughout Regime 1 as the pH decreases and equilibrium shifts to favor the protonated form of NCh. Magnitude of heat signal for ionic complex formation initially increases as ionization of NCh is increased and driving force for complexation improves, heat signal subsequently decreases when charge groups on CNF are consumed.

Regime 3 (saturation): It is evident that after mass ratio 0.03 g NCh per g CNF, the heat signal is reduced to a small constant value, found to be less than or equivalent to the background heat of dilution measured in a blank experiment (i.e. injecting NCh into pH 7 water, **Figure C.1**). This is an indication that at this mass ratio, the number of charge groups associated with NCh has exceeded the number of available charge groups associated with CNF, and further addition of NCh does not result in complexation or other measurable interaction. Previous trials which made use of higher initial concentrations of NCh (**Figure C.8**) reached this ratio with fewer injections but showed the same leveling-off behavior at the same ratio, corroborating the hypothesis that this is an indication of fully "saturated" CNF charges. The saturation occurs at a mass ratio of approximately 0.03 g NCh per g CNF. It has previously been noted that CNF (prepared by mechanical methods and free from chemical modification) has a substantially lower charge density (~40-80 mmol/kg)[42] than typical deacetylated NCh (~120-300 mmol/kg)[57], and this particular sample of NCh has an even higher estimated surface charge of ~1500 mmol/kg[5] so it is not surprising that the charges are consumed so quickly. Analogous interactions for polyelectrolyte complexes of polylysine (PLL) and copolymers of acrylamide and 2-acrylamido-2-methyl-1-propanesulfonate (PAMAMPS) have been studied by Lounis et al.,[24] where the heat signal levels off once charge compensation is reached. The stoichiometric charge equivalence at a mass ratio of 0.03 is corroborated by the fact that the zeta potential crosses from negative to positive somewhere between a ratio of 0.02 and 0.11 (**Figure C.9**). Further addition of NCh beyond this point does not interact to form an ionic complex, but does cause the pH to continue decreasing.

To verify the limits of the pH conditions, we performed two blank experiments where the pH conditions were outside of the window in which complexation is expected. In the first of these (**Figure 4.5a,b**), the CNF suspension was adjusted to pH 3 prior to the titration with NCh. In this case, the COO- groups on the CNF surface are largely (~90%) protonated to neutral charge COOH, and thus are not inclined to form ionic complexes with the cationic NCh. Indeed, the heat signature measured for this titration is comparable to the signal of NCh into water (**Figure C.5**), and we conclude that no interaction takes place. In the second experiment (**Figure 4.5c,d**) NCh was adjusted pH 7 prior to the titration. In this case, cationic NH_3^+ is ~83% deprotonated to neutral charge NH_2, and similarly no ionic complexation is detected in the thermogram. There is a slight increase in the magnitude of the heat with each injection over the course of the experiment (**Figure 4.5d**), which may be an indication of increased viscous heating as the NCh content increases and the particles, which are no longer colloidally stable at neutral pH, form aggregates and cause the viscosity to increase. The injection syringe maintains the same stir rate of 350 rpm throughout the experiment as the medium becomes increasingly more viscous, the heat evolved increases correspondingly.[58]

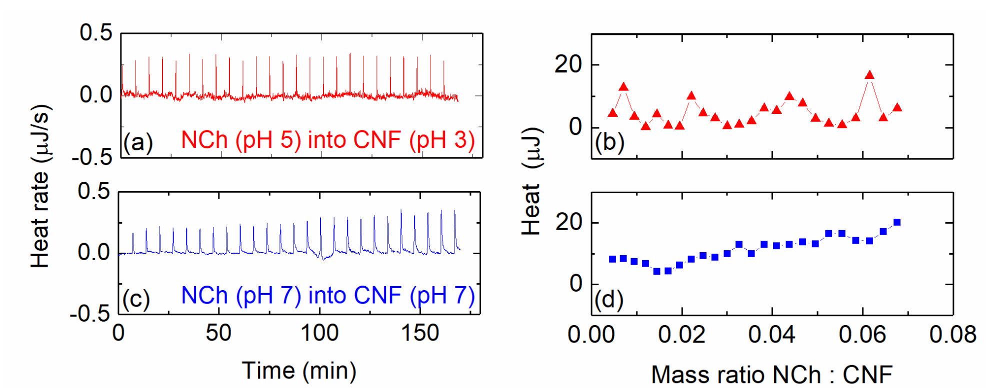

Figure 4.5. Comparison of NCh/CNF titration at different pH conditions. Acidic NCh injected into acidic CNF (a,b) shows no ionic complex formation, since adjustment of CNF to pH 3 causes protonation of the anionic COO^- to neutral charge COOH. (c,d) Similarly, nanochitin that has been pH-neutralized prior to injection shows no binding interaction, since the positive charges responsible for the ionic complexation are dependent on the amine groups being in protonated form (NH_3^+).

4.4.3 Order of operations and pH conditions

Given the demonstrated sensitivity to pH conditions and the earlier observations regarding the viscosity and elasticity of the suspensions and their dependence on aspect ratio and particle interactions, we identified an opportunity to tune the rheology by manipulating this behavior. To this end, we considered two main variables: First, the ratio of NCh to CNF, of which we tested three values: 1, 0.11, and 0.02 g NCh per g CNF (all at total solids content 0.5 wt%). And second, the pH environment of the mixture, of which we tested three conditions: (1) no pH adjustment, (2) "preneutralization," or pH adjustment of acidic NCh (from ~4 up to ~7) *before* mixing with CNF, and (3) "postneutralization," meaning pH adjustment of the system *after* mixing (from ~5 up to ~7). The order of operations is important, because for the ionic complexation of NCh and CNF to proceed the NCh amine groups must be in their protonated form (at low pH) before mixing. As such, we expect that for addition of preneutralized NCh to CNF, the particles will not interact. This expectation is strengthened by the ITC result shown in **Figure 4.5c,d**. However, in the postneutralized system, the cationic amine groups will already have complexed with anionic carboxylates on CNF. In this case, only excess amine groups beyond the charge equivalence of CNF will be neutralized when the pH is adjusted. The frequency spectra for the various conditions are shown in **Figure 4.6**. G" is only shown for one sample on each plot to maintain clarity, but the full data sets including G" can be found in **Appendix C** (**Figure C.10**).

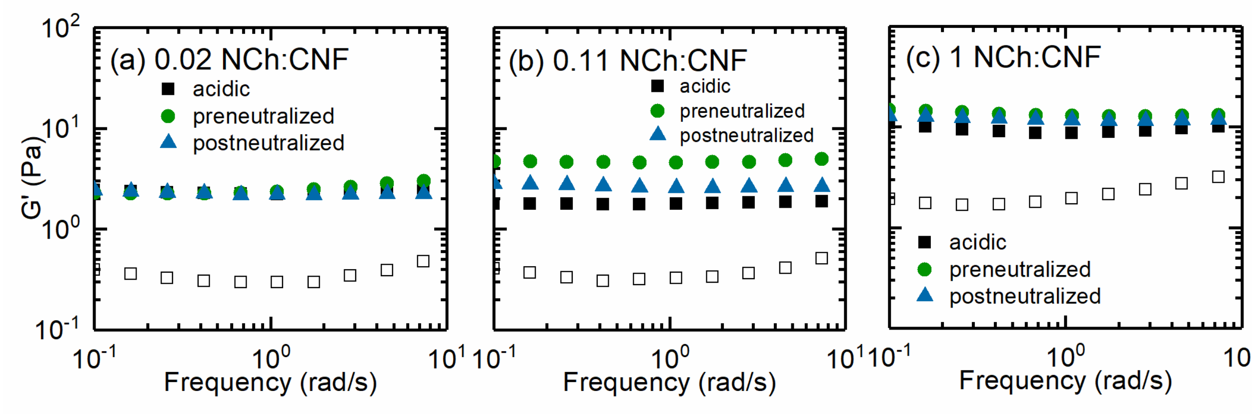

Figure 4.6. Frequency spectra for (a) 0.02 g NCh per g CNF, (b) 0.11 g NCh per g CNF, (c) 1 g NCh per g CNF. Colors and symbols indicate the pH conditions; black squares indicate no pH adjustment; green circles indicate pH of NCh adjusted to 7 *before* mixing (preneutralized); blue triangles indicate pH of system adjusted to 7 *after* mixing (postneutralized). Viscous modulus G" is shown for one data set in each plot for reference, but all G" values follow similar behavior.

Low NCh content (**Figure 4.6a**) In the case of the lowest ratio of nanochitin, there is no substantial difference in the value of the elastic modulus for different pH conditions. This is because of the large excess of CNF, which dictates that CNF entanglement is still the dominant rheological influence. It is worth noting that the value of G' for all three systems at this ratio (~2 Pa at frequency 1 rad/s) is in fact slightly higher than for pure CNF (0.7 Pa, **Figure 4.1a**). This can be attributed to a small increase in G' caused by aggregation (in the case of preneutralized NCh) or ionic complexation (in the case of acidic or postneutralized NCh). Both cases are associated with attractive particle interactions which would be expected to cause an increase in G'.

Medium NCh content (**Figure 4.6b**) The impact of neutralizing NCh is most evident at this ratio (0.11 g NCh per g CNF), because it is only slightly in excess of the stoichiometric ratio of NCh charges to CNF charges (~0.03 g NCh per g CNF). In this case, G' appears to be a direct function of the mass of NCh *subjected to pH adjustment*. Although the mass of NCh is constant among these three samples, the amount available for conversion of NH_3^+ to NH_2 is not constant. For the postneutralized system, a fraction of the NH_3^+ groups on the NCh surface are irreversibly complexed with COO- groups on CNF and are thus unavailable to be neutralized when the pH is adjusted. For the preneutralized NCh, *all* of the NH_3^+ groups are deprotonated. This means they are unavailable to complex with CNF and instead form aggregates in the absence of the stabilizing charges. This sample therefore has the highest G', due to having the most neutralized NCh and therefore the most aggregation. In the acidic sample (free from pH adjustment), the NCh remains protonated and no aggregation takes place, hence G' shows the lowest value. **Figure 4.7** shows G' of all samples plotted as a function of neutralized chitin content, and highlights the strong influence of aggregation on the structural properties.

High NCh content (**Figure 4.6c**) In the case of the equal mixture (1 g NCh per g CNF), NCh is in extreme excess of the stoichiometric charge equivalent to CNF. The dominant rheological effect is therefore aggregation of NCh particles, and as such the elastic modulus is higher than for the other ratios or for a pure CNF system.The system which was left in acidic condition (no pH adjustment) exhibits the lowest modulus, since aggregation is not a significant factor in this case because the amine groups remain protonated. The difference between the sample neutralized before mixing and the one neutralized after mixing is small and is proportionate to the number of groups that were irreversibly complexed with CNF and thus unavailable for deprotonation.

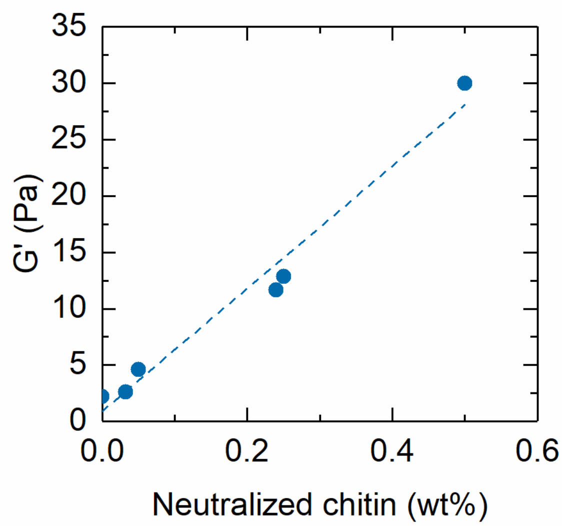

Figure 4.7. Elastic modulus (G') plotted as a function of excess deprotonated nanochitin (nanochitin beyond the established stoichiometric charge equivalent of cellulose nanofibrils). When aggregation is present in the system, it is the dominant rheological influence over entanglement and ionic attraction.

It is evident from **Figure 4.7** that the extent of NCh aggregation has a powerful influence on the microstructure of the mixed system. It is important to recognize this impact and tailor the system accordingly; in order to best take advantage of the ionic complex effects, the order of operations of NCh addition and pH adjustment of the system must be considered and chosen deliberately depending upon whether such aggregation is desired in the system or not.

4.5 CONCLUSIONS

NCh and CNF are both high-value materials with demonstrated use in a wide variety of applications, but by taking advantage of their inherently complementary properties, we can create a synergistic system with increased potential and improved performance for some applications. The concentration-dependent and pH-dependent behaviors of these materials in aqueous suspension provide an opportunity to finely tune the microstructure and elasticity of the system over a full order of magnitude without adjusting the solids content, by manipulating both the concentration and pH conditions. By applying the same principles to other varieties of biobased nanomaterials (*e.g.,* TEMPO-CNF, CNC, nanochitin with different charge densities), an almost limitless array of tunability emerges. Exploiting this opportunity for complex formation can also reduce or mitigate the use of crosslinking agents or ionic liquid solvents in some instances and thereby reduce environmental impact.

4.6 REFERENCES

(1) Shen, X.; Shamshina, J. L.; Berton, P.; Gurau, G.; Rogers, R. D. Hydrogels Based on Cellulose and Chitin: Fabrication, Properties, and Applications. *Green Chem.* **2015**, *18* (1), 53–75. https://doi.org/10.1039/C5GC02396C.

(2) Ajdary, R.; Huan, S.; Zanjanizadeh Ezazi, N.; Xiang, W.; Grande, R.; Santos, H. A.; Rojas, O. J. Acetylated Nanocellulose for Single-Component Bioinks and Cell Proliferation on 3D-Printed Scaffolds. *Biomacromolecules* **2019**, *20* (7), 2770–2778. https://doi.org/10.1021/acs.biomac.9b00527.

(3) Gustafsson, S.; Lordat, P.; Hanrieder, T.; Asper, M.; Schaefer, O.; Mihranyan, A. Mille-Feuille Paper: A Novel Type of Filter Architecture for Advanced Virus Separation Applications. *Mater. Horiz.* **2016**, *3* (4), 320–327. https://doi.org/10.1039/C6MH00090H.

(4) Bai, L.; Huan, S.; Xiang, W.; Rojas, O. J. Pickering Emulsions by Combining Cellulose Nanofibrils and Nanocrystals: Phase Behavior and Depletion Stabilization. *Green Chem.* **2018**, *20* (7), 1571–1582. https://doi.org/10.1039/C8GC00134K.

(5) Bai, L.; Huan, S.; Xiang, W.; Liu, L.; Yang, Y.; Nugroho, R. W. N.; Fan, Y.; Rojas, O. J. Self-Assembled Networks of Short and Long Chitin Nanoparticles for Oil/Water Interfacial Superstabilization. *ACS Sustainable Chem. Eng.* **2019**, *7* (7), 6497–6511. https://doi.org/10.1021/acssuschemeng.8b04023.

(6) Jowkarderis, L.; van de Ven, T. Rheology of Semi-Dilute Suspensions of Carboxylated Cellulose Nanofibrils. *Carbohydr Polym* **2015**, *123*, 416–423. https://doi.org/10.1016/j.carbpol.2015.01.067.

(7) Nazari, B.; Kumar, V.; Bousfield, D. W.; Toivakka, M. Rheology of Cellulose Nanofibers Suspensions: Boundary Driven Flow. *Journal of Rheology (1978-present)* **2016**, *60* (6), 1151–1159. https://doi.org/10.1122/1.4960336.

(8) Lindström, T. Aspects on Nanofibrillated Cellulose (NFC) Processing, Rheology and NFC-Film Properties. *Current Opinion in Colloid & Interface Science* **2017**, *29*, 68–75. https://doi.org/10.1016/j.cocis.2017.02.005.

(9) Xu, H.-N.; Li, Y.-H. Decoupling Arrest Origins in Hydrogels of Cellulose Nanofibrils. *ACS Omega* **2018**, *3* (2), 1564–1571. https://doi.org/10.1021/acsomega.7b01905.

(10) Saarikoski, E.; Saarinen, T.; Salmela, J.; Seppälä, J. Flocculated Flow of Microfibrillated Cellulose Water Suspensions: An Imaging Approach for Characterisation of Rheological Behaviour. *Cellulose* **2012**, *19* (3), 647–659. https://doi.org/10.1007/s10570-012-9661-0.

(11) Gao, K.; Guo, Y.; Niu, Q.; Fang, H.; Zhang, L.; Zhang, Y.; Wang, L.; Zhou, L. Effects of Chitin Nanofibers on the Microstructure and Properties of Cellulose Nanofibers/Chitin Nanofibers Composite Aerogels. *Cellulose* **2018**, *25* (8), 4591–4602. https://doi.org/10.1007/s10570-018-1899-8.

(12) Li, J.; Revol, J.-F.; Marchessault, R. H. Rheological Properties of Aqueous Suspensions of Chitin Crystallites. *Journal of Colloid and Interface Science* **1996**, *183* (2), 365–373. https://doi.org/10.1006/jcis.1996.0558.

(13) Li, W.; Liu, W.; Wen, W.; Liu, H.; Liu, M.; Zhou, C.; Luo, B. The Liquid Crystalline Order, Rheology and Their Correlation in Chitin Whiskers Suspensions. *Carbohydrate Polymers* **2019**, *209*, 92–100. https://doi.org/10.1016/j.carbpol.2019.01.006.

(14) Yokoi, M.; Tanaka, R.; Saito, T.; Isogai, A. Dynamic Viscoelastic Functions of Liquid-Crystalline Chitin Nanofibril Dispersions. *Biomacromolecules* **2017**, *18* (8), 2564–2570. https://doi.org/10.1021/acs.biomac.7b00690.

(15) Decher, G. Fuzzy Nanoassemblies: Toward Layered Polymeric Multicomposites. *Science* **1997**, *277* (5330), 1232–1237. https://doi.org/10.1126/science.277.5330.1232.

(16) Grande, R.; Trovatti, E.; Carvalho, A. J. F.; Gandini, A. Continuous Microfiber Drawing by Interfacial Charge Complexation between Anionic Cellulose Nanofibers and Cationic Chitosan. *J. Mater. Chem. A* **2017**, *5* (25), 13098–13103. https://doi.org/10.1039/C7TA02467C.

(17) Otoni, C. G.; Queirós, M. V. A.; Sabadini, J. B.; Rojas, O. J.; Loh, W. Charge Matters: Electrostatic Complexation As a Green Approach to Assemble Advanced Functional Materials. *ACS Omega* **2020**, *5* (3), 1296–1304. https://doi.org/10.1021/acsomega.9b03690.

(18) Meka, V. S.; Sing, M. K. G.; Pichika, M. R.; Nali, S. R.; Kolapalli, V. R. M.; Kesharwani, P. A Comprehensive Review on Polyelectrolyte Complexes. *Drug Discovery Today* **2017**, *22* (11), 1697–1706. https://doi.org/10.1016/j.drudis.2017.06.008.

(19) Lankalapalli, S.; Kolapalli, V. R. M. Polyelectrolyte Complexes: A Review of Their Applicability in Drug Delivery Technology. *Indian J Pharm Sci* **2009**, *71* (5), 481–487. https://doi.org/10.4103/0250-474X.58165.

(20) Tirrell, M. Polyelectrolyte Complexes: Fluid or Solid? *ACS Cent. Sci.* **2018**, *4* (5), 532–533. https://doi.org/10.1021/acscentsci.8b00284.

(21) Marciel, A. B.; Srivastava, S.; Tirrell, M. V. Structure and Rheology of Polyelectrolyte Complex Coacervates. *Soft Matter* **2018**, *14* (13), 2454–2464. https://doi.org/10.1039/C7SM02041D.

(22) Feng, X.; Leduc, M.; Pelton, R. Polyelectrolyte Complex Characterization with Isothermal Titration Calorimetry and Colloid Titration. *Colloids and Surfaces A: Physicochemical and Engineering Aspects* **2008**, *317* (1), 535–542. https://doi.org/10.1016/j.colsurfa.2007.11.053.

(23) Fu, J.; Schlenoff, J. B. Driving Forces for Oppositely Charged Polyion Association in Aqueous Solutions: Enthalpic, Entropic, but Not Electrostatic. *J. Am. Chem. Soc.* **2016**, *138* (3), 980–990. https://doi.org/10.1021/jacs.5b11878.

(24) Lounis, F. M.; Chamieh, J.; Leclercq, L.; Gonzalez, P.; Geneste, A.; Prelot, B.; Cottet, H. Interactions between Oppositely Charged Polyelectrolytes by Isothermal Titration Calorimetry: Effect of Ionic Strength and Charge Density. *J. Phys. Chem. B* **2017**, *121* (12), 2684–2694. https://doi.org/10.1021/acs.jpcb.6b11907.

(25) Fu, J.; Fares, H. M.; Schlenoff, J. B. Ion-Pairing Strength in Polyelectrolyte Complexes. *Macromolecules* **2017**, *50* (3), 1066–1074. https://doi.org/10.1021/acs.macromol.6b02445.

(26) Huang, Y.; Lapitsky, Y. Monovalent Salt Enhances Colloidal Stability during the Formation of Chitosan/Tripolyphosphate Microgels. *Langmuir* **2011**, *27* (17), 10392–10399. https://doi.org/10.1021/la201194a.

(27) Huang, Y.; Lapitsky, Y. Determining the Colloidal Behavior of Ionically Cross-Linked Polyelectrolytes with Isothermal Titration Calorimetry. *J. Phys. Chem. B* **2013**, *117* (32), 9548–9557. https://doi.org/10.1021/jp405384b.

(28) Sun, X.; Peng, B.; Ji, Y.; Chen, J.; Li, D. Chitosan(Chitin)/Cellulose Composite Biosorbents Prepared Using Ionic Liquid for Heavy Metal Ions Adsorption. *AIChE Journal* **2009**, *55* (8), 2062–2069. https://doi.org/10.1002/aic.11797.

(29) Wu, J.; Liang, S.; Dai, H.; Zhang, X.; Yu, X.; Cai, Y.; Zhang, L.; Wen, N.; Jiang, B.; Xu, J. Structure and Properties of Cellulose/Chitin Blended Hydrogel Membranes Fabricated via a

Solution Pre-Gelation Technique. *Carbohydrate Polymers* **2010**, *79* (3), 677–684. https://doi.org/10.1016/j.carbpol.2009.09.022.

(30) Benselfelt, T.; Pettersson, T.; Wågberg, L. Influence of Surface Charge Density and Morphology on the Formation of Polyelectrolyte Multilayers on Smooth Charged Cellulose Surfaces. *Langmuir* **2017**, *33* (4), 968–979. https://doi.org/10.1021/acs.langmuir.6b04217.

(31) Shamshina, J. L.; Zavgorodnya, O.; Choudhary, H.; Frye, B.; Newbury, N.; Rogers, R. D. In Search of Stronger/Cheaper Chitin Nanofibers through Electrospinning of Chitin–Cellulose Composites Using an Ionic Liquid Platform. *ACS Sustainable Chem. Eng.* **2018**, *6* (11), 14713–14722. https://doi.org/10.1021/acssuschemeng.8b03269.

(32) Shamshina, J. L.; Zavgorodnya, O.; Berton, P.; Chhotaray, P. K.; Choudhary, H.; Rogers, R. D. Ionic Liquid Platform for Spinning Composite Chitin–Poly(Lactic Acid) Fibers. *ACS Sustainable Chem. Eng.* **2018**, *6* (8), 10241–10251. https://doi.org/10.1021/acssuschemeng.8b01554.

(33) Shen, X.; Shamshina, J. L.; Berton, P.; Bandomir, J.; Wang, H.; Gurau, G.; Rogers, R. D. Comparison of Hydrogels Prepared with Ionic-Liquid-Isolated vs Commercial Chitin and Cellulose. *ACS Sustainable Chem. Eng.* **2016**, *4* (2), 471–480. https://doi.org/10.1021/acssuschemeng.5b01400.

(34) Zhu, K.; Wang, Y.; Lu, A.; Fu, Q.; Hu, J.; Zhang, L. Cellulose/Chitosan Composite Multifilament Fibers with Two-Switch Shape Memory Performance. *ACS Sustainable Chem. Eng.* **2019**, *7* (7), 6981–6990. https://doi.org/10.1021/acssuschemeng.8b06691.

(35) Zhang, X.; Elsayed, I.; Navarathna, C.; Schueneman, G. T.; Hassan, E. B. Biohybrid Hydrogel and Aerogel from Self-Assembled Nanocellulose and Nanochitin as a High-Efficiency

Adsorbent for Water Purification. *ACS Appl. Mater. Interfaces* **2019**, *11* (50), 46714–46725. https://doi.org/10.1021/acsami.9b15139.

(36) Xu, J.; Zhou, Z.; Cai, J.; Tian, J. Conductive Biomass-Based Composite Wires with Cross-Linked Anionic Nanocellulose and Cationic Nanochitin as Scaffolds. *International Journal of Biological Macromolecules* **2019**. https://doi.org/10.1016/j.ijbiomac.2019.11.154.

(37) Benselfelt, T.; Engström, J.; Wågberg, L. Supramolecular Double Networks of Cellulose Nanofibrils and Algal Polysaccharides with Excellent Wet Mechanical Properties. *Green Chem.* **2018**, *20* (11), 2558–2570. https://doi.org/10.1039/C8GC00590G.

(38) Wågberg, L.; Decher, G.; Norgren, M.; Lindström, T.; Ankerfors, M.; Axnäs, K. The Build-Up of Polyelectrolyte Multilayers of Microfibrillated Cellulose and Cationic Polyelectrolytes. *Langmuir* **2008**, *24* (3), 784–795. https://doi.org/10.1021/la702481v.

(39) Toivonen, M. S.; Kurki-Suonio, S.; Wagermaier, W.; Hynninen, V.; Hietala, S.; Ikkala, O. Interfacial Polyelectrolyte Complex Spinning of Cellulose Nanofibrils for Advanced Bicomponent Fibers. *Biomacromolecules* **2017**, *18* (4), 1293–1301. https://doi.org/10.1021/acs.biomac.7b00059.

(40) Bonino, C. A.; Krebs, M. D.; Saquing, C. D.; Jeong, S. I.; Shearer, K. L.; Alsberg, E.; Khan, S. A. Electrospinning Alginate-Based Nanofibers: From Blends to Crosslinked Low Molecular Weight Alginate-Only Systems. *Carbohydrate Polymers* **2011**, *85* (1), 111–119. https://doi.org/10.1016/j.carbpol.2011.02.002.

(41) Pääkkö, M.; Ankerfors, M.; Kosonen, H.; Nykänen, A.; Ahola, S.; Österberg, M.; Ruokolainen, J.; Laine, J.; Larsson, P. T.; Ikkala, O.; Lindström, T. Enzymatic Hydrolysis Combined with Mechanical Shearing and High-Pressure Homogenization for Nanoscale

Cellulose Fibrils and Strong Gels. *Biomacromolecules* **2007**, *8* (6), 1934–1941. https://doi.org/10.1021/bm061215p.

(42) Johan Foster, E.; J. Moon, R.; P. Agarwal, U.; J. Bortner, M.; Bras, J.; Camarero-Espinosa, S.; J. Chan, K.; D. Clift, M. J.; D. Cranston, E.; J. Eichhorn, S.; M. Fox, D.; Y. Hamad, W.; Heux, L.; Jean, B.; Korey, M.; Nieh, W.; J. Ong, K.; S. Reid, M.; Renneckar, S.; Roberts, R.; Anne Shatkin, J.; Simonsen, J.; Stinson-Bagby, K.; Wanasekara, N.; Youngblood, J. Current Characterization Methods for Cellulose Nanomaterials. *Chemical Society Reviews* **2018**, *47* (8), 2609–2679. https://doi.org/10.1039/C6CS00895J.

(43) Fall, A. B.; Burman, A.; Wågberg, L. Cellulosic Nanofibrils from Eucalyptus, Acacia and Pine Fibers. *Nordic Pulp & Paper Research Journal* **2014**, *29* (1), 176–184. https://doi.org/10.3183/npprj-2014-29-01-p176-184.

(44) Liu, L.; Bai, L.; Tripathi, A.; Yu, J.; Wang, Z.; Borghei, M.; Fan, Y.; Rojas, O. J. High Axial Ratio Nanochitins for Ultrastrong and Shape-Recoverable Hydrogels and Cryogels via Ice Templating. *ACS Nano* **2019**, *13* (3), 2927–2935. https://doi.org/10.1021/acsnano.8b07235.

(45) Bai, L.; Kämäräinen, T.; Xiang, W.; Majoinen, J.; Seitsonen, J.; Grande, R.; Huan, S.; Liu, L.; Fan, Y.; Rojas, O. J. Chirality from Cryo-Electron Tomograms of Nanocrystals Obtained by Lateral Disassembly and Surface Etching of Never-Dried Chitin. *ACS Nano* **2020**, *14* (6), 6921–6930. https://doi.org/10.1021/acsnano.0c01327.

(46) Hansen, L. D.; Fellingham, G. W.; Russell, D. J. Simultaneous Determination of Equilibrium Constants and Enthalpy Changes by Titration Calorimetry: Methods, Instruments, and Uncertainties. *Analytical Biochemistry* **2011**, *409* (2), 220–229. https://doi.org/10.1016/j.ab.2010.11.002.

(47) Po, H. N.; Senozan, N. M. The Henderson-Hasselbalch Equation: Its History and Limitations. *J. Chem. Educ.* **2001**, *78* (11), 1499. https://doi.org/10.1021/ed078p1499.

(48) Zhu, Y.; Huan, S.; Bai, L.; Ketola, A.; Shi, X.; Zhang, X.; Ketoja, J. A.; Rojas, O. J. High Internal Phase Oil-in-Water Pickering Emulsions Stabilized by Chitin Nanofibrils: 3D Structuring and Solid Foam. *ACS Appl. Mater. Interfaces* **2020**, *12* (9), 11240–11251. https://doi.org/10.1021/acsami.9b23430.

(49) Spaic, M.; Small, D. P.; Cook, J. R.; Wan, W. Characterization of Anionic and Cationic Functionalized Bacterial Cellulose Nanofibres for Controlled Release Applications. *Cellulose* **2014**, *21* (3), 1529–1540. https://doi.org/10.1007/s10570-014-0174-x.

(50) Fukuzumi, H.; Saito, T.; Okita, Y.; Isogai, A. Thermal Stabilization of TEMPO-Oxidized Cellulose. *Polymer Degradation and Stability* **2010**, *95* (9), 1502–1508. https://doi.org/10.1016/j.polymdegradstab.2010.06.015.

(51) Zhu, L.; Kumar, V.; Banker, G. S. Examination of Aqueous Oxidized Cellulose Dispersions as a Potential Drug Carrier. I. Preparation and Characterization of Oxidized Cellulose-Phenylpropanolamine Complexes. *AAPS PharmSciTech* **2004**, *5* (4), 138–144. https://doi.org/10.1208/pt050469.

(52) Kötz, J.; Philipp, B.; Nehls, I.; Heinze, T.; Klemm, D. Zum Polyelektrolytverhalten einer C-6-substituierten Carboxycellulose im Vergleich zu Carboxymethylcellulose. *Acta Polymerica* **1990**, *41* (6), 333–338. https://doi.org/10.1002/actp.1990.010410605.

(53) Corder, R. D.; Dudick, S. C.; Bara, J. E.; Khan, S. A. Photorheology and Gelation during Polymerization of Coordinated Ionic Liquids. *ACS Appl. Polym. Mater.* **2020**, *2* (6), 2397–2405. https://doi.org/10.1021/acsapm.0c00343.

(54) Varanasi, S.; He, R.; Batchelor, W. Estimation of Cellulose Nanofibre Aspect Ratio from Measurements of Fibre Suspension Gel Point. *Cellulose* **2013**, *20* (4), 1885–1896. https://doi.org/10.1007/s10570-013-9972-9.

(55) Abitbol, T.; Kam, D.; Levi-Kalisman, Y.; Gray, D. G.; Shoseyov, O. Surface Charge Influence on the Phase Separation and Viscosity of Cellulose Nanocrystals. *Langmuir* **2018**. https://doi.org/10.1021/acs.langmuir.7b04127.

(56) Mertins, O.; Dimova, R. Insights on the Interactions of Chitosan with Phospholipid Vesicles. Part I: Effect of Polymer Deprotonation. *Langmuir* **2013**, *29* (47), 14545–14551. https://doi.org/10.1021/la403218c.

(57) Narkevicius, A.; Steiner, L. M.; Parker, R. M.; Ogawa, Y.; Frka-Petesic, B.; Vignolini, S. Controlling the Self-Assembly Behavior of Aqueous Chitin Nanocrystal Suspensions. *Biomacromolecules* **2019**. https://doi.org/10.1021/acs.biomac.9b00589.

(58) Grolier, J.-P. E.; del Río, J. M. On the Physical Meaning of the Isothermal Titration Calorimetry Measurements in Calorimeters with Full Cells. *Int J Mol Sci* **2009**, *10* (12), 5296–5325. https://doi.org/10.3390/ijms10125296.

CHAPTER 5

Summary and Outlook

5.1 Overview

In this work, three different aqueous suspension systems of biobased nanomaterials have been studied, and a characteristic behavior of each has been explored from the perspective of interactions between the suspended particles. In **Chapter 2**, micro/nanofibrillated cellulose (MNFC) interactions drive flocculation; in **Chapter 3**, cellulose nanocrystal (CNC) interactions generate a thermal signature that allows detection of c^*; in **Chapter 4**, ionic attractions of nanochitin (NCh) and cellulose nanofibrils (CNF) induce complex formation. These interactions shape the microstructure and shear response of the suspensions, the understanding of which is critical to guide the implementation of these materials and optimization for target applications. Although many questions remain unanswered, the efforts of the biobased nanomaterial research community have been promising thus far, and represent real progress towards long-term, practical implementation of sustainable materials. In this chapter, we provide a brief summary of each of the studies presented in this work and offer some perspectives on recommended next steps, which may directly follow from the work presented herein and add value and application to the insights already provided.

5.2 Shear-generated structures of flocculated MNFC suspensions (Chapter 2)

5.2.1 Summary: Shear-generated structures of flocculated MNFC suspensions

In Chapter 2, we examined the relationship between application of shear and evolution of microstructure in flocculated MNFC suspensions. We found that heterogeneous features are reproducibly generated by specific shear regimes. These are the result of aggregation between fibrils and floc development under shear, and they can be avoided or disrupted by deliberate application of higher shear levels if particular care is taken in the cessation of shear. Specifically, an immediate stop of shear application from a high shear rate is preferable over a gradual reduction of shear rate to prohibit formation of heterogeneous features. The observation of a two-step yield mechanism reinforced the significance of hierarchical nature of MNFC suspensions, in which each structural level yields independently. Quantitative agreement was found between the critical values detected *via* steady shear measurements, structure recovery measurements, and yield stress measurements. Taken together, these experiments indicate that the observed behaviors are not an artifact of measurement and are in fact inherent to the specific system. The results of this work have implications for several applications of MNFC suspensions, such as coatings and 3D printing, and can be used to help guide the selection of processing conditions and end-use applications.

5.2.2 Outlook: Shear-generated structures of flocculated MNFC suspensions

We chose to focus on a concentration of 1 wt%, for two reasons: (1) the phenomena of interest which motivated the work (such as viscosity kink) were particularly visible in this system, allowing clear demonstration of these effects as we explored the cause, and (2) this value is on the order of a concentration that would likely be used in a real system as a thickener or reinforcing additive. We consider this study to be a useful demonstration of the shear-induced floc formation and breakdown processes at hand, but the field would benefit substantially from further investigation to the analogous effects at a wider range of concentrations. This insight would inform selection of properties for additional applications and help create a more complete picture of the fundamental behavior to guide analysis and modeling efforts for this and related systems. Extended studies that explore the persistence or development of the recorded behaviors in combined systems with additives or other components (interacting or noninteracting) would likewise broaden the real-world impact of the discoveries presented in this work. A similarly useful effort would be a study on the drying effects of the heterogeneities; for example, how drying time is affected by the presence of heterogenous features and how the properties of the final product (dried coating, film, or aerogel) are impacted by these features, as determined by surface characterization and mechanical testing.

5.3. Calorimetric detection of chiral nematic ordering transition (Chapter 3)

5.3.1 Summary: Calorimetric detection of chiral nematic ordering transition

In Chapter 3 we proposed a new method by which the critical concentration (c^*) of a chiral nematic CNC suspension can be determined using calorimetry. We developed this method by measuring the heat of interaction during dilution of previously well-characterized CNC samples, focusing on two properties known to impact the c^* value: aspect ratio and surface charge. Our results indicate that the viscosity change associated with dilution of a sample is delicately influenced by the driving forces for chiral nematic phase separation, leading to a different heat signal for an isotropic suspension (below c^*) compared to one that will phase separate at equilibrium (above c^*). Once we established a critical heat value indicative of c^*, we tested it by predicting the c^* values of new samples provided by colleagues in the field. The agreement of our predicted values with the values expected or measured by other techniques indicates the potential for a new standard of characterization. This method reduces the required time to find c^* from days to hours, and the necessary sample volume from milliliters to microliters. The technique can also be utilized as a quality control tool for well-characterized samples.

5.3.2 Outlook: Calorimetric detection of chiral nematic ordering transition

It is evident from this work that viscosity and chiral nematic phase formation are linked in a complex manner. We have established a criterion for calorimetric measurement of c^* in CNC suspensions, but certain experiments indicate challenges in testing of samples with dramatically different rheological properties. To this point, a rigorous fundamental study of the relationship between viscosity and phase separation would be a major benefit to the field. This subject has been touched upon in previous works, but a comprehensive study including thixotropy, steady state viscosity, and shear-induced orientation is still missing and would elucidate some of the fundamental basis for the thermal responses observed in this work. Additionally, we found in the course of this work that a deliberately fractionated CNC suspension of higher aspect ratio appears to exhibit notably lower viscosity compared to equivalent suspensions that have not been subjected to fractionation. The explanation for such a distinction was not immediately within the scope of this work, but it does appear to be a relevant and interesting research question, especially for a thorough fundamental understanding of CNC suspensions, their rheological properties and their chiral nematic phase behavior.

5.4 Ionic complexes of nanocellulose and nanochitin (Chapter 4)

5.4.1 Summary: Ionic complexes of nanocellulose and nanochitin

In Chapter 4 we explored ionic complex formation of anionic nanocellulose with cationic nanochitin in aqueous suspension. Specifically, we studied the interactions as quantified by isothermal titration calorimetry, which revealed a complex interplay of interactions, including protonation and deprotonation equilibrium effects due to the differing pH conditions of the materials, in addition to the expected electrostatic attraction and ionic bond formation. We decoupled these interactions by adjusting the initial pH conditions of the suspensions, revealing a broad range of microstructure properties accessible for an aqueous suspension at a single solids content. A precise degree of control over viscosity and elasticity of this system was demonstrated by adjustment of the nanochitin to nanocellulose ratio and pH conditions of the mixture. This tunability can provide an advantage by facilitating the use of these particles outside of their typical operable windows (*i.e.*, pH conditions that allow colloidal stability, solids contents suitable for target application, compatibility with additional components). These interactions are synergistic in that they have the potential to increase the elasticity of the system and provide irreversible structural connections similar to a crosslinked system, but without the use of covalent crosslinkers.

5.4.2 Outlook: Ionic complexes of nanocellulose and nanochitin

The advantages of combining the properties of nanocellulose and nanochitin have begun to attract deserved attention, and this study is an early step towards realizing the potential of such hybrid systems. Several additional aspects can broaden and deepen the understanding provided by this study and its value to real world applications. One example is higher solids contents, which will undoubtedly be associated with a more complex set of rheological behaviors. As the concentration of either particle is increased, thorough mixing of the suspensions will be impacted which is likely to affect the homogeneity of the suspension and its response to shear. Additionally, implementing other varieties of nanocellulose and nanochitin, such as CNCs and higher aspect ratio ChNFs with varying levels of surface charge can expand the potential pH conditions, network structures and aggregation behaviors expected in the composite system. One can imagine quite readily the wide variety of properties accessible by substituting a fibril/fibril system or a crystal/crystal system for the system studied here, which is most accurately identified as fibril/crystal due to the relatively low aspect ratios (~15) of NCh used. This extensive library of available components deserves thorough characterization to guide material selection for relevant applications.

APPENDICES

Appendix A

Supporting Information for Chapter 2

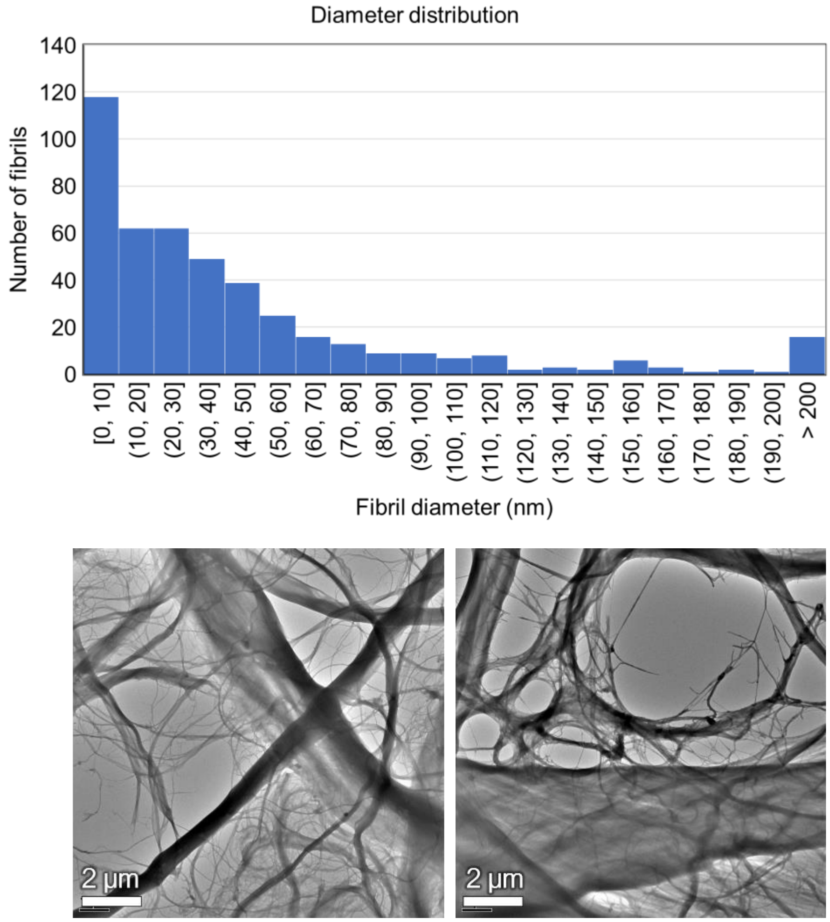

Figure A.1. Fibrillar diameters (top) as measured from transmission electron microscopy images (bottom).

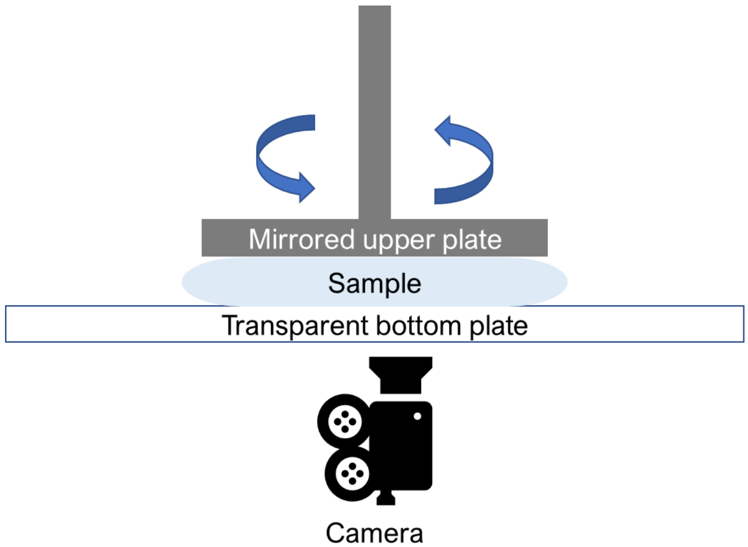

Figure A.2. Schematic diagram of the rheo-optical imaging setup.

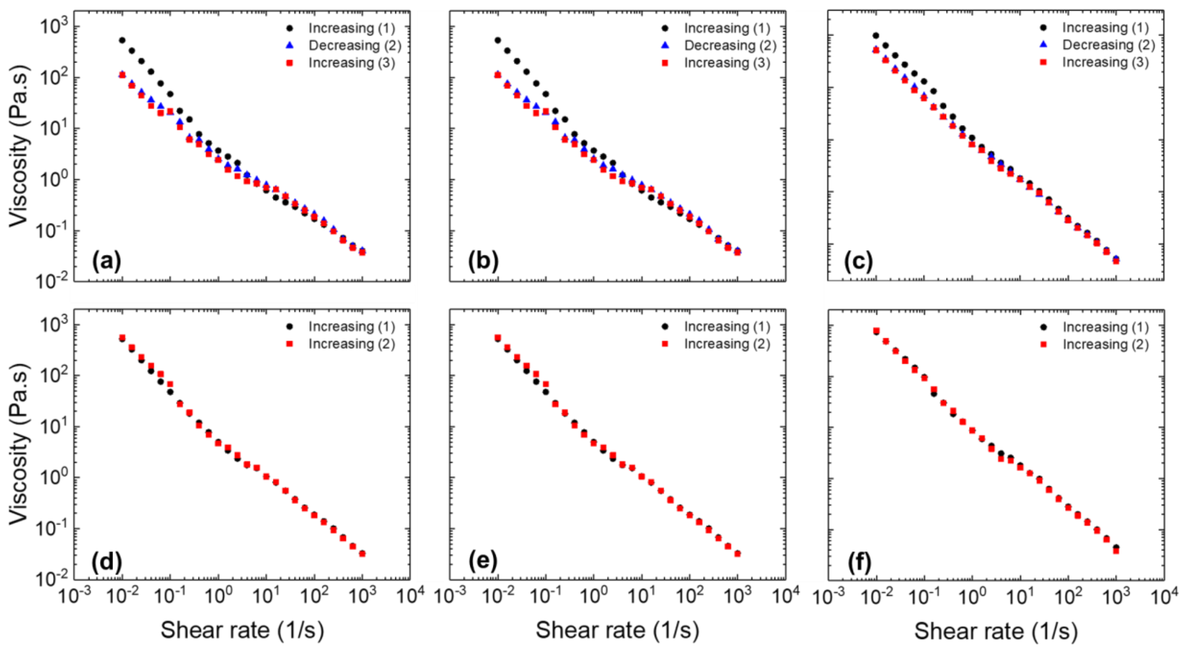

Figure A.3. Slow-quench (a-c) *vs*. fast-quench (d-f) test sequences for MNFC suspensions differing in composition (in wt%): (a,d) 2, (b,e) 2.5, (c,f) 3.1% (c,f). The symbols are described in the legends.

Figure A.4. Rheometer image from intermediate oscillatory stress (10 Pa)

Fibril size analysis

The difficulty of accurately measuring lengths of MNFC has been documented,[1,2] but an approximation can be reached by using the relationship between intrinsic viscosity and aspect ratio. The manufacturer[3] lists the fiber dimensions for MNFC as follows: "Fiber dimensions: nominal fiber width of 50 nm, lengths of up to several hundred microns." By applying the Simha equation[4] using calculated intrinsic viscosity and the density of fibrils as provided by the manufacturer (1.5 g/cm^3), we predict an aspect ratio of 189.

Iwamoto et al.[5] studied the use of the Simha equation to estimate aspect ratios of TEMPO-CNFs and found that it resulted in an underprediction, with actual aspect ratios roughly twice the estimated value. We therefore take the prediction of 189 as an approximation of the minimum aspect ratio and consider that a more reasonable estimate is obtained by doubling this value (a = 378). With this updated estimate, and TEM measured diameters in the range of 5-200 nm, we arrive at lengths of individual fibrils in the range of 2-75 μm. When considering the extensive entanglement and aggregation at play in the system, the manufacturer's estimate of "several hundreds of microns" remains valid in practice.

Generally, particle sizes > 1 μM are not expected to show remarkable Brownian motion,[6] and in the case of MNFC the largest fibril dimension is almost always in excess of that limit, sometimes by an order of magnitude or more. While some systems of cellulose nanomaterials may exhibit Brownian effects in the limits of very dilute suspensions ($\Phi \ll a^{-2}$),[7,8] the samples discussed here are not considered dilute and are expected to have substantial contributions of hydrodynamic forces (Pe > 1).[9]

We refer to an analysis presented by Tao et al. for long thin rods,[10] and we calculate rotational and translational diffusion constants to be $D_r = 7.67*10^{-4}\ s^{-1}$ and $D_t = 1.17*10^{-13} m^2 s^{-1}$. This calculation assumes a fibril length of 38 μm and diameter of 10 nm.

Using a fibril length of 38 μm and diameter of 10 nm, cellulose density 1.5 g/cm^3, a 1.0 wt. % suspension is calculated to have a number density of 1.76×10^{12} mL^{-1}.

We note that these calculations are subject to certain limitations, such as approximation of MNFC particles as long thin rigid rods, and these values should be taken only as relative measures for comparison and not necessarily as definitive quantifications.

REFERENCES for APPENDIX A

(1) Shinoda, R.; Saito, T.; Okita, Y.; Isogai, A. Relationship between Length and Degree of Polymerization of TEMPO-Oxidized Cellulose Nanofibrils. *Biomacromolecules* **2012**, *13* (3), 842–849. https://doi.org/10.1021/bm2017542.

(2) Li, Q.; Renneckar, S. Molecularly Thin Nanoparticles from Cellulose: Isolation of Sub-Microfibrillar Structures. *Cellulose* **2009**, *16* (6), 1025–1032. https://doi.org/10.1007/s10570-009-9329-6.

(3) Nanocellulose Data Sheets - The Process Development Center - University of Maine. *The Process Development Center*.

(4) Simha, R. The Influence of Brownian Movement on the Viscosity of Solutions. *J. Phys. Chem.* **1940**, *44* (1), 25–34. https://doi.org/10.1021/j150397a004.

(5) Iwamoto, S.; Lee, S.-H.; Endo, T. Relationship between Aspect Ratio and Suspension Viscosity of Wood Cellulose Nanofibers. *Polym J* **2014**, *46* (1), 73–76. https://doi.org/10.1038/pj.2013.64.

(6) Chapter 6 - Physics of Electrorheological Fluids. In *Studies in Interface Science*; Hao, T., Ed.; Electrorheological Fluids; Elsevier, 2005; Vol. 22, pp 235–340. https://doi.org/10.1016/S1383-7303(05)80021-3.

(7) Johan Foster, E.; J. Moon, R.; P. Agarwal, U.; J. Bortner, M.; Bras, J.; Camarero-Espinosa, S.; J. Chan, K.; D. Clift, M. J.; D. Cranston, E.; J. Eichhorn, S.; M. Fox, D.; Y. Hamad, W.; Heux, L.; Jean, B.; Korey, M.; Nieh, W.; J. Ong, K.; S. Reid, M.; Renneckar, S.; Roberts, R.; Anne Shatkin, J.; Simonsen, J.; Stinson-Bagby, K.; Wanasekara, N.; Youngblood, J. Current Characterization Methods for Cellulose Nanomaterials. *Chemical Society Reviews* **2018**, *47* (8), 2609–2679. https://doi.org/10.1039/C6CS00895J.

(8) Bröckel, U.; Meier, W.; Wagner, G. *Product Design and Engineering: Formulation of Gels and Pastes*; John Wiley & Sons, 2013.

(9) Hubbe, M. A.; Tayeb, P.; Joyce, M.; Tyagi, P.; Kehoe, M.; Dimic-Misic, K.; Pal, L. Rheology of Nanocellulose-Rich Aqueous Suspensions: A Review. *BioResources* **2017**, *12* (4), 9556–9661.

(10) Tao, Y.-G.; den Otter, W. K.; Padding, J. T.; Dhont, J. K. G.; Briels, W. J. Brownian Dynamics Simulations of the Self- and Collective Rotational Diffusion Coefficients of Rigid Long Thin Rods. *J. Chem. Phys.* **2005**, *122* (24), 244903. https://doi.org/10.1063/1.1940031.

Appendix B

Supporting Information for Chapter 3

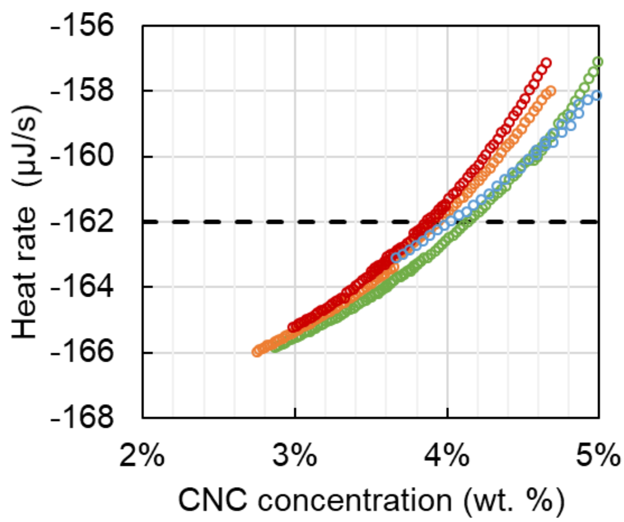

Figure B.1. Reproducibility of c^* measurements from ITC. Four different runs of suspensions containing as-received FPL-CNC confirm close agreement in terms of the heat rate signal. The average value at which they cross the threshold heat rate (at -162 μJ/s) is 3.95 ± 0.08 wt%.

Figure B.2. Optical image of a suspension containing a vial of 4 wt% FPL-CNC between crossed polarizers. The lower anisotropic region appears bright and yields φ = 0.06.

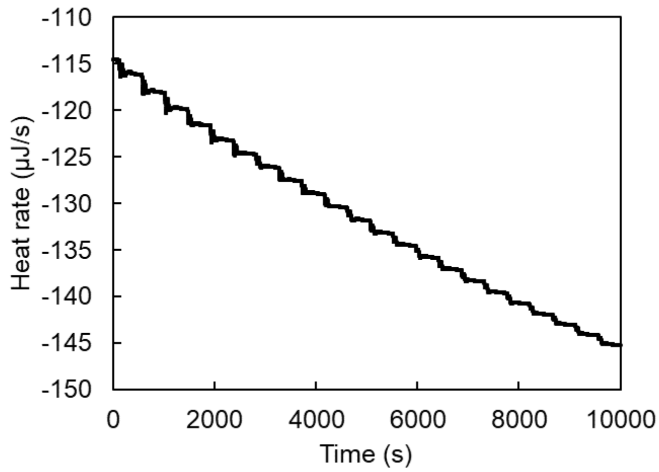

Figure B.3. Raw heat signal measured by injecting water into an aqueous suspensions with 8 wt% FPL-CNC. Each "step" indicates an injection of 2 μL of water into the 170 μL cell, resulting in a slightly reduced CNC concentration and a corresponding shift to a new baseline at a more exothermic heat value. The heater provides additional heat to maintain isothermal conditions to account for the reduction in viscous heating effects in the cell.

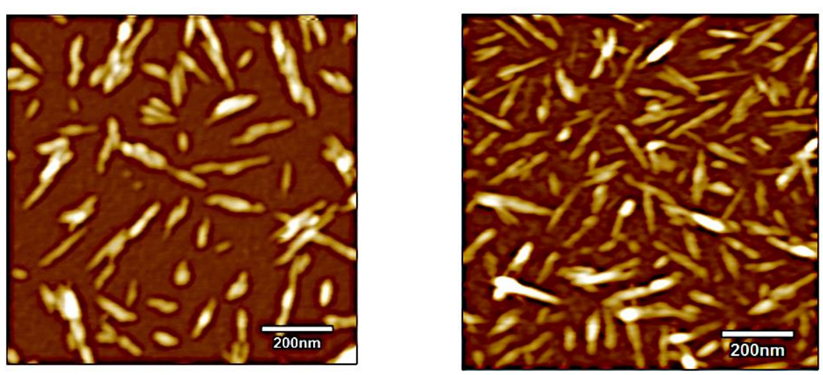

Figure B.4. AFM images of as-received FPL-CNC (left) and FPL-CNC after a reduction in CNC aspect ratio due to fractionation (right). Measurements of several images yield the nanocrystal dimensions and, as a consequence, their aspect ratios (see **Table 3.1**).

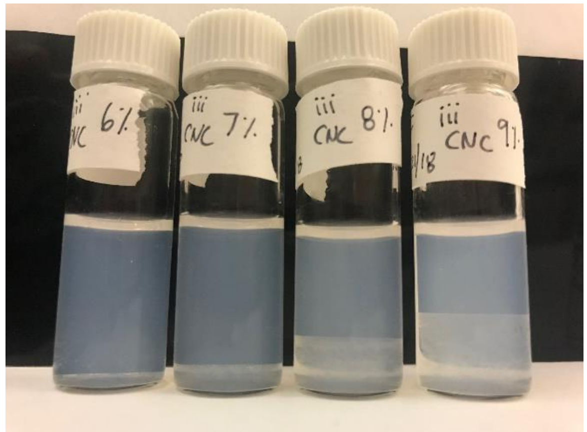

Figure B.5. Fractionated S-CNC suspensions prepared at different concentrations (see labels) and revealing the first evidence of mesophase-induced phase separation at 6 wt% (φ = 0.08).

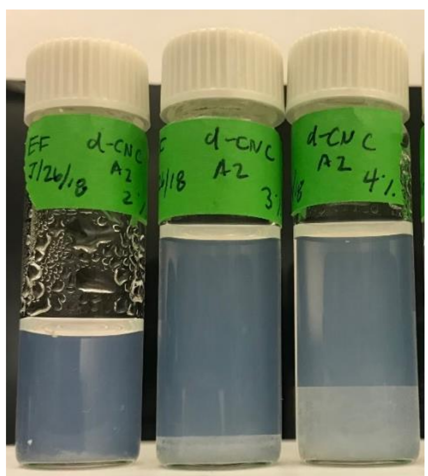

Figure B.6. Desulfated D-CNC suspensions prepared at different concentrations (see labels) and revealing the first evidence of mesophase-induced phase separation at 3 wt% (φ = 0.12).

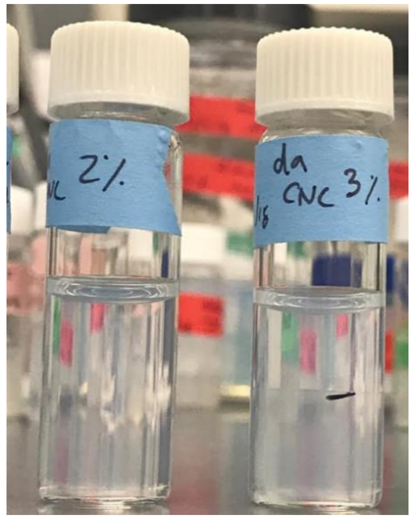

Figure B.7. Desulfated and fractionated LD-CNC suspensions prepared at two concentrations (see labels) and revealing the first evidence of mesophase-induced phase separation at 3 wt% (φ = 0.58). No phase separation is observed at 2 wt%.

Figure B.8. Aqueous UBC-CNC suspensions prepared at several concentrations with 1 mM NaCl and revealing the first evidence of mesophase-induced phase separation at 7 wt%.

Sample Calculation.

To establish the efficiency of this approach, the following sample calculation estimates that the experimental time to identify c^* can be reduced by 60x, while the sample volume can be reduced by 40x. In the ITC instrument used in this study, a typical titration experiment can be completed in 100 min (20 injections of 2.5 μL with 300 s equilibration after each injection), with 300 μL of sample at a single concentration (provided it is initially above c^*). Note that, although the calorimeter is loaded with 300 μL of sample, the active cell volume in which dilution and heat balance proceeds is 170 μL. In addition, after each injection, an equivalent volume is expelled from the well-mixed cell through a one-way outlet in similar mass-balance fashion as a continuous stirred tank reactor. Hence, the concentration after the *n*th injection (c_n) can be calculated as $c_n = c_{n-1}$ (170 - v_i)/170, where v_i is the volume of the injection in μL (2.5 in this example). If we take the initial suspension concentration as c_0 = 8 wt%, the cell concentration will be reduced to 5.95 wt% after 20 injections of 2.5 μL, and the experiment will generate data points at concentration intervals of approximately 0.1 wt% (see **Table B1**). In the event that the c^* threshold has not been crossed, the experiment can be extended by simply reloading the syringe with DI water and repeating the same procedure. With a new initial concentration of 5.95 wt%, the second stage of injections will reduce concentrations down to 4.42 wt%, and so on. Since removal and reloading the titration syringe can be accompanied by backmixing via diffusion from the more concentrated cell overflow volume reservoir into the active cell volume is possible, c_0 should be selected to so that c^* can be reached in a single experiment. For comparison purposes, however, we will be conservative in estimating experimental time and assume that this condition was not met, in which case 3 reloading steps are necessary. We allow 20 min prior to each trial to load the syringe (5 min) and equilibrate the initial heat baseline (15 min) for a total experimental time of 330 min and a "hands-on" or active time of 15 min. This will provide data points at 60 discrete concentrations (3 rounds x 20 injections per round). To achieve the same number of suspension concentration data points by observation in capillary tubes, one might prepare 200 μL per concentration and permit quiescent equilibration for up to 2 weeks (*cf.* **Figure B.8**). This would require a sample volume 40x greater than that used by ITC and an experimental time 60x greater. Direct observation would yield additional information regarding φ. Furthermore, one would not likely prepare 60 different concentrations, since many would be visually indistinguishable or might be so far above or below c^* that they would be unnecessary. We make this comparison to illustrate the potential for ITC to provide a quick initial measurement, which can then be corroborated and expanded using complementary methods to provide additional details about the sample (*e.g.*, φ and pitch).

Table B.1. Concentration progression of an ITC experiment

Injection	CNC concentration (wt%)	Baseline heat rate (μJ/s)
1	7.88	-115.76
2	7.77	-118.29
3	7.65	-120.15
4	7.54	-121.75
5	7.43	-123.21
6	7.32	-124.53
7	7.21	-126.40
8	7.11	-127.60
9	7.00	-129.33
10	6.90	-130.26
11	6.80	-132.25
12	6.70	-133.72
13	6.60	-134.65
14	6.50	-135.98
15	6.41	-137.17
16	6.31	-138.37
17	6.22	-140.10
18	6.13	-140.76
19	6.04	-142.09
20	5.95	-143.56

Appendix C

Supporting Information for Chapter 4

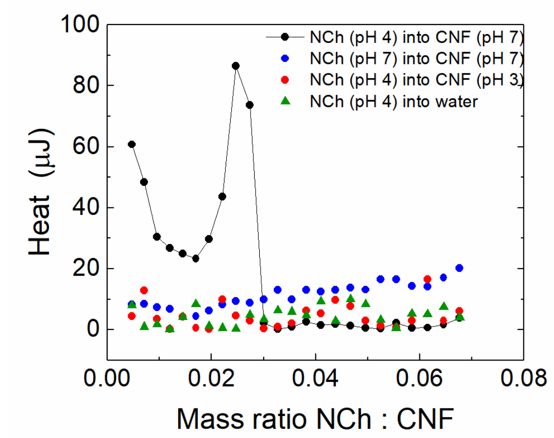

Figure C.1. Thermogram for NCh titrated into CNF compared with blank runs of NCh injected into water, NCh injected into acidic CNF, and neutralized NCh injected into CNF.

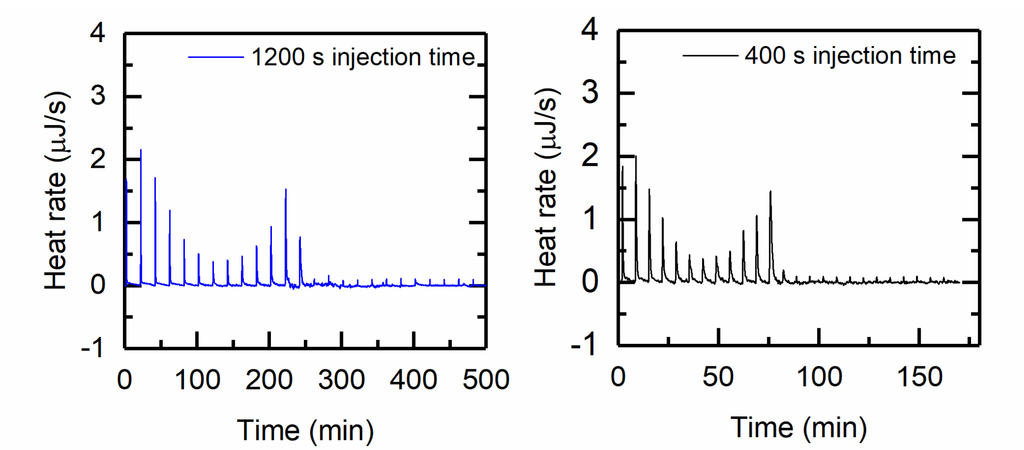

Figure C.2. Changing the equilibration time per injection has no apparent impact on the results.

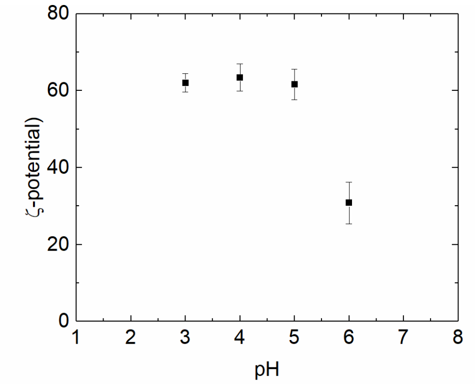

Figure C.3. Zeta potential of NCh as a function of pH. At lower pH, % protonation and therefore % ionization of the NH_2 groups to NH_3^+ is higher, resulting in a more positive zeta potential and a more stable suspension.

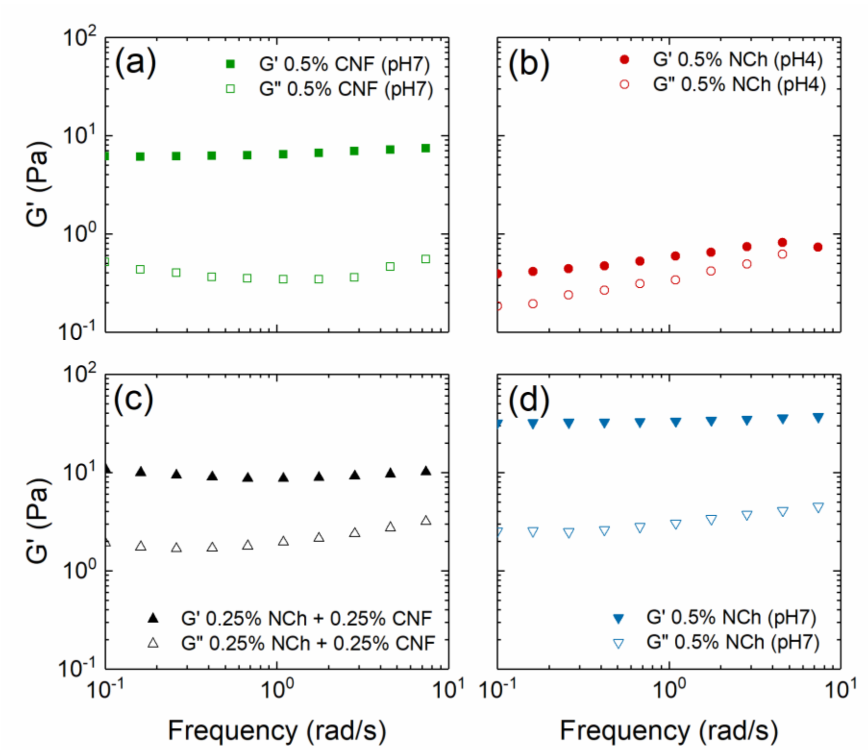

Figure C.4. Frequency sweeps showing G' (filled symbols) and G" (open symbols) for (a) CNF at pH 7 (b) NCh at pH 5 (c) equal mixture CNF + NCh at pH ~5.5 (d) NCh adjusted to pH 7

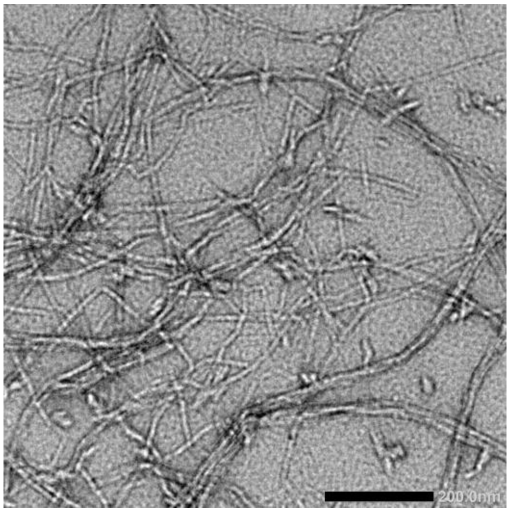

Figure C.5. Morphology of CNF (TEM). Scale bar is 200 nm.

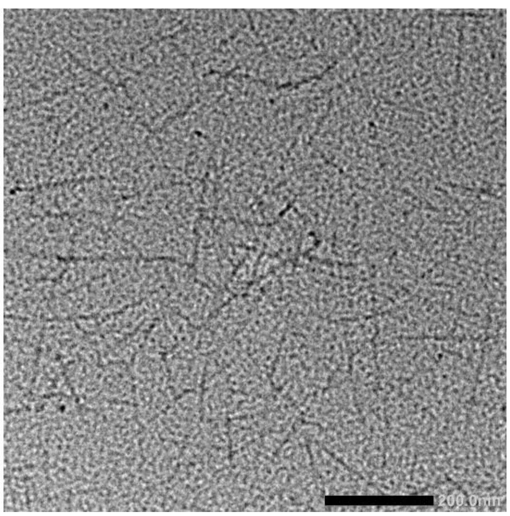

Figure C.6. Morphology of NCh (TEM). Scale bar is 200 nm.

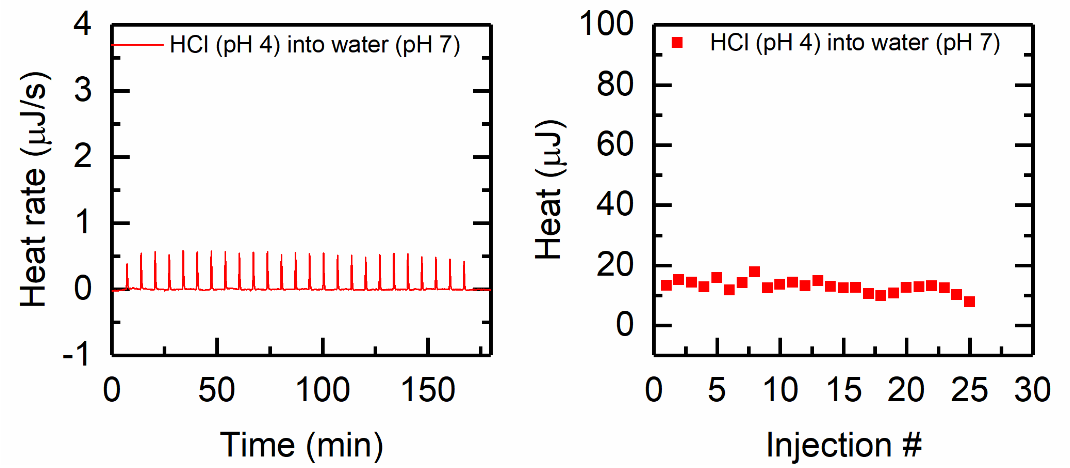

Figure C.7. Dilute HCl (pH 4) into water (pH 7). Changing pH alone (in absence of protonation/deprotonation) exhibits a constant and small heat signal.

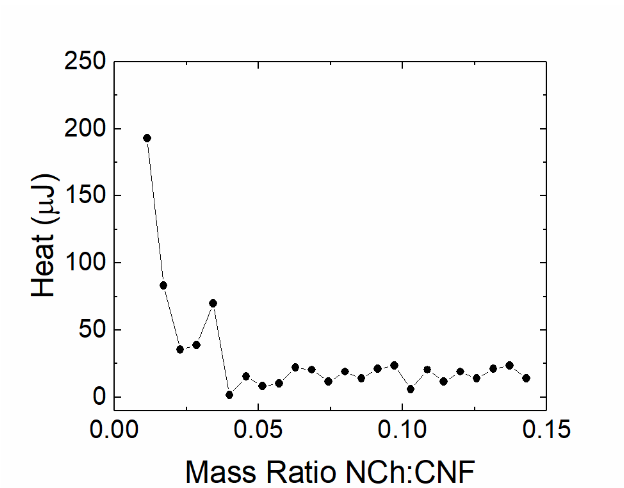

Figure C.8. 0.1 wt% NCh into 0.1 wt% CNF reaches the charge saturation point (0.03 g NCh per g CNF) in fewer injections than is required for 0.01 wt% NCh INTO 0.05%, but the value is the same.

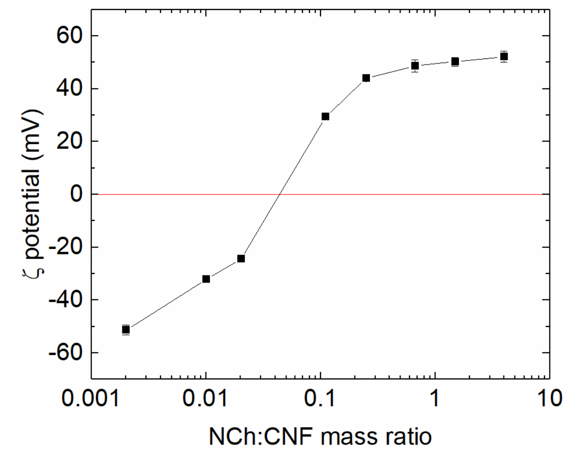

Figure C.9. Zeta potential of 0.5 wt% total solids in water at different NCh ratios. The ζ-potential crosses from negative to positive between 0.02 and 0.11 g NCh per g CNF

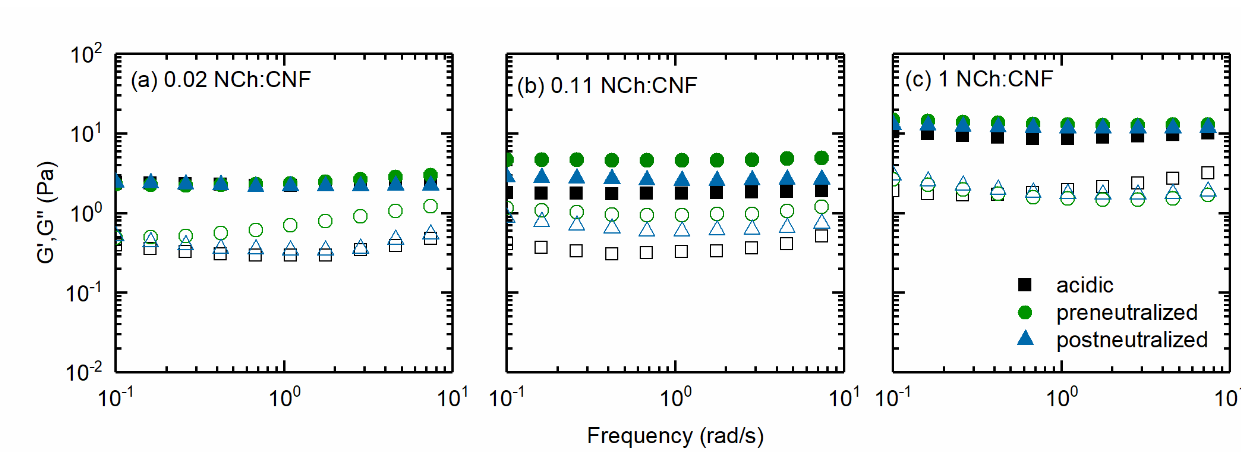

Figure C.10. Frequency sweeps including G' (filled symbols) and G" (open symbols) for mixed systems of CNF + NCh at 0.5 wt% solids for different mass ratios, (a) 0.02 g NCh per g CNF, (b) 0.11 g NCh per g CNF, (c) 1 g NCh per CNF. Symbols represent pH conditions, black squares indicate no pH adjustment, green circles indicate NCh was neutralized prior to mixing, blue triangles indicate the mixture was neutralized after addition of NCh to CNF.

Sample calculation: Mass of deprotonated nanochitin per injection

Mass of NCh deprotonated per injection is calculated by applying the Henderson-Hasselbach equation for the pH of the given injection, multiplying % ionization by mass of NCh in the cell for the injection, and subtracting the amount for the previous injection.

For the n^{th} injection, the mass of nanochitin subjected to deprotonation can be calculated as follows:

% deprotonation at pH *n*:

$pH_n = pKa + \log_{10}[A-]/[HA]$

$pKa = 6.3$

$\log_{10}[A^-]/[HA] = pH_n - pKa = x$

$[A^-]/[HA] = 10^x = \%$ deprotonation

Nanochitin mass in cell after injection *n* (a_n):

a_n = (syringe concentration) * (volume of injection) * (n)

Deprotonated nanochitin mass in cell (d_n)

$d_n = a_n$*(% deprotonation)

Deprotonated per injection *n* (*p*):

$p = d_n - d_{n-1}$